Master's thesis

NTNU
Norwegian University of Science and Technology
Faculty of Natural Sciences
Department of Physics

Sindre Synnes Lindseth

GAMMA-RAYS FROM SPIDER BINARIES

A search for gamma-ray emission around the nearby compact binary millisecond pulsar PSR J1720-0533

Master's thesis in Physics
Supervisor: Manuel Linares
May 2023

NTNU
Norwegian University of
Science and Technology

Sindre Synnes Lindseth

GAMMA-RAYS FROM SPIDER BINARIES

A search for gamma-ray emission around the nearby compact binary millisecond pulsar PSR J1720-0533

Master's thesis in Physics
Supervisor: Manuel Linares
May 2023

Norwegian University of Science and Technology
Faculty of Natural Sciences
Department of Physics

NTNU
Norwegian University of
Science and Technology

Table of Contents

List of Figures

List of Tables

Acknowledgements

I would like to express my deepest gratitude to my exceptional supervisor, Manuel Linares, for his support, guidance, and encouragement throughout my Master of Science in Physics. His insight, feedback, and sincere interest in my work have been crucial for me in my studies over the last couple of years, especially for this thesis.

I am also grateful to the LOVE-NEST group for interesting talks and discussions on compact binary millisecond pulsar physics. I appreciate their valuable feedback and the opportunity to share my work with them.

Furthermore, I would like to acknowledge the Faculty of Natural Sciences, and the Department of Physics at the Norwegian University of Science and Technology for providing the necessary equipment and facilities for my research. I am also grateful to the Astroparticle Physics group for organizing inspiring seminars and guest lecturers that have motivated me for academic growth.

Finally, I would like to thank my family, friends, and fellow students. Their support and positivity have been essential for my academic journey so far, and I am grateful for their continued encouragement in my future endeavors.

Abstract

The Fermi Large Area Telescope (LAT) has led to a drastic increase in the population of compact binary millisecond pulsars in the Galactic field (also known as 'spiders'). The majority of the known spider population shows γ-ray emission, thus making the subset of this group of pulsars that remain undetected in γ-rays an interesting exception. γ-ray quiet pulsars provide valuable constraints for modeling the high-energy emission originating from particle acceleration in the relativistic magnetospheres surrounding pulsars. In this thesis, we study in detail the γ-ray emission from the region surrounding PSR J1720-0533, a black widow spider discovered in 2021. With an estimated distance of only 0.2 kpc and a spin-down power of $\dot{E} = 8.5 \times 10^{33}\,\mathrm{erg\,s^{-1}}$, PSR J1720-0533 is the nearest known black widow, and a promising candidate for γ-ray detection due to its large $\dot{E}/d^2$-value. However, from a detailed analysis of the full 14-year data set collected by the Fermi-LAT between 2008 and 2022, we find no significant detection of γ-ray emission around the radio-timing position of PSR J1720-0533. We report a 95% upper limit on the γ-ray luminosity of $L_\gamma < 5.8 \times 10^{30}\,\mathrm{erg\,s^{-1}}$ (in the $0.1 - 100\,\mathrm{GeV}$ energy range), which is the deepest upper limit on the γ-ray luminosity of any pulsar to date. We discuss possible physical explanations behind the non-detection of γ-rays from this system, and how these results can improve our understanding of the γ-ray emission mechanisms from the relativistic magnetospheres of millisecond pulsars.

Chapter 1

Neutron Stars

Neutron stars are among the most interesting and extreme objects observable in the universe. Their large gravitational effect on the surrounding space-time together with their strong magnetic fields and short rotational periods give rise to various extreme physics phenomena. By studying neutron stars, astrophysicists can test and model theories of gravity, nuclear physics, particle physics, electrodynamics, and plasma physics, in conditions non-achievable on Earth.

1.1 Neutron star formation

These fascinating stars are born in the violent core collapse deaths of main sequence stars with masses larger than about $10M_\odot$ [1], where $M_\odot$ is the mass of the Sun. Stars with this mass or above exhaust all the hydrogen atoms in their core in the nucleosynthesis process where the atoms fuse into heavier elements. Once this chain of nuclear fusion reaches iron production, the process stops as the fusion of iron nuclei does not produce any energy. The iron core grows until it reaches the theoretical maximum limit called the Chandrasekhar mass of about $1.4\,\mathrm{M}_\odot$ [2]. Once this limit is reached, the outward pressure from radiation can no longer balance inward pressure from the immense gravitational force, resulting in a core-collapse supernova explosion. In this supernova, the outward pressure from the core collapse strips away the outer layers of the star, creating a supernova remnant (SNR). The extreme density in the iron core triggers electron capture as the electron degeneracy pressure no longer can hold the star. In this electron capture process, the electrons combine with protons in the iron nuclei to produce neutrons via inverse β-decay [3]. If the total mass of the core is not too great, the neutron degeneracy pressure balances the gravitational forces, avoiding the collapse into a black hole. The result is a star of almost pure neutrons - a neutron star.

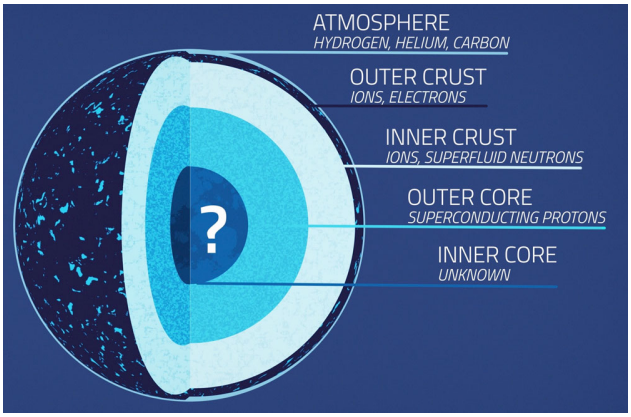

Figure 1.1: Model of the different shells in the neutron star's interior. Credit: NASA's Goddard Space Flight Center Conceptual Image Lab.

Neutron stars have a canonical mass of $M_{\mathrm{NS}} \simeq 1.4\,\mathrm{M}_\odot$, with a radius of only 12 km. Consequently, they have extreme mass densities, surpassing that of an atomic nucleus. These stars also have very short rotational periods, ranging from a few seconds to around 1 millisecond, and possess magnetic fields billions of times stronger than what can be produced on Earth (see Section 1.3). Despite almost a century of research, there are still many unanswered questions regarding these compact objects, such as which states of matter are to be found in the core regions and what

is the origin of the high-energy electromagnetic radiation.

1.2 Neutron star interiors

The neutron star's *equation of state* relates the star's density with pressure and temperature and is a hot topic for neutron star astronomers. It is essential for modeling the interior regions of the neutron star, which are shown in Figure 1.1. While astrophysicists have a good idea of the states of matter found in the outer regions of the neutron star, we do not have a good understanding of the core regions [4]. The outermost layer consists of a thin atmosphere, just some centimeters thick, composed of ionized hydrogen and helium atoms. Beneath the atmosphere lies a thin outer crust made out of free electrons and neutron-rich atomic nuclei in lattice structures. Deeper into the star, the neutron degeneracy pressure begins to play a role [5], and as pressure increases, neutrons start to decay from their parent nuclei. This region defines the separation of the inner and outer crust and is called the *neutron drip* line. Beneath this line, the free neutrons that decayed in the neutron drip exist in a super-fluid state creating vortices in the inner crust, known as *nuclear pasta* [6]. Beyond the inner crust lies the poorly understood regions of the stellar core. The core is generally divided into the outer and inner regions, where it is believed to exist a superconducting superfluid of neutrons and possibly free quarks or other exotic particles like hyperons [4], which are baryons containing one or more strange quarks.

1.3 Characteristic properties of neutron stars

Neutron stars exhibit other extreme properties besides their high mass densities in their interior regions. If we assume conservation of angular momentum during the core collapse, the initial angular momentum of the proto-neutron star equals the angular momentum of the newly born neutron star. With angular momentum $L = I\Omega \propto R^2/P$, this leads to the following relation between P_{NS} and P_0, which are the rotational periods of the neutron star and the proto-neutron star, respectively:

$$\frac{P_{\mathrm{NS}}}{P_0} = \left(\frac{R_{\mathrm{NS}}}{R_0}\right)^2. \tag{1.1}$$

Here, R_{NS} is the radius of the neutron star, and R_0 is the radius of the proto-neutron star. The small radii of neutron stars compared to those of the proto-neutron stars, result in very short rotational periods for these compact objects. Although this is an estimate, it explains the short observed rotational periods of young neutron stars on the order of $P \sim 100\,\mathrm{ms}$, as seen in Figure 1.2. A similar effect occurs for the magnetic field of the neutron star. The magnetic flux through the surface of the proto-neutron star is conserved during the collapse. Since the magnetic field flux is proportional to R^{-2} through the surface of a sphere with radius R, we derive the following inverse relation for the magnetic field strength compared to the rotational period:

$$\frac{B_{\mathrm{NS}}}{B_0} = \left(\frac{R_0}{R_{\mathrm{NS}}}\right)^2. \tag{1.2}$$

Here, B_0 and B_{NS} are the magnetic field strengths of the proto-neutron star and the neutron star, respectively. This relation explains the enormous magnetic field strengths of neutron stars. To get an idea of the order of magnitude of these fields we use the Sun's surface magnetic field strength $B_\odot \sim 1\,\mathrm{G}$, and radius $R_\odot \sim 10^6\,\mathrm{km}$, yielding $B_{\mathrm{NS}} \sim 10^{10}\,\mathrm{G}$. The magnetosphere of a neutron star is essential for multi-wavelength emission, as it accelerates elementary particles to relativistic speeds releasing broad-band electromagnetic radiation that we can observe with our telescopes.

The rotation of the neutron star, often approximated by that of a rotating magnetic dipole, produces electromagnetic radiation. This electromagnetic energy derives from the rotational kinetic energy of the neutron star and results in a fractional change in its rotational period over time. This change is quantified by the period derivative, denoted as $\dot{P} \equiv \mathrm{d}P/\mathrm{d}t$. A wide variety of P and $\dot{P}$ values have been observed for neutron stars, with P on the scales of $\sim 10^{-3} - 10^{1}\,\mathrm{s}$, and $\dot{P}$ on the scales of $\sim 10^{-9} - 10^{-21}$. A value of $\dot{P}/P = 10^{-15}\,\mathrm{s}^{-1}$ means the star loses 1 part in a quadrillion of its rotational period every second, which is equivalent to a loss of 0.1% in the rotational period in around 300 000 years. Such a steady rotational period makes it possible to measure neutron

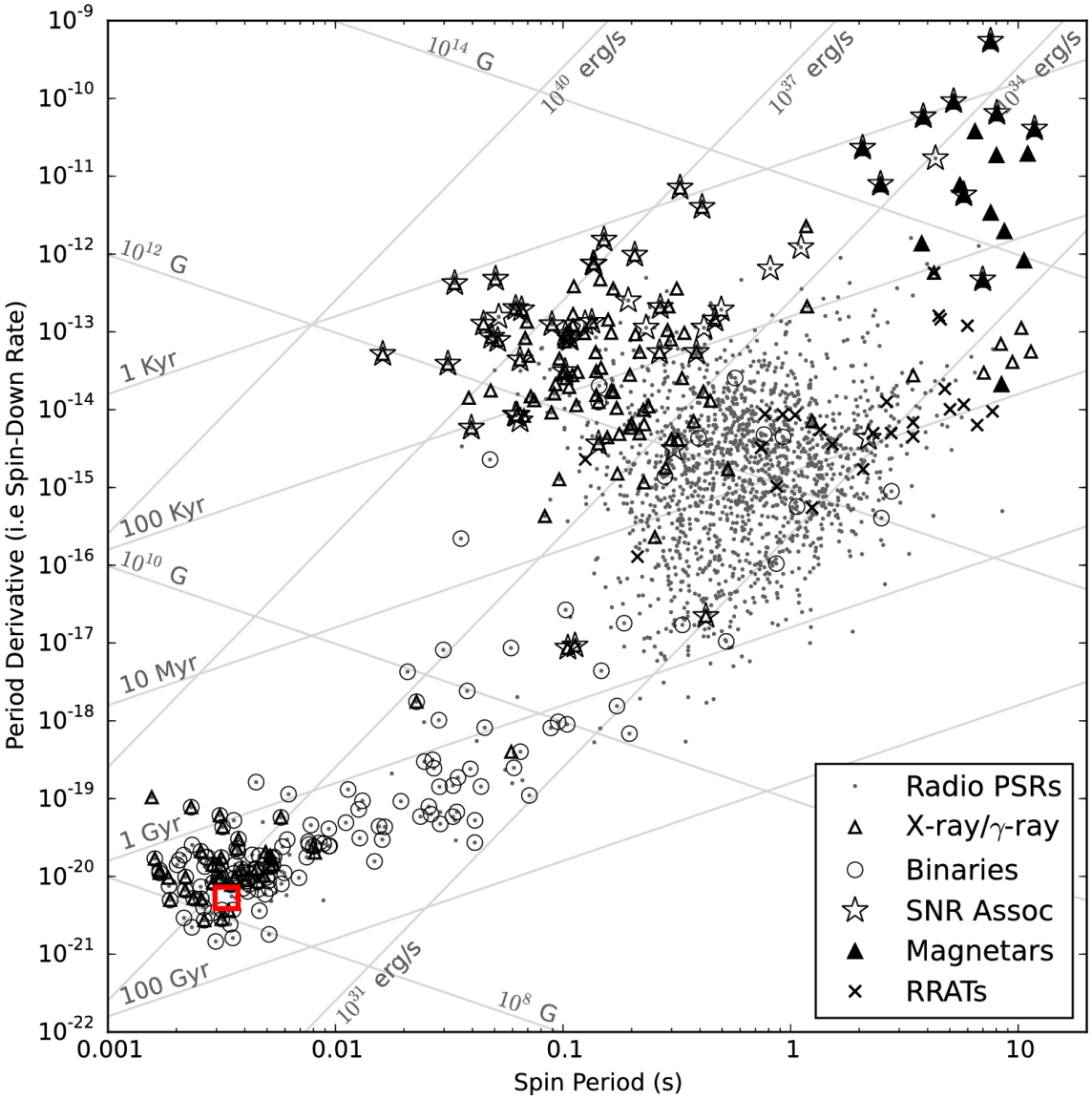

Figure 1.2: A diagram of a large pulsar population in the $P - \dot{P}$ plane. The pulsar's position in this diagram gives information of its characteristic age $\tau = P/2\dot{P}$, spin-down power $\dot{E} \equiv 4\pi^2 \dot{P}/P^3$ and magnetic field strength $B_c = 3.2 \times 10^{19}(\sqrt{P\dot{P}})$ G as indicated by the different contour lines for these properties. In the lower left of the diagram, we observe the MSPs. Most of them are in binary systems and have been spun up by accretion from their companion giving them a very low rotational period. The black widow spider studied in this work, PSR J1720-0533 (see Section 1.6), is indicated by the red square. Figure credit: Condon and Ransom, *Essential Radio Astronomy*, Charlottesville: NRAO, 2015 [7].

stars' periods to very high precision, and their low spin-down rates make neutron stars extremely accurate cosmic clocks.

P and $\dot{P}$ allow us to define some other characteristic properties of neutron stars [7, 8]. First, the spin-down power of the star can be defined by considering the time derivative of the rotational energy, $\mathrm{d}E/\mathrm{d}t$, where $E = I\Omega^2/2$. Here, I is the moment of inertia of the neutron star, which is often assumed to be the canonical value of $I \approx 10^{45}\,\mathrm{g\,cm^2}$, and Ω is the angular velocity. Since we expect the rotational period to increase over time ($\dot{\Omega} < 0$), we take the negative of the time derivative to define the spin-down power of neutron stars as $\dot{E} \equiv -\mathrm{d}E/\mathrm{d}t = -I\Omega\dot{\Omega}$. With $\Omega = 2\pi/P$ we can rewrite this as

$$\dot{E} = \frac{4\pi^2 I \dot{P}}{P^3}. \tag{1.3}$$

$\dot{E}$ is an important property of the neutron star as it quantifies the energy available to produce the electromagnetic emission and particle winds.

Assuming that the spin-down power equals the rate of emission of magnetic dipole radiation, it can be shown that $P\dot{P}$ is not changing over time [7]. Thus, we can write the identity $P\mathrm{d}P = P\dot{P}\mathrm{d}t$ and integrate over the pulsars age:

$$\int_{P_{\mathrm{NS},0}}^{P} P\,\mathrm{d}P = \int_0^{\tau} P\dot{P}\,\mathrm{d}t = P\dot{P}\int_0^{\tau}\mathrm{d}t. \tag{1.4}$$

Integrating and assuming that the initial neutron star rotational period ($P_{\mathrm{NS},0}$) is much less than its current period (P), we define the characteristic age of the neutron star as

$$\tau \equiv \frac{P}{2\dot{P}}. \tag{1.5}$$

Finally, again assuming that the spin-down power is equal to the rate at which magnetic dipole radiation is emitted and that the magnetic field axis is aligned with the rotational axis, it can be shown that the characteristic magnetic field strength at the neutron star surface is

$$B_c = 3.2 \times 10^{19}(\sqrt{P\dot{P}})\ \mathrm{G}. \tag{1.6}$$

These characteristics can be plotted in a $P - \dot{P}$ diagram, as shown in Figure 1.2, to get an idea of the range of $\dot{E}$, τ and B_c values observed in the full neutron star population and how these compact objects evolve over time.

1.4 Neutron star population

Astronomers use a classification system to distinguish the different types of neutron star systems they observe. The first major distinction is between isolated and binary systems. The isolated systems include *central compact objects*, which are young neutron stars that show no pulsations, commonly associated with SNRs. When a pulsed radio, X-ray, or γ-ray emission is observed the neutron star is classified as a *pulsar*. In some cases of very young pulsars, the magnetic field can be amplified by a dynamo effect originating from the parent star. These objects can have a magnetic field strength on the scales of $B \sim 10^{14} - 10^{16}\,\mathrm{G}$ and are known as *magnetars* [9].

In binary systems, the evolution of the neutron star is also dependent on the companion, leading to several new classifications. If a neutron star in a binary system is close enough to its hydrogen-rich companion, the outer layers of the companion can extend outside its Roche lobe and be pulled towards the neutron star, as illustrated in Figure 1.3. This phenomenon is called mass transfer. The in-falling matter starts to spiral in towards the neutron star, and if enough matter is transferred, an *accretion disk* can form. In the process, heat is created in the disk leading to thermal X-ray emission, and hence, the systems in this accretion state are classified as Low Mass X-ray Binaries (LMXBs).

On long timescales, the accreting matter induces a torque on the neutron star, causing its rotational frequency to increase up to several hundred rotations per second. This leads to a new branch of the neutron star population, called *recycled millisecond pulsars* (MSPs). MSPs are characterized by fast spin rates with rotational periods less than 30 ms, where the fastest observed MSP, PSR J1748-2446, has a rotational period of just 1.4 ms [10]. If MSPs are actively accreting

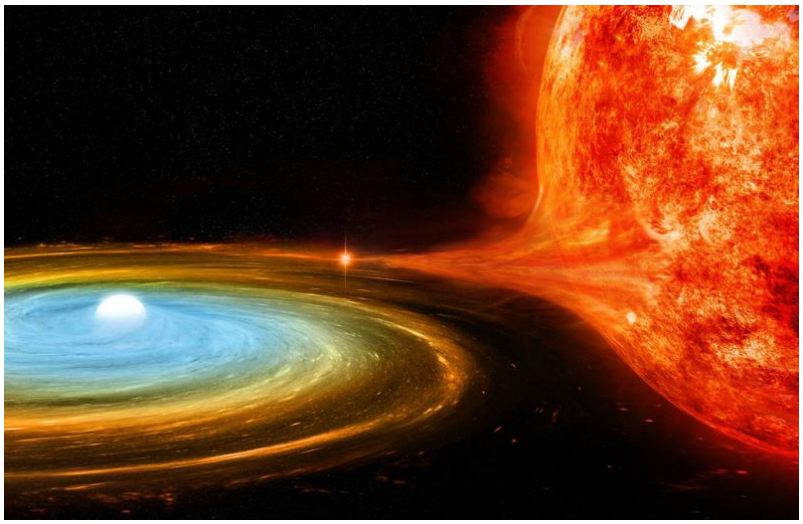

Figure 1.3: Artist's illustration of a neutron star accreting matter from a nearby companion star. Credit: NASA/CXC/M. WEISS.

matter from their companions they are called accretion-powered MSPs, forming a sub-class of LMXBs. Otherwise, they are classified as rotation-powered MSPs (RMSPs). Some MSPs are observed to transition between these two states [11] and are classified as transitional MSPs. MSPs are typically found in the lower-left corner of the $P - \dot{P}$ diagram and consist of older neutron stars with weaker magnetic field strengths.

1.4.1 Spiders: compact binary millisecond pulsars

RMSPs can be further classified based on their companion's mass (M_c), leading to a subgroup of RMSPs called *spider binaries*. Spider binaries consist of *redbacks* and *black widows* which are MSPs with a hydrogen-rich main sequence companion star with a low mass $M_c \gtrsim 0.1 M_\odot$, or a brown dwarf companion with a very low mass $M_c \lesssim 0.06 M_\odot$, respectively. Both types of systems are in tight orbits, with orbital periods of $P_{\rm orb} \lesssim 1\,{\rm d}$. The tightest orbit measured for a spider binary is in the black widow candidate ZTF J1406+1222 with an observed orbital period of 62 minutes [12]. These tight orbits expose the companion stars to high energy emissions from the MSPs. This irradiation heats up the inner face of the companion facing the MSP (see Figure 1.4), leading to variable emission observable from Earth, which allows astronomers to measure the orbital parameters of the system.

The strong pulsar wind ejects matter away from the companion star and are believed to be the leading reason for the complete dissolution of the companion in a few isolated MSPs [13]. This destructive process is analogous to the cannibalistic nature of some spider species, which explains the naming of this sub-group of RMSPs. When the companion is close to inferior conjunction, the ejected matter can lead to a total disappearance of the radio pulses from the neutron star, in the phenomenon called *radio eclipses*.

Currently, more than 50 spider binaries have been identified [14], located at distances on the scales of $\sim 0.2 - 1\,{\rm kpc}$. The high-energy γ-ray emission from these spider systems originates from the pulsar's magnetosphere, with γ-ray luminosities observed in the range of $L_\gamma \sim 10^{32} - 10^{34}\,{\rm erg\,s^{-1}}$. In Chapter 4, we will see that only 6 out of the 56 spiders considered in this study do not exhibit detectable γ-ray emission. This small number of spiders with non-detected γ-ray emission results from a detection bias, as many of the spiders are initially identified through γ-ray source associations. The most probable reasons for the non-detection of γ-rays are geometrical effects, low $\dot{E}$-values, large distances, or high background contamination.

Some spiders also exhibit extended X-ray and optical emissions resulting from the influence of the pulsar wind on the surrounding interstellar medium. In the 1988 paper by Kulkarni and Hester [15] they discovered a pulsar wind nebula (PWN) surrounding the eclipsing black widow pulsar B1957+20, which was found to originate from Hα-emission induced by shocks driven into the interstellar medium by the relativistic pulsar wind. Later, in a 2003 paper by Stappers et al.

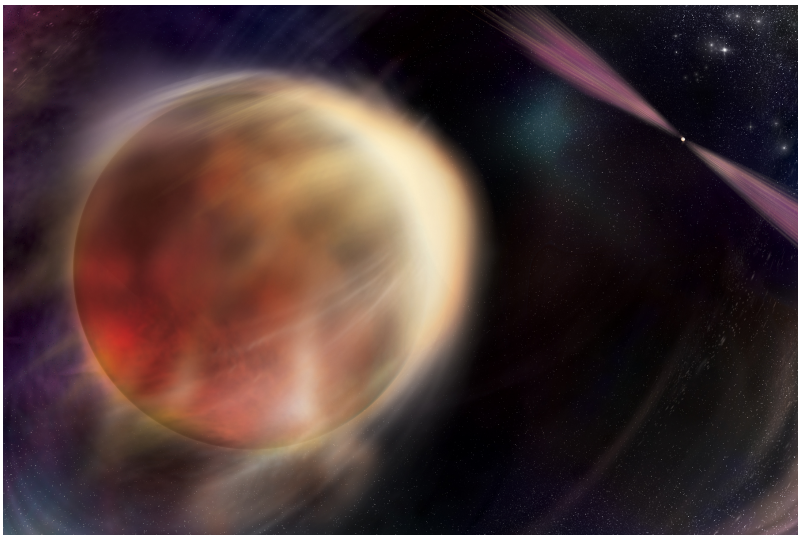

Figure 1.4: Artist's illustration of a spider binary system. The strong pulsar wind produces matter outflows from the companion leading to eclipses. The multi-wavelength emission from the pulsar heats up the inner face of the companion. Credit: NASA/Sonoma State University, Aurore Simonnet.

[16], an X-ray nebula was observed around the same black widow system, and the nature of this emission was attributed to the shock in the region where the pulsar wind and the companion wind collide.

Studying the spider population can help us understand the extreme physical conditions in the vicinity of the neutron star. Therefore it is important to observe, model, and explain the physical origins of the broad-band emission this subset of MSP exhibits.

1.5 Pulsar emission models

To understand how rotating neutron stars emit electromagnetic radiation across the broad-band spectrum, from radio waves to TeV γ-rays, it is necessary to understand the geometry of the surrounding magnetic fields. The first important note is that the rotational and magnetic axes are not necessarily aligned. The angle between the two is called the *obliquity* and is denoted by α. The magnetic field lines co-rotate with the neutron star and define a cylindrical boundary where the co-rotating field lines reach the speed of light. This boundary is known as the *light cylinder*, with a radius $R_{\rm LC} = c/\Omega$, where c is the speed of light and Ω is the angular velocity of the star. At this boundary, the magnetic field lines can no longer stay closed and instead open up, ejecting charged particles out of the system and giving rise to a beamed pulse of electromagnetic radiation. The combined effects of α and $R_{\rm LC}$ give rise to a complex geometry of the magnetosphere, which can be seen in Figure 1.5.

The creation e^+e^- pairs in the magnetosphere of neutron stars is a key process for generating the observed broad-band emission [17]. Quantum electrodynamic effects can convert a photon traveling through a magnetic field into an e^+e^- pair if its energy is sufficiently high [18], with an energy threshold of $\epsilon > 2mc^2/\sin\theta$, where θ is the angle between the photon momentum and the local magnetic field. Moreover, two photons can interact and produce e^+e^- pairs as well. The latter process is important at larger distances from the neutron star surface where the magnetic field is weaker. The produced e^+e^- pairs then accelerate in voltage drops in different areas of the magnetosphere. As these charged particles are accelerated to relativistic velocities and their trajectories are bent by the magnetic fields, they emit *synchrotron radiation* (SR). The energy of these emitted photons depends on the velocity of the particles, the strength of the magnetic field, and the angle between the velocity vector and the local field. Furthermore, if these particles interact with background photons, they can transfer some of their kinetic energy to the photons in the process of inverse Compton scattering (ICS), which generates higher-energy photons. The

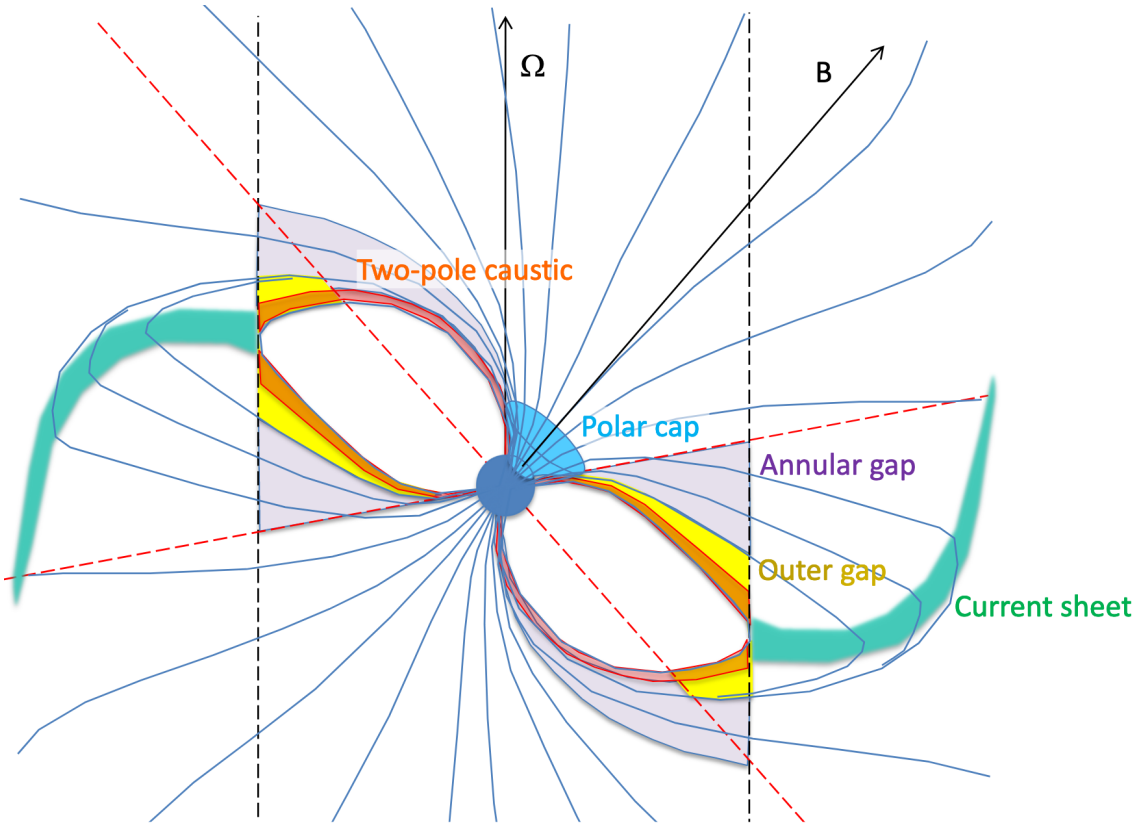

Figure 1.5: A model figure of the magnetosphere of a rotating neutron star with a dipolar magnetic field. The shaded areas indicate where the different emission models place the voltage gaps which are responsible for accelerating particles into relativistic velocities. The light cylinder is indicated by the verticle dashed lines, and the diagonal dashed lines indicate the null charge surfaces. The figure shows the complex geometry of the magnetosphere resulting from the combined effects of the obliquity and the light cylinder. Figure credit: Alice K. Harding. *The Emission Physics of Millisecond Pulsars*. In: Millisecond Pulsars, 2022 [17].

photons produced by SR or ICS can again convert into new particle pairs, resulting in cascades of energetic particles filling the magnetosphere of the pulsar. The question now is where in the pulsar's magnetosphere is it possible to accelerate particles to sufficient relativistic velocities to produce the observed γ-ray emission. This question leads to the different emission models associated with magnetospheric regions, as shown in Figure 1.5.

Most of the radio emission from MSPs is believed to originate from the regions above the polar caps, which are the regions on the neutron star's surface limited by the last open field lines above the magnetic poles. Charged particles are accelerated in these open field lines and emit radio waves due to SR and ICS. Additionally, some of the charged particles are accelerated toward the magnetic poles, and on impact with the surface, they scatter in the neutron star's thin atmosphere, transferring thermal energy to the surrounding area and emitting thermal radiation with energies up to X-rays [19]. This process is observed as hot spots on the neutron star's magnetic poles [20, 21].

Compared to normal pulsars, MSPs exhibit more complicated radio emissions with wider, more complex pulse profiles and polarization patterns that are more challenging to interpret [17]. Since the surface magnetic fields of MSPs are much lower than for normal pulsars ($B \sim 10^8$ G), the e^+e^- pair production required for pair cascades and radio emission is more difficult than for normal pulsars. Therefore, it is suggested that there exists a more complex multipole magnetic field close to the neutron star surface that can produce the observed emission.

The high-energy emission models for MSPs are believed to be quite similar to those for normal pulsars. Early models of high-energy radiation invoked the same polar cap model used for normal pulsars. However, due to insufficient particle energies in the polar voltage gap, subsequent models suggested that the emission instead originates from close to but inside the light cylinder. This

Figure 1.6: FAST viewed from above. Image credit: Liu Xu, Xinhua News Agency.

resulted in the *outer gap* (OG) [22], *two-pole caustic* (TPC) [23], and *annular gap* models [24, 25]. The differences between these models lie in which voltage gap the particles accelerate in. The OG and TPC models place the high-energy emission in the voltage gaps close to the last open field line. While the TPC model exhibits radiation all the way from the neutron star surface to the light cylinder, the OG emission is confined to the region between the *null charge surface* and the light cylinder. The null charge surface is defined as the surface where the magnetic field is perpendicular to the rotational axis of the pulsar ($\mathbf{\Omega} \cdot \mathbf{B} = 0$), and is indicated by the diagonal dashed lines in Figure 1.5. The annular gap model places the voltage gap in the annular region of the magnetosphere, defined by the region between the *critical field line* and the last open field line, where the critical field line is the field line that crosses the null charge surface at the light cylinder.

Thanks to the many detected γ-ray pulsations in normal pulsars and MSPs by the *Fermi-LAT* (see Section 2.1), modern-day magnetospheric models favor placing the high-energy emission in the *current sheet* of the magnetosphere. Particles ejected along the open field lines can be returned to the star through this sheet, which is located outside of the light cylinder in the region close to where the magnetic field changes polarity. Relativistic particles accelerated in this large region, reaching up to $r \sim 50 - 100\, R_{\rm LC}$, produce γ-ray photons by Doppler-boosted SR [17]. The emission would appear to pulsate as the sheet crosses the line of sight, explaining the observed γ-ray pulsations.

Although Figure 1.5 provides a useful representation of the neutron star magnetosphere based on a simple rotating dipole model, it is now clear from analytical and observational evidence that a more complex multipole solution must exist for the magnetic field close to the neutron star surface. Miller et al. 2019 [26] and Riley et al. 2019 [27] discovered multiple surface hot spots on the same hemisphere of the MSP PSR J0030+0451, implying the existence of a more complex multipolar structure of the magnetic field. Such a magnetic field configuration introduces new parameters into the emission models, further complicating the problem. Thus, continued research on neutron stars is crucial to improve our current understanding of their emission mechanisms and gaining confidence in our models.

1.6 The black widow millisecond pulsar PSR J1720-0533

PSR J1720-0533 is a black widow MSP discovered in 2021 by the Chinese Five-hundred-meter Aperture Spherical Telescope (FAST, see Figure 1.6) during the ongoing Commensal Real-Time ASKAP Fast-Transients (CRAFT) survey [28]. FAST is the world's largest single-dish radio telescope placed in the Dawodong depression in the southwest province of Guizhou [29]. The CRAFT

survey is looking for short-timescale radio transients and is discovering new radio pulsars with an angular resolution of about 3' [30].

PSR J1720-0533 was discovered in a 3.16-hour orbit with a $M_c \gtrsim 0.034\,\mathrm{M}_\odot$ brown dwarf companion positioned at a high Galactic latitude of $b = 17.25°$. The pulsar has a rotational period of $P = 3.26\,\mathrm{ms}$ and a spin-down rate of $\dot{P} = 7.46 \times 10^{-21}$ before Shklovskii correction (see Section 4.2.2). This results in a spin-down power of $\dot{E} = 0.85 \times 10^{34}\,\mathrm{erg\,s^{-1}}$, placing it in the lower-left corner of the $P - \dot{P}$ diagram. The pulsar was discovered with a dispersion measure distance of $d = 191\,\mathrm{pc}$ using the electron density model of Yao et al. 2017 [31] making it the closest known spider binary to date [32]. However, distances calculated by the dispersion measure technique are known to be associated with relatively large uncertainties compared to other distance estimate techniques. For instance, the Second Fermi-LAT Catalog for γ-ray pulsars (2PC) [33] uses a 20% uncertainty on the dispersion measure distances. This is taken under consideration in the conducted γ-ray analysis of PSR J1720-0533 (see Chapter 4).

At the beginning of writing this thesis, little was known about the multi-wavelength counterparts of this newly discovered black widow, thus making it an interesting target for a high energy γ-ray emission analysis using the Fermi Large Area Telescope.

Chapter 2

The Fermi Observatory

The Fermi γ-ray Space Telescope (formerly known as the Gamma-ray Large Area Space Telescope (GLAST)), is a space-based observatory designed to monitor the γ-ray sky. It was launched on June 11, 2008, into a circular low-Earth 96-minute orbit from Cape Canaveral Air Force Station (see Figure 2.1), and although it was originally designed to last between five to ten years, the observatory now enters its 15^{th} year of operation. The observatory is carrying two instruments: the Large Area Telescope (LAT), which is the primary instrument onboard Fermi (see Figure 2.2), and the Gamma-ray Burst Monitor.

Figure 2.1: Image of the launch of the Fermi γ-ray Space Telescope from Cape Canaveral Air Force Station. Image credit: United Launch Alliance, Carleton Bailie.

Before Fermi, extensive radio surveys with ground-based telescopes were the primary tool for detecting pulsars [34]. After a successful launch and deployment, the Fermi-LAT with its all-sky survey capability has been crucial in the rapid increase of discoveries of MSPs and spider binaries like PSR J1720-0533, mainly through targeted searches around unassociated Fermi-LAT sources. In fact, the upcoming Third Fermi-LAT γ-ray Pulsar Catalog (3PC) will contain over 100 MSPs and, in total, around 300 pulsars detected and analyzed by the Fermi-LAT collaboration[1] using more than nine years of data [35].

2.1 The Large Area Telescope

Since high-energy γ-rays cannot be reflected or refracted, they are detected indirectly by converting them into e^+e^- pairs, and from the deposited tracks and energies of these, it is possible to estimate the γ-ray's initial arrival direction and energy. The Fermi-LAT is one such high-energy pair-conversion telescope.

When a γ-ray photon enters the detector, it interacts with one of the thin, high-Z conversion foils and produces an e^+e^- pair, as illustrated in Figure 2.2b. The pair is then tracked by multiple layers of thin silicon strip detectors as the particles travel deeper into the instrument. These tracks are used to estimate the arrival direction of the original γ-ray photon. Finally, the pair is absorbed by the calorimeter where their total deposited energy is measured. With the

[1] See https://glast.sites.stanford.edu/

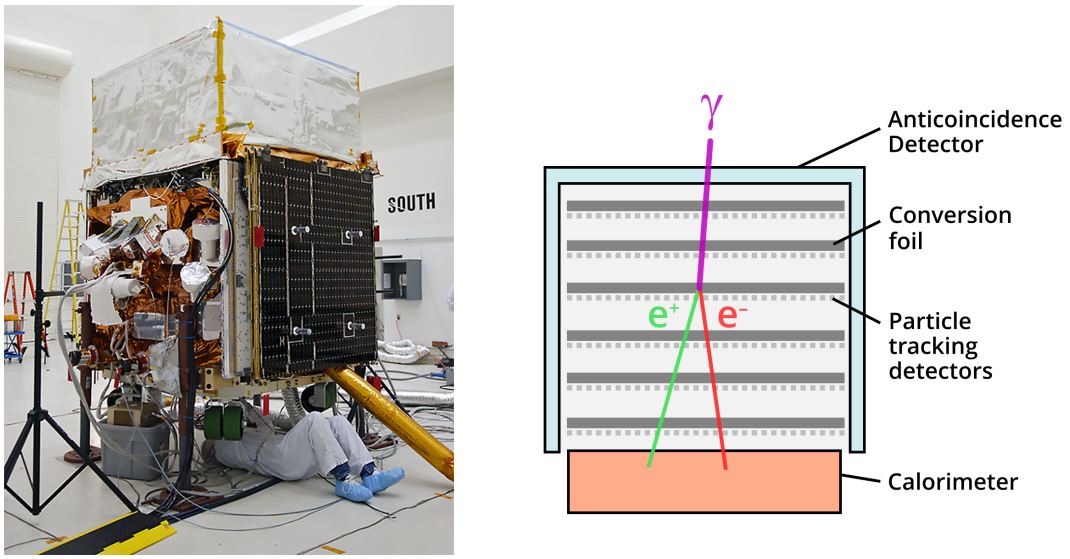

(a) (b)

Figure 2.2: Left (a): Construction of the Fermi observatory with the Fermi-LAT mounted on top. Image credit: NASA/General Dynamics Advanced Information Systems. Right (b): Cross-sectional schematic of the Fermi-LAT showing how a γ-ray photon converts into an e^+e^- pair when interacting with the conversion foil. Figure credit: NASA's Goddard Space Flight Center Conceptual Image Lab.

information on the γ-ray event observed by the Fermi-LAT, the instrument calculates the corresponding probabilities that it was a real γ-ray photon event, and classifies the event into different event classes and types, depending on the quality of reconstruction (see Section 2.1.1).

Figure 2.2b shows the anticoincidence detector surrounding the instrument. The assignment of this thin plastic cover is to reject events corresponding to cosmic rays, which can contaminate the data by also producing tracks in the silicon strips [36]. Since cosmic rays outnumber γ-rays by factors of $10^2 - 10^5$ [37], this is a crucial component in the reduction of background γ-ray contamination.

The wide field of view of the Fermi-LAT covers about 20% of the sky in the energy range from $\sim 20\,\mathrm{MeV}$ to $> 300\,\mathrm{GeV}$ [37]. The instrument is oriented around its zenith at all times but rocks from left to right on alternate orbits. This rocking motion, combined with the large field of view, enables the Fermi-LAT to cover the entire sky every two orbits. The precision of the reconstructed arrival directions of the γ-ray photons depends on their energy, where the 68% containment radius of the point spread function (PSF) of an on-axis γ-ray is less than 3.5° at $E_\gamma = 100\,\mathrm{MeV}$ and less than 0.15° at $E_\gamma > 10\,\mathrm{GeV}$.

The sub-degree resolution of the Fermi-LAT at higher energies makes it an essential tool for discovering new pulsar candidates. Blind searches with ground-based telescopes can be time-consuming and unsuccessful, but the Fermi-LAT can provide locations of pulsar candidates that can be utilized in multi-wavelength observations. This is one of the reasons that the Fermi-LAT has been a game changer in pulsar astronomy and a significant contributor to the increase of pulsar identifications.

2.1.1 γ-ray events: classes and types

When a γ-ray photon enters the Fermi-LAT, the information collected by the instrument is saved in an event file. To distinguish between events of varying quality, the γ-ray photon events are classified into classes and sub-partitions with respect to the quality of their energy measurement and reconstruction of their arrival direction. The quality of the reconstructed γ-ray photon depends on factors such as the arrival inclination angle, energy, and detector energy losses. The event classes are characterized by their own set of instrument response functions (IRFs), which map the photon

Table 2.1: The different partitions and event types of the γ-rays classified by the Fermi-LAT. The table is retrieved from the NASA Fermi-LAT website.

Conversion type partition		
Event type	`evtype`	Description
Front	1	Events converting in the front section of the tracker.
Back	2	Events converting in the back section of the tracker.
PSF type partition		
Event type	`evtype`	Description
PSF0	4	First (worst) quartile in the quality of the reconstructed arrival direction.
PSF1	8	Second quartile in the quality of the reconstructed arrival direction.
PSF2	16	Third quartile in the quality of the reconstructed arrival direction.
PSF3	32	Fourth (best) quartile in the quality of the reconstructed arrival direction.
EDISP type partition		
Event type	`evtype`	Description
EDISP0	64	First (worst) quartile in the quality of the reconstructed energy.
EDISP1	128	Second quartile in the quality of the reconstructed energy.
EDISP2	256	Third quartile in the quality of the reconstructed energy.
EDISP3	512	Fourth (best) quartile in the quality of the reconstructed energy.

observables into the event parameters and assign the probabilities of an event being a real photon[2]. The classes are nested in a hierarchical manner, where more restrictive classes are subsets of the less restrictive ones. The most restrictive classes are characterized by narrower PSFs at the expense of lower effective areas. For most analyses, the Fermi science team recommends the `P8R3_SOURCE` class of events, with event class number `evclass` = 128. This class is a high-probability photon class, with a good balance between low background contamination and effective area which is suitable for most analyses of point sources and moderately extended sources.

Within each event class, the Fermi-LAT further partitions events into different event types based on the quality of the PSF and deposited energy, and where in the detector the photon was converted. To achieve a narrow PSF at low energies, the high-Z photon converters need to be thin. However, this compromises the effective area of the telescope at higher energies. To address this issue, the Fermi-LAT team divided the tracker into a 'front' and 'back' section, where the back section converters are 6 times thicker than the front section converters and therefore have a larger effective area at the expense of a factor $\lesssim 2$ loss in angular resolution at 1 GeV energies [36]. This leads to the first partition of the Fermi-LAT events, where we find two event types depending on whether the photon is converted in the front or back section of the instrument. The second partition divides the events into four different types depending on the quality of the PSF. The worst quartile of reconstructed arrival directions falls into the first type, the second worst quartile into the second, and so on. Similarly, the accuracy of the deposited energy partitions the events into four quartiles in a similar manner. Thus, in total, the Fermi-LAT labels the γ-ray photon events with 3 out of a total of 10 different event types, including one for the front or back conversion partition, one for the four quartiles in the PSF partition, and one of the four quartiles for the deposited energy partition. With these, the event type(s) can be carefully selected depending on the science goals for analyzing the Fermi-LAT data. An overview of the event types of the Fermi-LAT is provided in Table 2.1, and more detailed explanations of all event classes and event types are available at the Fermi-LAT websites[3].

2.2 Likelihood Analysis

After classifying events as γ-ray photons we consider the events as photon 'counts'. It is though important to distinguish these event counts from a classical exposure on a CCD. First of all, the Fermi-LAT is constantly scanning the sky for photons within the field of view. When running the data selection for a region of interest (ROI) the counts map can mimic a classical exposure, but there are connected uncertainties in the photon energy and the reconstructed arrival directions to

[2]See https://fermi.gsfc.nasa.gov/ssc/data/analysis/documentation/Cicerone/Cicerone_LAT_IRFs
[3]See https://fermi.gsfc.nasa.gov/ssc/data/analysis/documentation/Cicerone/Cicerone Data/LAT DP.html

take into account. Hence, for the Fermi-LAT, a cluster of photon counts cannot be classified as a source based on the counts' angular positions only. To make a quantitative analysis, it is necessary to fit a source model to the event data and calculate probabilities that the model will reproduce the observed data. For the Fermi-LAT, this is done using a likelihood analysis.

The likelihood $\mathcal{L}$ is the probability of obtaining the observational data given an input model. For the Fermi-LAT the data are the γ-ray photon events and the model is a distribution of γ-ray sources in the sky, including their spatial and spectral shapes. To calculate the expected data produced by a given source model, it is crucial to have sufficient knowledge about the IRFs and the exposure time of the ROI. This calculation is explained further in Section 2.4.

After a model is acquired, we wish to determine the best-fit values for the spectral parameters of the model sources. By performing a χ^2 minimization algorithm to fit the spectral parameters, the likelihood of the model is expected to be maximized. For the Fermi-LAT, there are five different χ^2 minimization algorithms, including the MINUIT and NEWMINUIT algorithms [38], where the latter is used in the analysis of this work (see Chapters 3 and 4). While fitting the spectral parameters of the model sources maximizes the likelihood of the model, we can also re-localize sources to their maximum likelihood position to improve the global likelihood of the model (see Section 2.5).

2.3 The functional form of the likelihood

The likelihood analysis can be implemented in two different ways: the binned and the unbinned analysis. To understand their differences, we need to look at the likelihood's functional form. The likelihood $\mathcal{L}$ is a product of probabilities of observing the counts given an input model. As the detector does not have any pixels, the counts can be assigned to bins of arbitrary sizes. Given a source model, we can estimate the expected number of counts, m_i, in each of the i bins using the IRFs and exposure maps (see Section 2.4). As the number of counts is characterized by Poissonian statistics, the probability of detecting n_i counts in the i^{th} bin is given by

$$p_i = \frac{m_i^{n_i} \mathrm{e}^{-m_i}}{n_i!}, \tag{2.1}$$

where n_i is the observed counts in the data. The likelihood, $\mathcal{L}$, is the product of all these probabilities over all bins. Due to the product properties of the exponential, we can factor out the exponentials from the product and have a factor solely determined by the total number of expected counts in the model, N_{exp}:

$$\mathcal{L} = \prod_i p_i = \prod_i \frac{m_i^{n_i} \mathrm{e}^{-m_i}}{n_i!} = \mathrm{e}^{-\sum_i m_i} \prod_i \frac{m_i^{n_i}}{n_i!} \tag{2.2}$$

$$= \mathrm{e}^{-N_{\mathrm{exp}}} \prod_i \frac{m_i^{n_i}}{n_i!}. \tag{2.3}$$

Equation (2.3) is the basis for the binned likelihood analysis. However, binning the counts in this manner lose information about the individual counts. If we let the bin size decrease, the resulting likelihood is increasingly more accurate. The unbinned likelihood arises in the limit where the bin sizes get infinitesimally small. It logically follows that $n_i = \{0, 1\}$, and (2.3) now becomes:

$$\mathcal{L} = \mathrm{e}^{-N_{\mathrm{exp}}} \prod_i m_i, \tag{2.4}$$

where i now indicates the count index. The reduction of bin size results in increased accuracy, but the trade-off is increased calculation times of the likelihood. For a sufficient number of counts, the unbinned analysis becomes too computationally expensive and the binned likelihood is necessary.

A very useful parameter used in the likelihood analysis is the Test Statistic (TS), which is defined as

$$\mathrm{TS} = -2(\ln\mathcal{L}_{\mathrm{max},0} - \ln\mathcal{L}_{\mathrm{max},1}), \tag{2.5}$$

where $\mathcal{L}_{\mathrm{max},0}$ is the maximum likelihood of the null hypothesis model, and $\mathcal{L}_{\mathrm{max},1}$ is the maximum likelihood of the new model we want to investigate. As TS increases as $\mathcal{L}_{\mathrm{max},1}$ increases, it is clear to see that maximizing the TS-value for a model source is equivalent to maximizing the likelihood of

the model. Thus the TS-value can be used to move sources to their maximum likelihood positions, detect new sources, optimize the spectral curvature of a source, and test for a spatial extension by imposing an extended spatial template on a source (see Section 3.1). A large TS-value means the new model is highly favored over the old model, and as a rule of thumb, the TS-value is approximately the square of the detection significance (TS $\approx \sigma^2$). Thus, the improvements of the models are quantified using the TS-value which is directly correlated with the significance of detection.

2.4 The Fermi-LAT data preparation

Any Fermi-LAT analysis starts from the data query on the Fermi-LAT websites[4]. Here we access the Fermi-LAT data of the ROI and make cuts on the energy and time ranges. In theory, the whole γ-ray sky could influence the ROI, but in practice, the effect from sources a few tens of degrees away is negligible. Hence, to reduce the computational load, the data are cut at a given search radius from the center coordinates in the query. In addition to the event data files, the information on the spacecraft within the time range is given. This is later used to make good time intervals (GTIs), exposure maps, *livetime* cubes, and source maps.

After the data are retrieved, the events need to be sufficiently cut depending on several criteria. First of all, it is necessary to make cuts on the maximum zenith angle of the events. This is to filter out γ-ray contamination from photons produced in Earth's limbs. Secondly, the event type(s) must be specified. As mentioned above (see Section 2.1.1), we can choose the event type(s) within an event class that is(are) most fitting for the analysis. For example, a morphological analysis (see Chapter 3) might want to take advantage of the events with the highest quality on the reconstructed arrival directions (`evtype` = 32). To achieve more counts, the analysis can include multiple event types by summing over their event type number. To include events corresponding to the upper half in the quality of reconstructed direction, we choose `evtype` = 48. To include all events within an event class, we can choose `evtype` = 3 which encompasses events hitting both the front and the back sections of the tracker.

When utilizing multiple event types in an analysis, we can obtain increased global accuracy (with the expense of increased computational load) by splitting the event types into independent likelihood analyses in the so-called *joint likelihood* analysis [39]. With this implementation, the maximum likelihood analyses are done in parallel, but independent of the different event types. The product of the individual likelihoods produces the joint likelihood. The estimation of model parameters across disjoint data sets is expected to increase the global accuracy of the data, and thus, the joint likelihood is the selected configuration for the analysis of this work (see Chapters 3 and 4).

The events within a selected ROI can only be considered to be valid if they are observed in a good time interval (GTI). Initially, the GTIs are the time intervals when the Fermi-LAT is collecting data. This excludes intervals when the Fermi spacecraft is exposed to increased background γ-ray contamination while transiting the Southern Atlantic Anomaly, and the rare occasions when the Fermi-LAT is undergoing software updates or the Fermi spacecraft is maneuvering. Since the ROI is not visible at all times during the selected time range, the GTIs need to be updated depending on the criteria made in the data selection. Thus the spacecraft data are used together with the relative position of the ROI in the sky to calculate the new GTIs. All events outside these new GTIs are filtered out.

Before the likelihood analysis can start, the *livetimes* and exposure maps of the ROI need to be calculated. The IRFs of the Fermi-LAT depend on the inclination angles of the incoming γ-rays, which is defined as the angle between the photon arrival direction and the Fermi-LAT normal. This fact means that the IRFs are constantly changing over time and also vary across the selected ROI. The predicted number of photons from a source in the ROI thus depends on the time it spends at a certain inclination angle in the time range of the data. This time-like quantity is named livetime and is a crucial part of getting accurate results in the likelihood analyses.

The exposure maps for the likelihood analysis differ from normal exposure maps. Instead of being integrals over effective area and time, the likelihood exposure maps are integrals of the total response function over the whole ROI data space. Thus the integral is over the measured energies

[4]See https://fermi.gsfc.nasa.gov/cgi-bin/ssc/LAT/LATDataQuery.cgi

(E'), directions $(\hat{p}')$, and time range (t). The exposure function is expressed by

$$\epsilon(E, \hat{p}) = \int_{\text{ROI}} dE' d\hat{p}' dt R(dE', d\hat{p}'; dE, d\hat{p}, t), \tag{2.6}$$

where R is the response function given by the livetime calculations. The software and pipelines to execute the data preparation are explained in Section 3.2.

2.5 The Fermi-LAT analysis

With precise information on the IRFs, GTIs, and exposure maps of the ROI, we are able to predict the expected observational data produced by an input source model. Hence, we can calculate the expected number of photons in each bin, m_i, and the likelihoods of different source models can be calculated using equation (2.3) or (2.4). Therefore, we are ready to begin a model-building process to analyze the observational data. However, the input source models do not necessarily need to start from scratch, as the Fermi-LAT collaboration publishes catalogs with the γ-ray properties of detected γ-ray sources. These catalogs are updated every few years as more data are obtained, and at the time of writing, the most recently updated catalog is the 4FGL-DR3 catalog, which was released in 2022 [40]. This is the third data release of the original Fermi Large Area Telescope Fourth Source Catalog (4FGL) [41]. In addition to these catalogs, the Fermi-LAT collaboration also provides models for diffuse galactic and isotropic γ-ray background radiation. These catalogs and background models give a good starting point for producing a baseline model in most analyses.

When a baseline model for the ROI is acquired, the general Fermi-LAT analysis follows a model-building technique by fitting the spectral components of the model sources with the χ^2 minimization algorithm, while looking for new source candidates. New candidate sources are identified by making a TS-map of the ROI. This map is produced by fitting the normalization of a test source with a suitable spectral parametrization (usually a power law spectral model with spectral index $\Gamma = 2$, see Equation (3.1)) in each bin in the ROI, and saving the obtained TS-value. Once the test source has iterated through each bin, a TS-map is produced by plotting all the TS-values over the grid positions as seen in Figure 2.3. New sources can be introduced at the TS-peaks in the map satisfying a given TS-value threshold. The existing model sources are not necessarily placed at their best-fit position, and can therefore be re-localized by making a local TS-map around its current position and moving it to the local TS-peak. Most Fermi-LAT analyses follow some iterative process of fitting spectral parameters, adding source candidates, and re-localizing existing sources. Figure 2.4 illustrates the model-building procedure performed in Chapter 3, and we observe how the model residual maps increasingly resemble the residual map of the observational data.

For this work, we have executed an extended source analysis of the source FHES J1723.5-0501 (see Chapter 3). This is performed by optimizing the ROI around this extended source with new candidate point sources and subsequently testing the source of interest for extended emission. This type of extended source analysis is explained in Section 3.1.

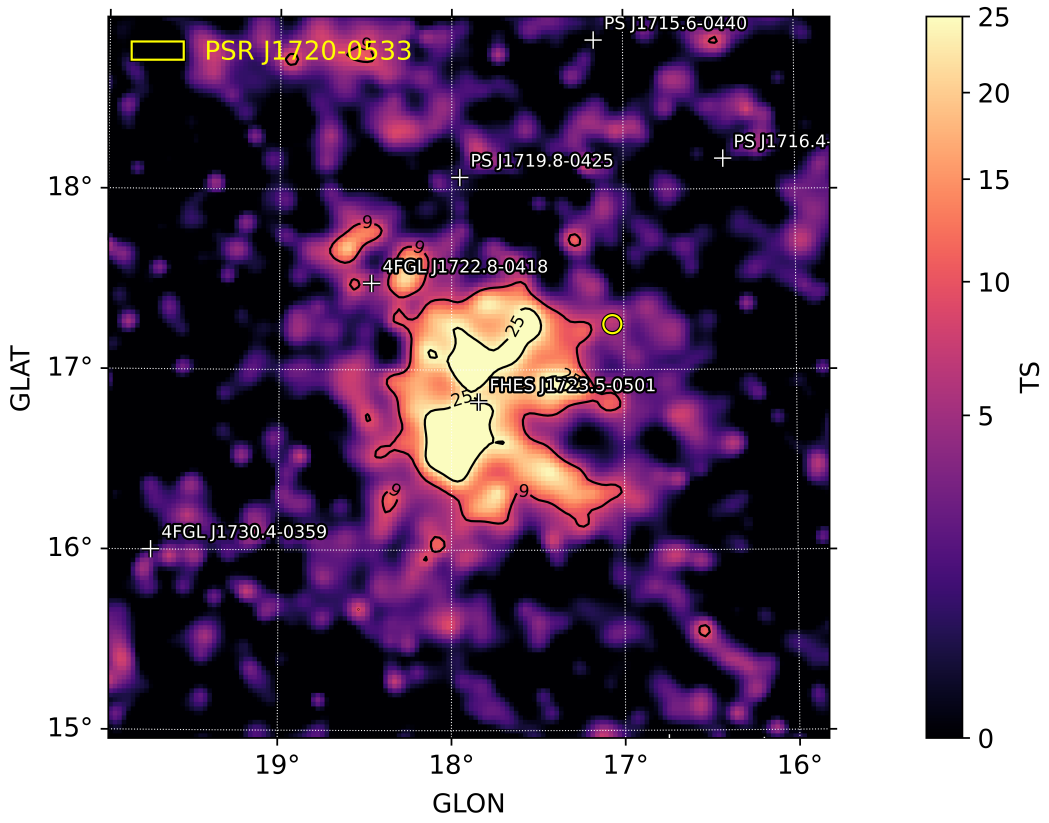

Figure 2.3: An example TS-map of a region including PSR J1720-0533 and FHES J1723.5-0501. The map is produced after optimizing the ROI (see Sections 3.1 and 3.4), using a test source with a power law spectral shape with $\Gamma = 2$. The current model consists of the Galactic and isotropic γ-ray background models, 4FGL catalog sources, and additional candidate point sources added during the optimization algorithm. The model sources are indicated by the white crosses and labels, and the yellow circle indicates the position of PSR J1720-0533 with the $3'$ uncertainty of FAST. The bright central source is the extended source FHES J1723.5-0501, which was excluded from the model when producing the TS-map, explaining the large TS-values observed in the central region.

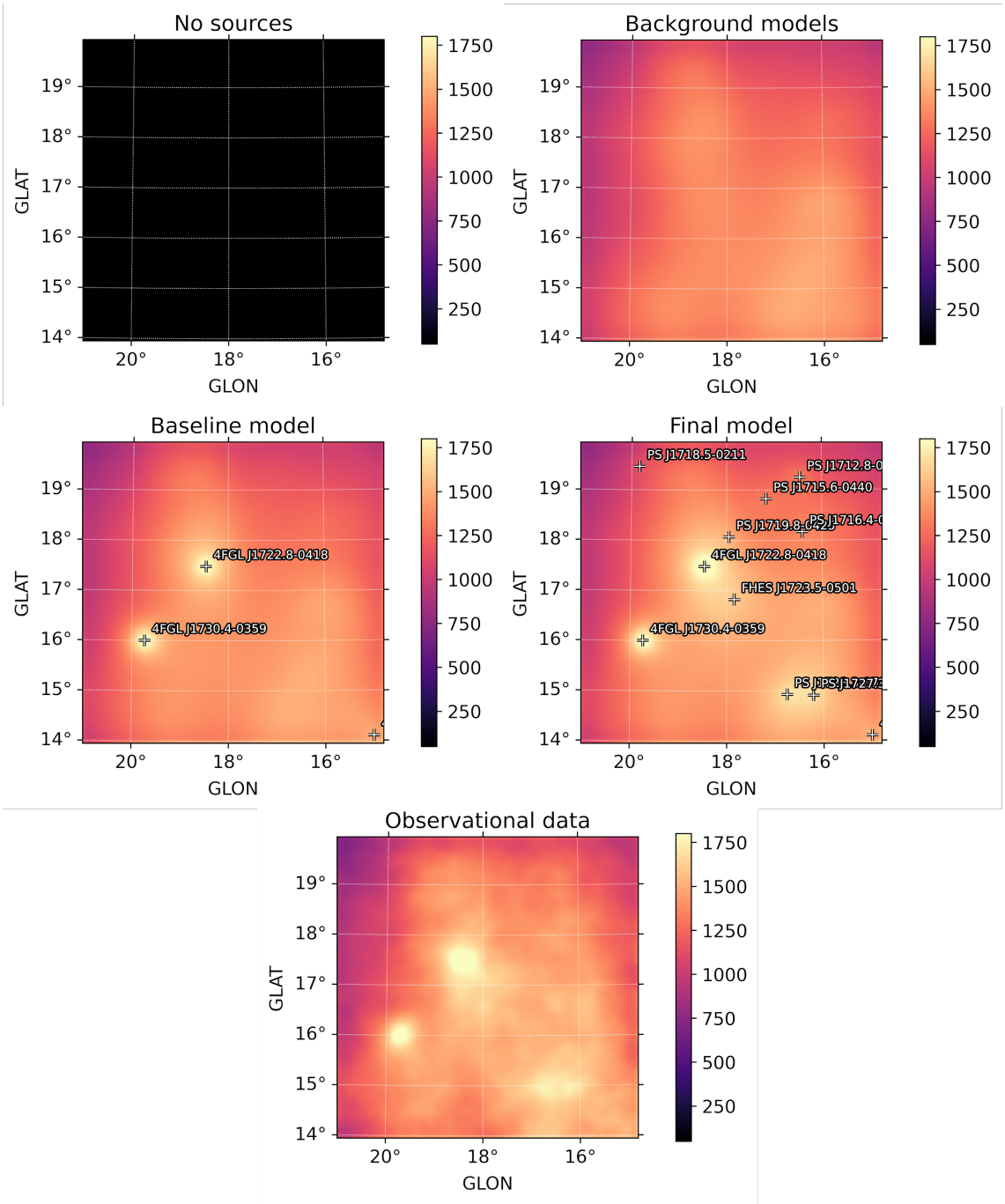

Figure 2.4: Residual maps of different steps in the model-building algorithm. The top left figure shows the residual map with no sources in the model and is correspondingly dark. At the top right, we have included the diffuse background emission from the Galactic and isotropic background models. The middle left figure shows the baseline model, where the Fermi-LAT catalog sources are included, and in the middle right, the residual map of the final produced model after adding candidate sources is shown. The maps increasingly resemble the observational data seen at the bottom of the figure.

Chapter 3

The Extended γ-ray Source FHES J1723.5-0501

In this Chapter, we study the extended (not point-like) γ-ray (GeV) source FHES J1723.5-0501, which is close to the black widow pulsar PSR J1720-0533, as seen in Figure 2.3. Ackermann et al. 2018 (A18 hereafter, [42]), presented the first Fermi High-Latitude Extended Sources Catalog (FHES), where they reported the discovery of 19 new extended sources, including FHES J1723.5-0501, using nearly eight years of Fermi-LAT data. FHES J1723.5-0501 was found to be centered at Galactic longitude $l = 17.90^\circ$ and latitude $b = 16.96^\circ$, thus resulting in an angular separation of only 0.85° to the black widow pulsar PSR J1720-0533 (see Section 1.6). A18 found the source to have a 68% containment radius of $R_{\rm ext} = 0.73^\circ \pm 0.10^\circ$ and also reported of an unclassified 1.4 GHz radio shell engulfed by the extended emission, suggesting its association with a type 1a SNR or a PWN.

In a recent study, Araya et al. 2021 [43] classified FHES J1723.5-0501 as a type 1a SNR, naming it G17.8+16.7, and estimating its distance to be in the range of $d = 1.4 - 3.5$ kpc, using the characteristic 1.4 GHz radio luminosity range for SNRs and SNR evolutionary models. While this distance estimate suggests that there is no connection between FHES J1723.5-0501 and PSR J1720-0533, it is important to note that the existence of PSR J1720-0533 was not considered in any of the mentioned analyses. Therefore, in Section 3.5, we revisit the possibility of a physical connection between the two sources by considering the energy budget between them, the Hillas criterion [44], and looking at the dust maps in the line of sight [45].

Regardless of the nature of FHES J1723.5-0501, precise modeling of the extended source is crucial to obtain accurate constraints on the pulsar's γ-ray emission, given the small angular separation. The next section explains the optimization algorithm used to model this extended source.

3.1 Extended source analysis

We model the extended source using a ROI optimization algorithm based on the algorithm presented in A18. The iterative analysis is shown in the flowchart in Figure 3.1. The analysis in A18 presents a procedure to discover extended sources around almost 2700 seeds of sources from 3FGL (Third Fermi-LAT Source Catalog [46]) and 3FHL (Third Fermi-LAT Catalog of High-Energy Sources [47]). As this analysis is a general procedure, all steps are not relevant for the particular ROI around FHES J1723.5-0501. The steps for this ROI are explained below, with some deviations from the A18 analysis explained. For more details on the analysis, see the original paper (A18).

The analysis starts from a baseline source model with the Galactic and isotropic background models, together with the Fermi-LAT catalog sources within a $10^\circ \times 10^\circ$ region centered at the central source. These models and catalogs are provided by the Fermi-LAT collaboration[1,2]. If there are high-energy sources from 3FHL in the ROI, these are also added to the baseline model. However, there are no such high-energy sources in the ROI around FHES J1723.5-0501. To ensure that the characterization of extension is not biased by the baseline model sources, all unassociated

[1] See https://fermi.gsfc.nasa.gov/ssc/data/access/lat/BackgroundModels.html
[2] See https://fermi.gsfc.nasa.gov/ssc/data/access/lat/12yr_catalog/

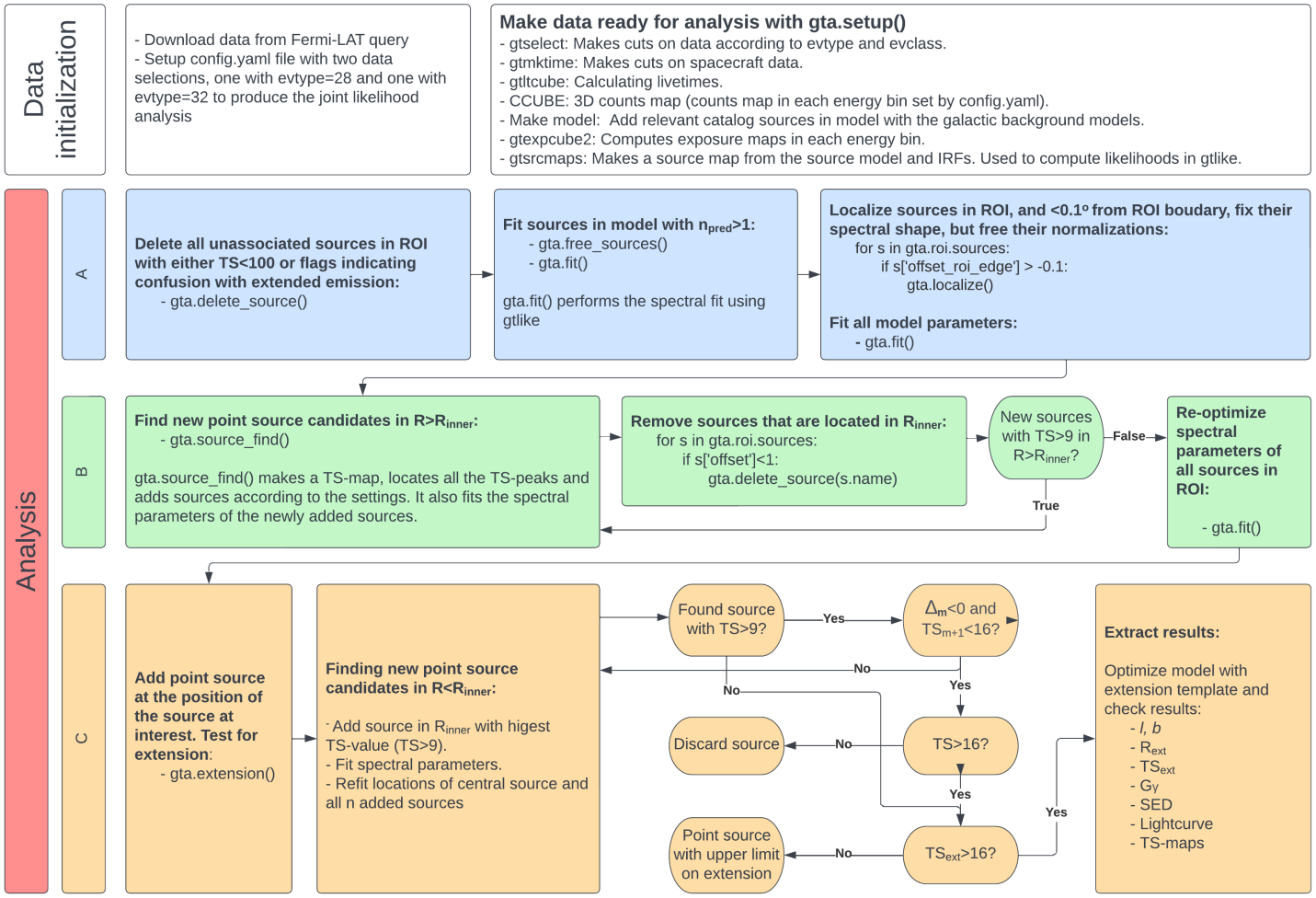

Figure 3.1: Flowchart of the analysis procedure. The procedure is based on the analysis produced by A18. The relevant functions from the `fermipy` software package are indicated in the chart for each step. See Section 3.1 for details.

sources with either TS < 100 or flags indicating confusion with extended emission are removed from the baseline model. If they indeed are real point sources, they will be added to the model in the source-finding algorithm later in the analysis. Next, we change the spectral model of all catalog sources with TS > 100 modeled with the power law (PL) spectral parameterization, given by

$$\frac{dN}{dE} = N_0 \left(\frac{E}{E_b} \right)^{-\Gamma}, \tag{3.1}$$

to a log-parabola (LP) model given by

$$\frac{dN}{dE} = N_0 \left(\frac{E}{E_b} \right)^{-(\alpha+\beta \ln(E/E_b))}. \tag{3.2}$$

We do this to ensure accurate modeling of background sources with undetected spectral curvature. As PL is a special case of LP ($\beta = 0$), this comes without loss of generality. In the spectral models above, N_0 is the flux normalization factor, E_b is the scale parameter, which is normally fixed, Γ and α are the spectral indexes of the PL and LP models, respectively, and β is the curvature parameter for the LP model.

Once all baseline model sources are configured, we perform a spectral fit of the flux normalization and spectral shape of the Galactic diffuse emission model, and all point sources with at least one predicted photon ($n_{\text{pred}} \geq 1$) from the catalog parameters. Next, we re-localize the sources inside the ROI with a distance of at least 0.1° from the ROI boundary to their local TS-peak (see Section 2.2) and refit their normalizations simultaneously. Finally, we refit the spectral parameters of all model components to complete the optimization of the baseline model.

The analysis then proceeds iteratively by looking for new candidate point sources. First, we investigate sources in the outer ROI defined by $R > R_{\text{inner}}$, where $R_{\text{inner}} = 1°$. Candidates are identified by creating a TS-map (see Section 2.5) for a test source with a PL spectral model with index $\Gamma = 2$. When generating the TS-map, the spectral parameters of all model sources are kept fixed, while the normalization of the test source is free to vary. Starting from the peak with the highest TS-value, we add candidate point sources with TS > 9 to the model, as long as the new candidate is at least 0.5° away from an existing candidate source with a higher TS-value. To ensure that the source is bright enough to detect the spectral curvature parameters in the LP case [40], we only model candidate sources with a LP spectral shape for sources with TS > 100, and otherwise they are modeled with a PL. When the candidate sources are added to the model, we simultaneously fit their spectral shapes and normalizations. Once all candidate sources fulfilling our criteria are added to the model, a new TS-map is generated and new candidate sources are added in the same way. This procedure continues until there are no candidate sources left located at $R > R_{\text{inner}}$ with TS > 9. Finally, we refit the normalizations and spectral shapes of all model components to complete the optimization of the outer ROI. The TS-maps of the ROI around FHES J1723.5-0501 before and after this source-finding process are shown in Figure 3.2.

In the final part of the analysis, we optimize the inner ROI by carefully looking for new point source candidates while we test the central source for extension. First, we add the central, potentially extended, source of interest to the model as a point source. Next, we search for new candidate point sources with TS > 9 located at $R < R_{\text{inner}}$ while simultaneously testing the central source for spatial extension (explained below). This optimization of the inner ROI proceeds in an iterative way, where iteration n describes the number of added point sources in the model starting from $n = 0$. The iteration steps are as follows:

1. We test the central source for extension with regard to the criteria described in the next paragraphs.

2. A TS-map is made, and if there are TS-peaks with TS > 9, we add a point source at the peak with the highest TS-value in R_{inner}, which now contains 4FGL catalog sources, the source of interest, and $n + 1$ additional point sources.

3. We re-localize all point sources in R_{inner} to their best-fit position, starting with the source of the highest TS-value.

4. These three steps are repeated until either an extended model with n added point sources in R_{inner} is preferred over a model with $n + 1$ point sources, there are no new candidate point sources with TS > 9, or the number of iterations exceeds five ($n = 5$).

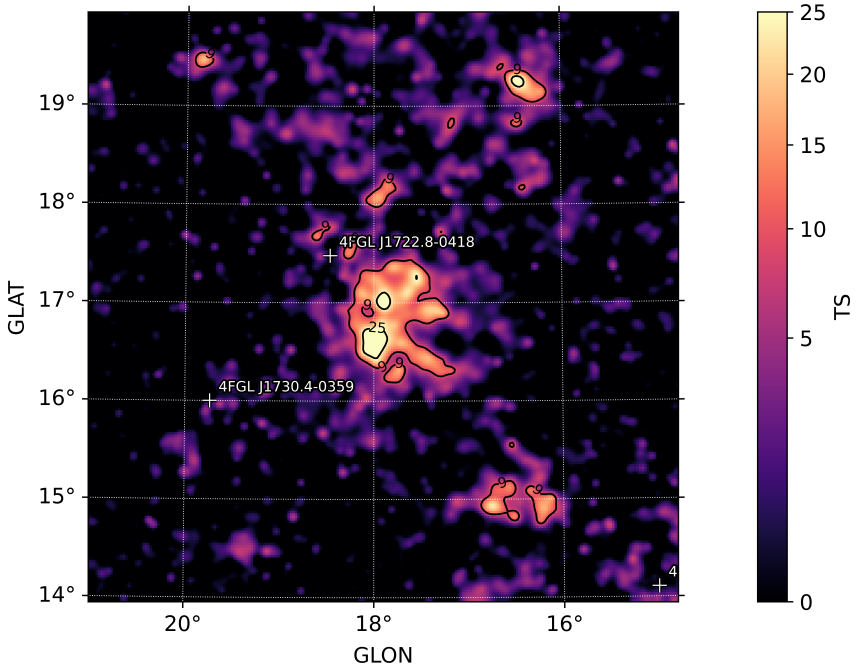

(a)

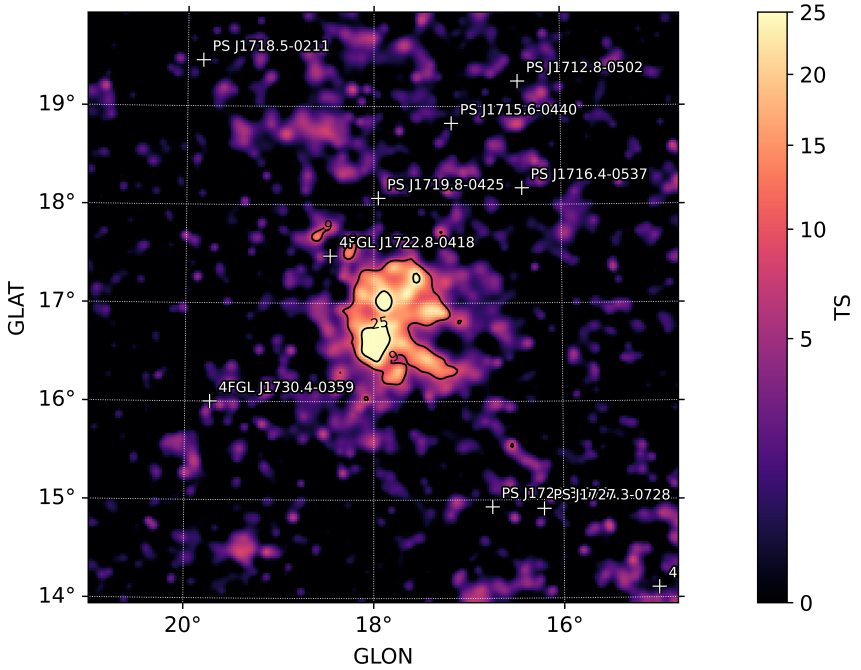

(b)

Figure 3.2: TS-maps of the ROI before (a) and after (b) the optimization of the outer ROI. In (a) we observe TS-peaks with TS > 9 at multiple positions in the ROI. The diffuse extended emission in the center is easy to identify and distinguish from the smaller surrounding point sources. The source finding algorithm identifies the peaks with $R > R_{\text{inner}}$ and TS > 9 and places a point source at their local maximum. In (b) we see that the peaks are replaced by point sources indicated by the white crosses labeled 'PS JXXXX.X-XXXX'. There are no remaining TS-peaks with TS > 9 at $R > R_{\text{inner}}$, and the outer ROI is optimized.

To classify the central source as extended, it needs to fulfill a number of criteria. In every iteration n, we compare the likelihood $\mathcal{L}_n$ of the model containing the central point source and n additional point sources in $R_{\rm inner}$ to the likelihood $\mathcal{L}_{\rm ext+n}$ of a model where the central source is imposed with an extended spatial template. When the central source is changed from a point source to an extended source, the spectral parameters are initially kept the same, thus keeping the PL spectral model. Then, we execute an extension fit of the source where we, among other things, find the best-fit position and extension radius for the potentially extended source. The angular size of the extension fit is denoted by $R_{\rm ext}$ and is parameterized by the intrinsic 68% containment radius. When fitting for extension, the sources within 1.5° of the central source are free to vary in their normalization, and for sources within 1.0°, we also free their spectral shapes. All other model source parameters are kept fixed.

After performing the extension fit, we need to investigate whether the source of interest actually is diffuse extended emission and not a cluster of point sources. The Aikaike Information Criterion (AIC) [48] is a useful tool to compare model fits with different numbers of parameters as it minimizes overfitting. The criterion is expressed as

$$\mathrm{AIC} = 2k - 2\ln\mathcal{L}, \tag{3.3}$$

where k is the number of independent adjusted parameters in the model, and $\mathcal{L}$ is the likelihood. The best model will minimize the AIC-value, thus penalizing models with a large number of parameters. The difference in AIC-values for the extended and point source models is expressed as

$$\Delta_{\rm ext} = \mathrm{AIC}_{\rm ext+n} - \mathrm{AIC}_n = 2(\ln\mathcal{L}_n - \ln\mathcal{L}_{\rm ext+n} + k_{\rm ext+n} - k_n), \tag{3.4}$$

where $\mathcal{L}_n$ and $\mathcal{L}_{\rm ext+n}$ are as defined above, and $k_{\rm ext+n}$ and k_n is the number of parameters in a model with and without an extended central source, respectively. If $\Delta_{\rm ext} < 0$ a model with an extended central source is preferred over a model with a central point source.

In some scenarios, the criterion given by Equation (3.4) prefers an extended model with n additional sources over a model with $n+1$ point sources, even though $n+1$ sources return a better fit. Thus, to gain confidence in the extended model we define

$$\mathrm{TS}_{\rm ext+1} = 2(\ln\mathcal{L}_{\rm ext+n+1} - \ln\mathcal{L}_{\rm ext+n}), \tag{3.5}$$

where $\mathcal{L}_{\rm ext+n+1}$ denotes the likelihood of a model including an extended central source and $n+1$ additional point sources. The value of $\mathrm{TS}_{\rm ext+1}$ describes the detection significance of an additional point source in the model with an extended central source. If this value is small (in this case $\mathrm{TS}_{\rm ext+1} < 16$), we consider the detection of a new candidate point source in the inner ROI to be insignificant.

The final source model is produced in the first iteration giving $\Delta_m < 0$ and $\mathrm{TS}_{\rm ext+1} < 16$, or no additional point sources with TS > 9 in $R_{\rm inner}$ are found in the source-finding algorithm. If there are not detected any new candidate point sources in the first iteration, both Δ_m and $\mathrm{TS}_{\rm ext+1}$ are undefined, which is the case for the ROI around FHES J1723.5-0501.

The detection significance of extended emission is quantified by

$$\mathrm{TS}_{\rm ext} = 2(\ln\mathcal{L}_{\rm ext+n} - \ln\mathcal{L}_n), \tag{3.6}$$

which is the likelihood ratio between a model with an extended central component and a model with a central point source. We classify the source as extended if $\mathrm{TS}_{\rm ext} > 16$, corresponding to a 4σ detection (our detection significance for FHES J1723.5-0501 is much higher, see Section 3.4 and Table 3.4). Once the central source is classified as extended, we update the source model with the extended template for the central source and refit the normalization and spectral shape of all model components. Finally, we consider the ROI to be fully optimized by running a new extension fit of the central source and once again refit all spectral parameters of the model components.

3.2 Fermi-LAT observations of FHES J1723.5-0501

Like any other Fermi-LAT analysis, we analyze FHES J1723.5-0501 using tools provided by the NASA Fermi-LAT collaboration. For this work, we use the `fermipy`[3] [49] Python package version

[3]See https://fermipy.readthedocs.io/en/latest/index.html

Table 3.1: Data selections and analysis configuration for the 2008 – 2016 data set.

Selection	Criterion
Observation period	August 4, 2008, to February 4, 2016
Mission Elapsed Time (MET)	239557417 to 476239414
Central coordinates	RA = 261.25°, DEC = −5.22°
Radius	8°
Energy range	1-1000 GeV
Zenith angle	$z \leq 100°$
Event types	`evtype` = 32 and `evtype` = 28
Event class	`evclass` = 128
Data quality cut	DATA_QUAL == 1
	LAT_CONFIG == 1

1.2 built on the Fermi *science tools* [50] version 2.2.0. The packages are publicly available[4]. The science tools contain the essential functions needed to perform the likelihood analysis, including the main tool `gtlike` which performs the spectral parameter fits. In this work, we use `gtlike` configured with the NEWMINUIT χ^2 minimization algorithm [38] to fit the parameters. The Python script used to perform the extended emission analysis of FHES J1723.5-0501 (and the point source analysis of PSR J1720-0533, see Chapter 4) is shown in Appendix A.1.

The extended source is analyzed for two different time intervals. First, we use the same 2008 – 2016 data set used by A18 (see Section 3.3). Once our results were consistent with those reported in their paper, the reproduced analysis is considered complete and we can confidently move on to analyze the full 14-year data set of the Fermi-LAT for this work (see Section 3.4).

3.3 Reproducing previous work: the 2008 – 2016 data set

FHES J1723.5-0501 is first analyzed using the same data set as A18, including data in the time range from August 4, 2008, to February 4, 2016, and within the energy range of 1 – 1000 GeV. We perform a joint likelihood analysis using `evtype` = 32 and `evtype` = 28, where `evtype` = 28 is the combined set of the last three quartiles of the PSF partition (see Section 2.4). These three event types are combined into one set to reduce the computational load, as done in A18. The overview of the data selection and analysis configuration for this reproduction analysis is shown in Table 3.1, and the `config.yaml` file used by `fermipy` is shown in Appendix A.2. To get as identical results as possible, the IRFs corresponding to the `P8R2_SOURCE_V6` class of events are used together with `gll_iem_v06.fits` and `iso_P8R2_SOURCE_V6_v06.txt` model files for the Galactic and isotropic background, respectively. These are the IRFs and background models used in A18 and are provided by the Fermi-LAT collaboration[5]. The data are centered around the position of 3FGL J1725.0-0513 and we include data within an 8° radius from this position. The 3FGL sources within a $10° \times 10°$ region around the central source are included in the initial baseline model, whereas the ROI is confined to only a $6° \times 6°$ region. The analysis follows the analytic steps explained in Section 3.1.

We are able to reproduce the result of A18 and find spectral parameters, spatial parameters, and fluxes that are fully consistent within the uncertainties. We find an extension radius of $R_{\rm ext} = 0.72° \pm 0.10°$, with a central position at Galactic coordinates $l = 17.93°$ and $b = 16.86°$. We get TS-values of TS = 103.2 and $\rm TS_{ext} = 84.7$, which are larger values than those reported in A18, especially for $\rm TS_{ext}$. This is suspected to originate from the last fitting procedures in the analysis, where we execute a double extension fit. This last step is unclear in A18, which is the reason for suspicion. Nevertheless, these TS-values show the significant detection of extension for this source with a source detection significance of $\sigma \simeq 10$, and extension detection significance of $\sigma \simeq 9$. For the spectral properties we obtain a γ-ray photon flux of $F_\gamma = (17.3 \pm 2.4) \times 10^{-10}$ cm^{-2} s^{-1}, a γ-ray energy flux of $G_\gamma = (2.2 \pm 0.4) \times 10^{-11}$ erg cm^{-2} s^{-1} and a PL spectral index of $\Gamma = 1.94 \pm 0.08$. The values of F_γ and Γ are fully consistent with the ones reported in A18 (the value of G_γ is not reported in A18). A comparison between the extension results from this work and A18 is shown

[4] See https://fermi.gsfc.nasa.gov/ssc/data/analysis/software/
[5] See https://fermi.gsfc.nasa.gov/ssc/data/access/lat/BackgroundModels.html

Table 3.2: Results from the extension fit of FHES J1723.5-0501 from A18 and the reproduced analysis with the 2008 − 2016 data set.

Analysis	l[°]	b[°]	TS	TS_{ext}	R_{ext}[°]	F_γ [a]	G_γ [b]	Γ
Ackermann et al. 2018	17.90	16.96	89.5	52.9	$0.73 \pm 0.10 \pm 0.01$	$18.3 \pm 2.5 \pm 2.1$	-	$1.97 \pm 0.08 \pm 0.06$
This work	17.93	16.86	103.2	84.7	0.72 ± 0.10	17.3 ± 2.4	2.2 ± 0.4	1.94 ± 0.08

[a] γ-ray photon flux in units of 10^{-10} cm^{-2} s^{-1} in the 0.1 − 100 GeV energy band.

[b] γ-ray energy flux in units of 10^{-11} erg cm^{-2} s^{-1} in the 0.1 − 100 GeV energy band.

Table 3.3: Data selections and analysis configuration for the 2008 − 2022 data set.

Selection	Criterion
Observation period	August 4, 2008, to September 26, 2022
Mission Elapsed Time (MET)	239557417 to 685859961
Central coordinates	$l = 17.90°$, $b = 16.96°$
Radius	8°
Energy range	1-1000 GeV
Zenith angle	$z \leq 100°$
Event types	`evtype` = 32 and `evtype` = 28
Event class	`evclass` = 128
Data quality cut	DATA_QUAL == 1
	LAT_CONFIG == 1

in Table 3.2.

In Figure 3.3 we present the TS-maps of FHES J1723.5-0501 after the ROI optimization of this analysis. The maps are produced using a test source with a PL spectral model with $\Gamma = 2$ while excluding FHES J1723.5-0501 from the source model. Figure 3.3a is produced to resemble Figure 11 from A18, and Figure 3.3b shows a zoomed TS-map of the extended source where the position of PSR J1720-0533 is indicated by the yellow circle. The map has similar TS-contours as the one produced in A18. We note that a few candidate sources (sources labeled 'PS JXXXX.X-XXXX') are added in this work, but not in A18, and vice versa. The reason for this can be small variations in the analysis procedure and configuration. As the obtained results are fully consistent, the minor differences in the faint nearby sources do not affect our results for FHES J1723.5-0501.

3.4 Full data analysis: the 2008 − 2022 data set

After we obtain consistent results with A18 for FHES J1723.5-0501 using the 2008 − 2016 data set, we redo the analysis with Fermi-LAT data from August 4, 2008, to September 26, 2022. The data are centered around the extended source's position in the FHES catalog, with $l = 17.90°$ and $b = 16.96°$, and we include data within an 8° radius of this position. The data are analyzed by applying a joint likelihood with the `P8R3_SOURCE_V3` class of events using `evtype` = 32 and `evtype` = 28 (see Section 2.4). The background emission is modeled using the `gll_iem_v07.fits` model file for the Galactic background and `iso_P8R3_SOURCE_V3_v1.txt` model file for the isotropic background. These models are the most up-to-date background models provided by the Fermi-LAT collaboration[6]. As in the previous analysis, we include catalog sources within a $10° \times 10°$ region around the central position, now using the 4FGL-DR3 catalog [40], and we confine the ROI to a $6° \times 6°$ region. The further data selection and analysis configurations are displayed in Table 3.3, and the `config.yaml` file used by `fermipy` is shown in Appendix A.3. The analysis follows the procedure explained in Section 3.1 with one exception: all spectral parameters of 4FGL catalog sources outside the $6° \times 6°$ ROI are kept fixed to their catalog values throughout the analysis. This is to reduce the number of free parameters in the χ^2 minimization fit.

With six more years of Fermi-LAT data, we find a 30% increase in the TS-value of FHES J1723.5-0501, now with TS = 133.8, corresponding to a $\sigma = 11.6$ detection. We also find an increase

[6] See https://fermi.gsfc.nasa.gov/ssc/data/access/lat/BackgroundModels.html

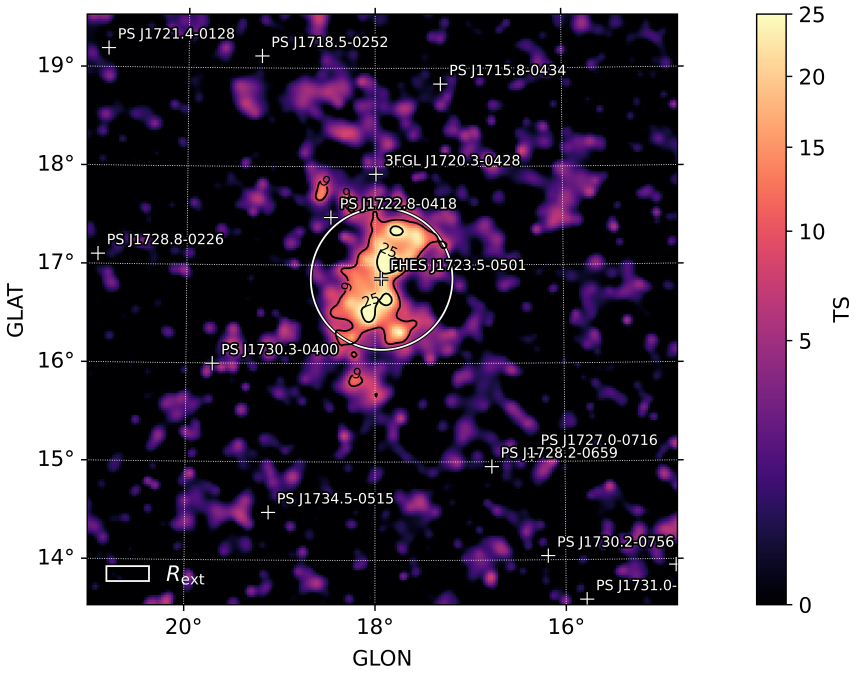

(a)

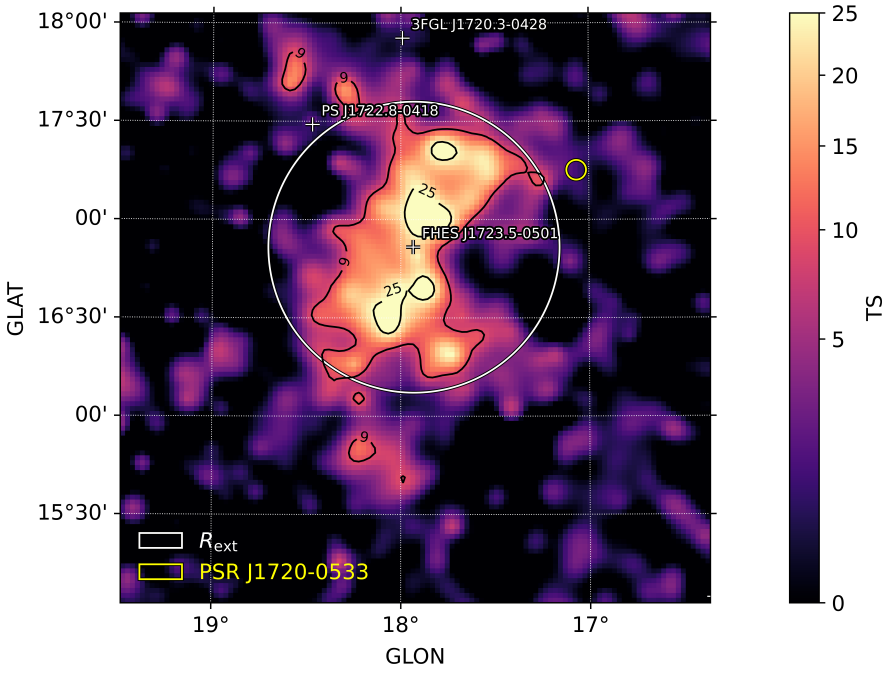

(b)

Figure 3.3: Top (a): TS-map of FHES J1723.5-0501 for the A18 reproduction analysis. White crosses indicate the model sources, where sources labeled 'PS JXXXX.X-XXXX' are candidate sources added in the ROI optimizing algorithm. The white circle indicates $R_{\rm ext}$ centered at the best-fit position. This figure is similar to Figure 11 (left) in A18. Bottom (b): An enlarged plot of the same TS-map with the position of PSR J1720-0533 marked by the yellow circle indicating the 3' uncertainty of FAST.

Table 3.4: The results from the extension fit of FHES J1723.5-0501 from Araya et al. 2021 [43], compared to the results of the full 2008 − 2022 data set analysis of this work.

Analysis	$l[^\circ]$	$b[^\circ]$	TS	TS_{ext}	$R_{ext}[^\circ]$	F_γ [a]	G_γ [b]	Γ
Araya et al 2021	-	-	153.2	65.6	$0.68^{+0.07}_{-0.16}$	-	~ 1	$1.83 \pm 0.02 \pm 0.05$
This work	17.84	16.82	133.8	114.7	$0.74^{+0.10}_{-0.08}$	16.2 ± 2.0	2.1 ± 0.3	1.93 ± 0.07

[a] γ-ray photon flux in units of $10^{-10}\,\mathrm{cm}^{-2}\,\mathrm{s}^{-1}$ in the $0.1 - 100\,\mathrm{GeV}$ energy band.

[b] γ-ray energy flux in units of $10^{-11}\,\mathrm{erg}\,\mathrm{cm}^{-2}\,\mathrm{s}^{-1}$ in the $0.1 - 100\,\mathrm{GeV}$ energy band.

in the extension detection significance, now with $TS_{ext} = 114.7$, corresponding to a $\sigma = 10.7$ detection. The extension fit return a best-fit position of $l = 17.84^\circ$ and $b = 16.82^\circ$, with the extension radius of $R_{ext} = 0.74^{\circ\,+0.10^\circ}_{-0.08^\circ}$. The final TS-maps of the ROI, created using a test source with a PL spectral model with $\Gamma = 2$ and excluding FHES J1723.5-0501 from the source model, are shown in Figure 3.4. We find a γ-ray photon flux of $F_\gamma = (16.2 \pm 2.0) \times 10^{-10}\,\mathrm{cm}^{-2}\,\mathrm{s}^{-1}$, a γ-ray energy flux of $G_\gamma = (2.1 \pm 0.3) \times 10^{-11}\,\mathrm{erg}\,\mathrm{cm}^{-2}\,\mathrm{s}^{-1}$, and a PL spectral index of $\Gamma = 1.93 \pm 0.07$. These values are fully consistent with the results from A18, and our reproduced analysis (see Section 3.3).

We show the spectral energy distribution (SED) using two energy bins per decade for FHES J1723.5-0501 in Figure 3.5. We detect the source up to the highest energy band ($\sim 300-1000\,\mathrm{GeV}$), highlighting its measured 'hardness'. We also test FHES J1723.5-0501 for spectral curvature by defining $TS_{LP} \equiv -2(\ln\mathcal{L}_{PL} - \ln\mathcal{L}_{LP})$, where $\mathcal{L}_{PL}$ and $\mathcal{L}_{LP}$ are the likelihoods of the model where the extended source is modeled with a PL and LP, respectively. We obtain, $TS_{LP} \simeq 0$, and thus a LP is not preferred over a PL spectral model for FHES J1723.5-0501.

We compare our findings with those reported in the paper by Araya et al. 2021 [43], where the authors conducted an independent analysis on FHES J1723.5-0501 with a data set from August 2008 to July 2021. In contrast to this work, they use data in the $0.5 - 500\,\mathrm{GeV}$ energy range, in a non-joint likelihood analysis using `evtype` = 3, as well as a different ROI optimization procedure. Table 3.4 shows the comparison between their results and the results from this work on FHES J1723.5-0501 with the full 14-year data set. They report a γ-ray luminosity of $L_\gamma \sim 9 \times 10^{33}\,\mathrm{erg}\,\mathrm{s}^{-1}$ at an arbitrary distance of 3 kpc, resulting in $G_\gamma \sim 1 \times 10^{-11}\,\mathrm{erg}\,\mathrm{cm}^{-2}\,\mathrm{s}^{-1}$. While the results for R_{ext} and Γ coincide within the uncertainties, we suspect their lower value for Γ to be a result of their upper energy range cut of 500 GeV, producing a model fit with a slightly harder spectrum for FHES J1723.5-0501. They obtain a larger TS-value compared to this work, but their TS_{ext} value is only 57% of ours. We suspect our large TS_{ext} value to originate from the use of a joint likelihood analysis with the PSF partition (See Section 2.4).

3.4.1 Lightcurve

We create a lightcurve for FHES J1723.5-0501 (shown in Figure 3.6) by dividing the data set into 14 equal time bins, corresponding to about one year of Fermi-LAT data in each bin. A local livetime cube (see Section 2.4) is calculated in each bin, however, we receive an error when producing the livetime cube for the first time bin. In the second time bin, the calculated photon flux gives a large anomaly compared to the mean value and the data point has large uncertainties. Therefore, the first two data points are not included in the plot in Figure 3.6. The lightcurve shows little variability around the average $F_\gamma = 16.2 \times 10^{-10}\ \mathrm{cm}^{-2}\,\mathrm{s}^{-1}$ line (indicated by the dashed line in the figure) and we find no significant change in flux over the 12-year time span.

3.4.2 Morphology

The TS-maps of FHES J1723.5-0501, from the final optimized model, are shown in Figure 3.4. We find that the TS-map has a more circular shape compared to Figure 11 in A18. Furthermore, as mentioned above, the TS-values have increased as a result of more data, with some regions exceeding TS = 49. From Figure 3.4b we observe that the extension radius R_{ext} with its 1σ uncertainty overlaps the $\sim 3'$ uncertainty of PSR J1720-0533's radio timing position, empathizing

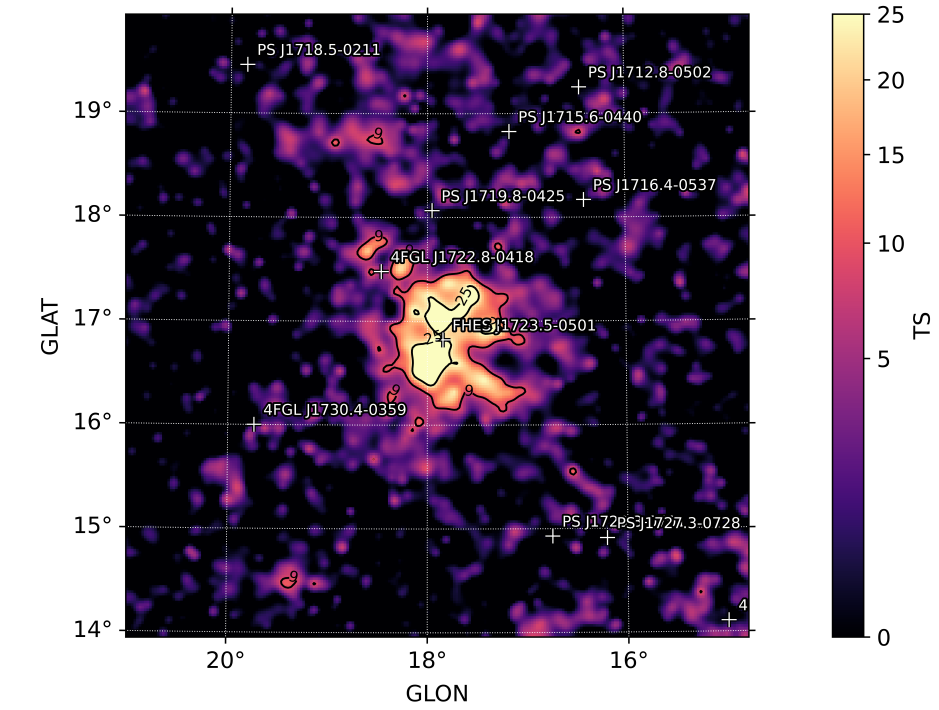

(a)

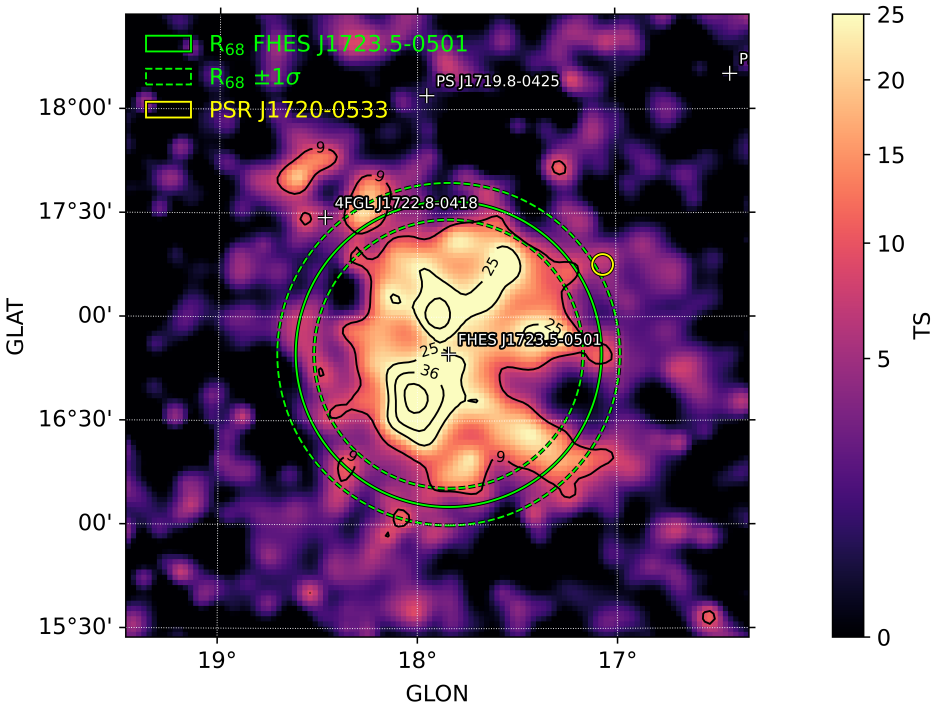

(b)

Figure 3.4: Top (a): Final TS-map of FHES J1723.5-0501 in the full 2008 – 2022 data analysis. White crosses indicate the positions of the model sources. Bottom (b): Zoomed TS-map of the extended source where the position of PSR J1720-0533 is marked with a yellow circle indicating the 3′ uncertainty of FAST. The green circles indicate the measured $R_{\rm ext}$-value with $\pm1\sigma$ uncertainties.

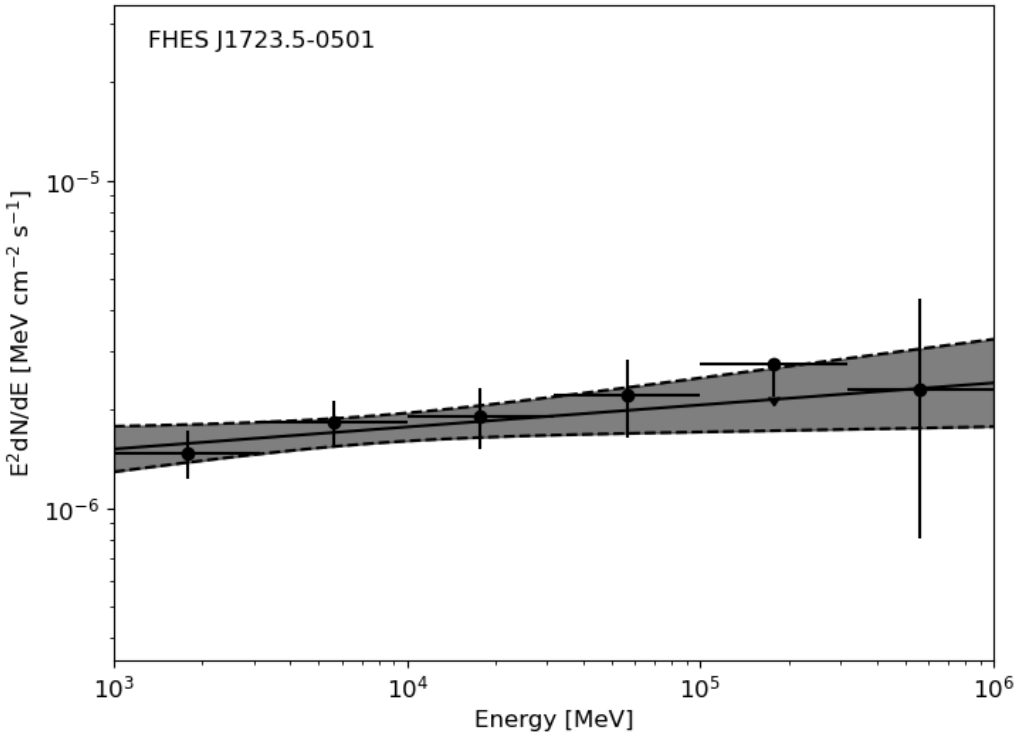

Figure 3.5: SED for FHES J1723.5-0501 in the analysis energy range. The points indicate the measured $E^2\mathrm{d}N/\mathrm{d}E$ values, with associated uncertainties. The arrow shows an upper limit, and the shaded area indicates the model spectrum with $\pm 1\sigma$ uncertainties.

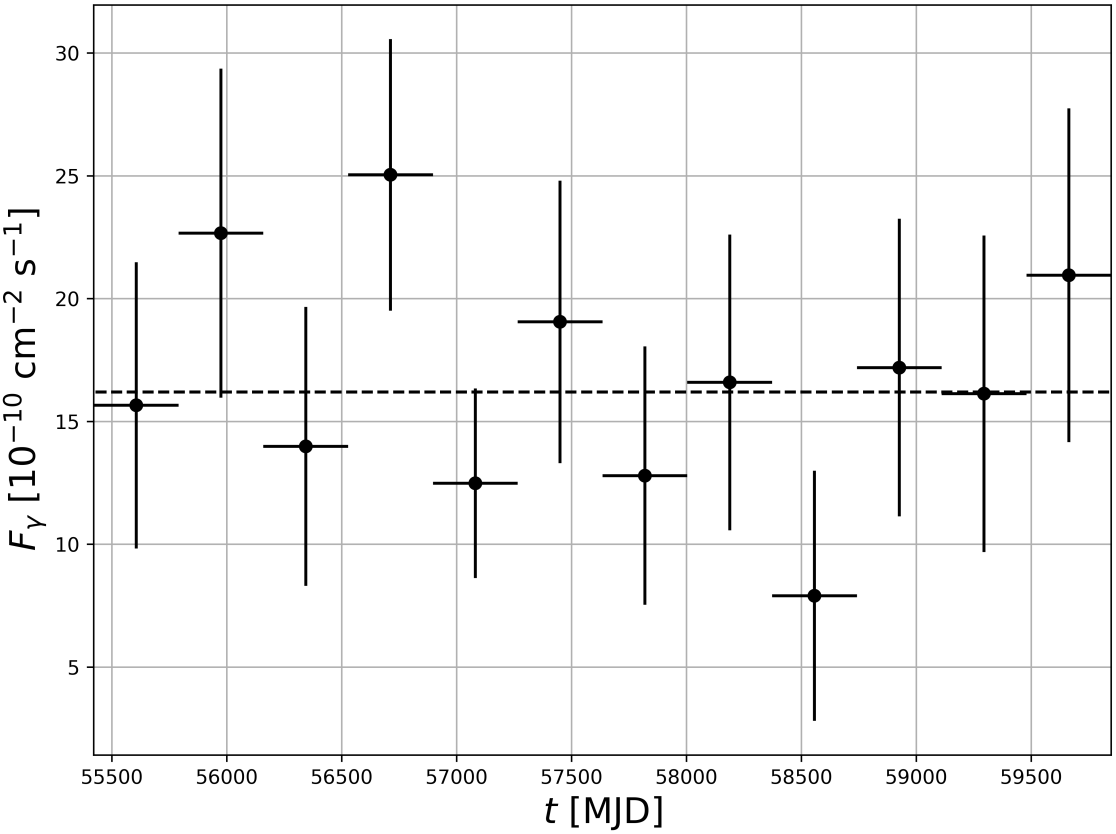

Figure 3.6: Lightcurve of FHES J1723.5-0501 between 2010-2022, produced using the optimized ROI model and the baseline analysis configurations. The dashed line indicates the average photon flux, $F_\gamma = 16.2 \times 10^{-10}\,\mathrm{cm}^{-2}\,\mathrm{s}^{-1}$. We observe no evident variability in the photon flux in the Fermi-LAT data.

Table 3.5: Morphological comparison between a 2D radial Gaussian and a radial disk as the extended spatial template for FHES J1723.5-0501 for source models with and without including 4FGL J1722.8-0418.

Model	$l[^\circ]$	$b[^\circ]$	$R_{\rm ext}[^\circ]$	TS	$\rm TS_{ext}$	ΔAIC
Disk	18.13 ± 0.05	17.00 ± 0.05	$0.72^{+0.02}_{-0.02}$	259.4	224.8	169.5
Gaussian	18.13 ± 0.05	17.18 ± 0.06	$0.78^{+0.08}_{-0.06}$	275.0	222.5	153.8
Disk*	17.82 ± 0.06	16.77 ± 0.08	$0.60^{+0.07}_{-0.03}$	132.8	103.7	12.4
Gaussian*	17.84 ± 0.07	16.82 ± 0.08	$0.74^{+0.10}_{-0.08}$	133.8	114.7	0

*Model including 4FGL J1722.8-0418.

Table 3.6: Summary of the energy-dependent morphology analysis of FHES J1723.5-0501.

Energy band [GeV]	$R_{\rm ext}[^\circ]$	$\rm TS_{ext}$
1-4	0.86 ± 0.10	152
4-10	0.58 ± 0.08	88
10-1000	0.83 ± 0.12	123

the importance of proper modeling of the extended source to obtain accurate constraints on the γ-ray emission of the pulsar.

To investigate the morphology of FHES J1723.5-0501, we run tests with different extended templates, namely the 2D Gaussian and the radial disk templates. In addition, we test the source model with and without 4FGL J1722.8-0418 for both templates. This 4FGL catalog source also lies close to the extended emission of FHES J1723.5-0501, as can be seen in Figure 3.4b, and should therefore be modeled and tested carefully to avoid any bias. We find that the model with a 2D Gaussian template for the central source and including 4FGL J1722.8-0418 gives the best fit according to the AIC-values (see Section 3.1). Table 3.5 show the difference in AIC-values for the distinct models compared to the best-fit model (Gaussian*), together with the best-fit localization coordinates, and calculated TS- and $R_{\rm ext}$-values.

We also study the energy-dependent morphology by examining the extension of FHES J1723.5-0501 in three different energy bands ($1-4\,\rm GeV$, $4-10\,\rm GeV$ and $10-1000\,\rm GeV$). These energy ranges were chosen to achieve a reasonable amount of counts in each energy band, where we find $n \simeq 500$ for the lowest energy band, $n \simeq 200$ for the middle energy band, and $n \simeq 100$ for the highest energy band. We obtain $R_{\rm ext}(1-4\,\rm GeV) = 0.86^\circ \pm 0.10^\circ$ with $\rm TS_{ext} = 152$ in the lowest energy band, $R_{\rm ext}(4-10\,\rm GeV) = 0.58^\circ \pm 0.08^\circ$ with $\rm TS_{ext} = 88$ in the middle energy band, and $R_{\rm ext}(10-1000\,\rm GeV) = 0.83^\circ \pm 0.12^\circ$ with $\rm TS_{ext} = 123$ in the highest energy band. The summary of the results is presented in Table 3.6. In Figure 3.7 we show TS-maps of FHES J1723.5-0501, produced with a PL test source with $\Gamma = 2$, when confining the data to the respective energy bands. We observe that the radiation is mostly centered around the central position of FHES J1723.5-0501 for all energy bands. The lowest energy band shows two eminent regions of radiation, one in the north and one in the south (see Figure 3.7a). None of these regions exceeds $\rm TS \geq 16$. However, we observe that the regions with $\rm TS > 9$ are relatively large in this band. We reason this with the broader PSF in the lower energy ranges of the Fermi-LAT which makes it more difficult to accurately place the emission in the lowest energy band. The scale factor, $S_p(E)$, which indicates the first order variation of the PSF with energy[7], gives $S_P(2\,\rm GeV) \simeq 0.005$ for the central energy in the lowest energy band. This scale factor is reduced by almost a factor of three in the middle band, where we find one noticeable region of emission in the southwest region with $\rm TS \geq 25$ and $3-4$ smaller regions of $\rm TS \geq 9$ (see Figure 3.7b). In the highest energy band, the emissions are spread out in multiple smaller regions, with one region exceeding $\rm TS \geq 16$ close to the central position of FHES J1723.5-0501 (see Figure 3.7c).

Going from the lowest to the middle energy band shows a decrease in the calculated $R_{\rm ext}$ value, suggesting a decrease in extension with increasing energies. However, the decrease is not statistically significant ($\simeq 2\sigma$), and the calculated $R_{\rm ext}$ value for the $10-1000\,\rm GeV$ band suggests an extension similar to that of the $1-4\,\rm GeV$ band, indicating a nearly constant $R_{\rm ext}$ over these two

[7]See https://fermi.gsfc.nasa.gov/ssc/data/analysis/documentation/Cicerone/Cicerone_LAT_IRFs/IRF_PSF.html

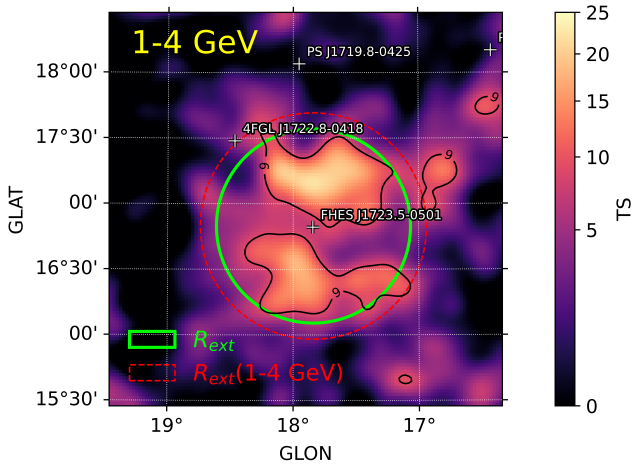

(a)

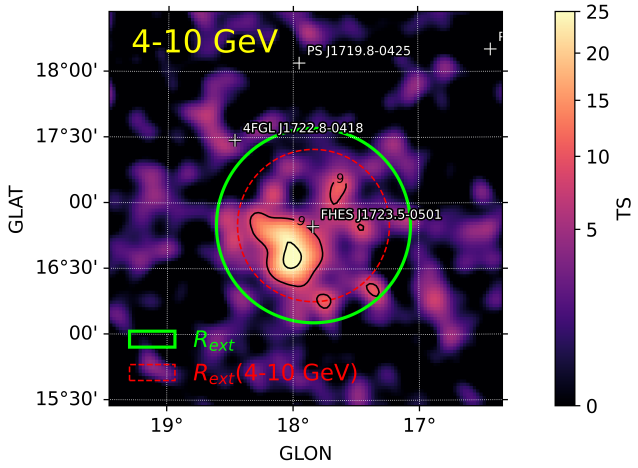

(b)

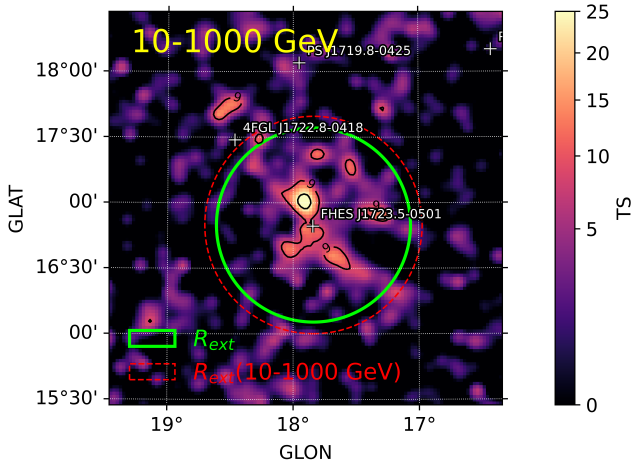

(c)

Figure 3.7: TS-maps of FHES J1723.5-0501 in different energy bands. The green circles indicate $R_{\text{ext}} = 0.74^{\circ}$ for the full energy range, the red dashed circle indicates R_{ext} for the given energy range, and the model sources are indicated by the white crosses.

energy bands. Despite this, an inspection of the TS-map in Figure 3.7c reveals that the calculated value of $R_{\rm ext}$ may be unrealistic, given that the majority of the high-energy emission is located inside the green circle. We observe that the small TS-peak just east of 4FGL J1772.8-0418 is included in the extension fit, and we interpret this as a possible overshoot of the fit. If this TS peak is a part of the extended emission or whether it could be from background sources excluded in the model, is not clear. Figure 3.4b might suggest that it does not originate from FHES J1723.5-0501, as it is located outside $R_{\rm ext}$. However, it is located partly inside the 1σ uncertainty, making it difficult to place the origin of this TS-peak. An overshoot in the extension fit could result in a larger calculated $R_{\rm ext}$ value for the $10-1000\,\mathrm{GeV}$ energy band than expected from inspection of the TS-map in Figure 3.7c, and that the real value of $R_{\rm ext}$ is smaller in this energy band. If this is the case, there is evidence of a decrease in $R_{\rm ext}$ with increasing energy, as both the middle and highest energy bands would show a decrease in $R_{\rm ext}$.

A decrease in $R_{\rm ext}$ with increasing energy suggests a particle energy loss with increasing distance from the center of the extension. This is characteristic of a PWN, as the e^+ e^- pairs are expected to cool down as they propagate outwards from a central pulsar [51]. Motivated by the discussion above, we look for a central point-like source in the center of FHES J1723.5-0501 which we could identify as a central pulsar, suggesting that this extended source is a PWN. However, there is no significant evidence for such a candidate point source in the optimization of the inner ROI (see Section 3.1). Thus we report no evidence from this γ-ray analysis that FHES J1723.5-0501 is a PWN considering no detection of a point-like central source engulfed in the extended emission, and no clear evidence of a decreasing value of $R_{\rm ext}$ with increasing energies.

3.5 Possible physical connection with PSR J1720-0533

At the time of A18's publication, PSR J1720-0533 was not yet discovered, and it was not considered by Araya et al. 2021 [43] as they published their work a few weeks after the discovery paper from Wang et al. 2021 [32]. Hence, we revisit the potential of a physical connection between FHES J1723.5-0501 and the black widow pulsar. On the timescales of the characteristic age of PSR J1720-0533 ($\tau \sim 1\,\mathrm{Gyr}$, see Equation (1.4)), SNRs cool down and disappear. Therefore we do not consider the SNR scenario where the pulsar has propagated away from the extended emission. Instead, since a large portion of the observed Galactic γ-rays originate from interstellar dust clouds [45], we consider the possibility of cosmic rays ejected away from the black widow system interacting with the interstellar medium to produce the observed γ-ray emission of FHES J1723.5-0501. These γ-ray photons could be produced in hadronic interactions between the cosmic rays and an interstellar dust cloud, or by re-accelerating leptons in the magnetic fields within the cloud. Below we take a look at the energy budget between PSR J1720-0533 and FHES J1723.5-0501, and investigate the possibilities of these scenarios.

3.5.1 Energy budget between PSR J1720-0533 and FHES J1723.5-0501

Assuming a distance to FHES J1723.5-0501 similar to that of PSR J1720-0533, with a dispersion measure distance of $d \sim 0.2\,\mathrm{kpc}$, and an angular radius of $R_{\rm ext} = 0.74^\circ \approx 0.013\,\mathrm{rad}$ for the extended source, we calculate a spatial diameter of $D_{\rm ext} = 2R_{\rm ext}d \simeq 5\,\mathrm{pc}$. With this distance we get a γ-ray luminosity of $L_\gamma \simeq 1\times10^{32}\,\mathrm{erg\,s^{-1}}$ for FHES J1723.5-0501. Additionally, we calculate the angular separation between the central coordinates of FHES J1723.5-0501 and PSR J1720-0533 to be $\theta_s = 0.85^\circ \approx 0.015\,\mathrm{rad}$. Using the reported spin-down power of PSR J1720-0533 from Wang et al. 2021 [32] of $\dot{E} = 0.85\times10^{34}\,\mathrm{erg\,s^{-1}}$, and assuming isotropic emission from the black widow pulsar, we find

$$L = \frac{\dot{E}}{4\pi s^2}\times\pi\left(\frac{D_{\rm ext}}{2}\right)^2 \simeq 1.5\times10^{33}\,\mathrm{erg\,s^{-1}},$$

which is the total received energy per second by FHES J1723.5-0501 from PSR J1720-0533, assuming a distance of $s = d\theta_s = 3\,\mathrm{pc}$ between the two sources. Therefore, with the simplified assumptions mentioned above, the pulsar is theoretically energetic enough to power the γ-ray emission from FHES J1723.5-0501, with a resulting γ-ray efficiency of $\eta \simeq 7\%$ for the extended source.

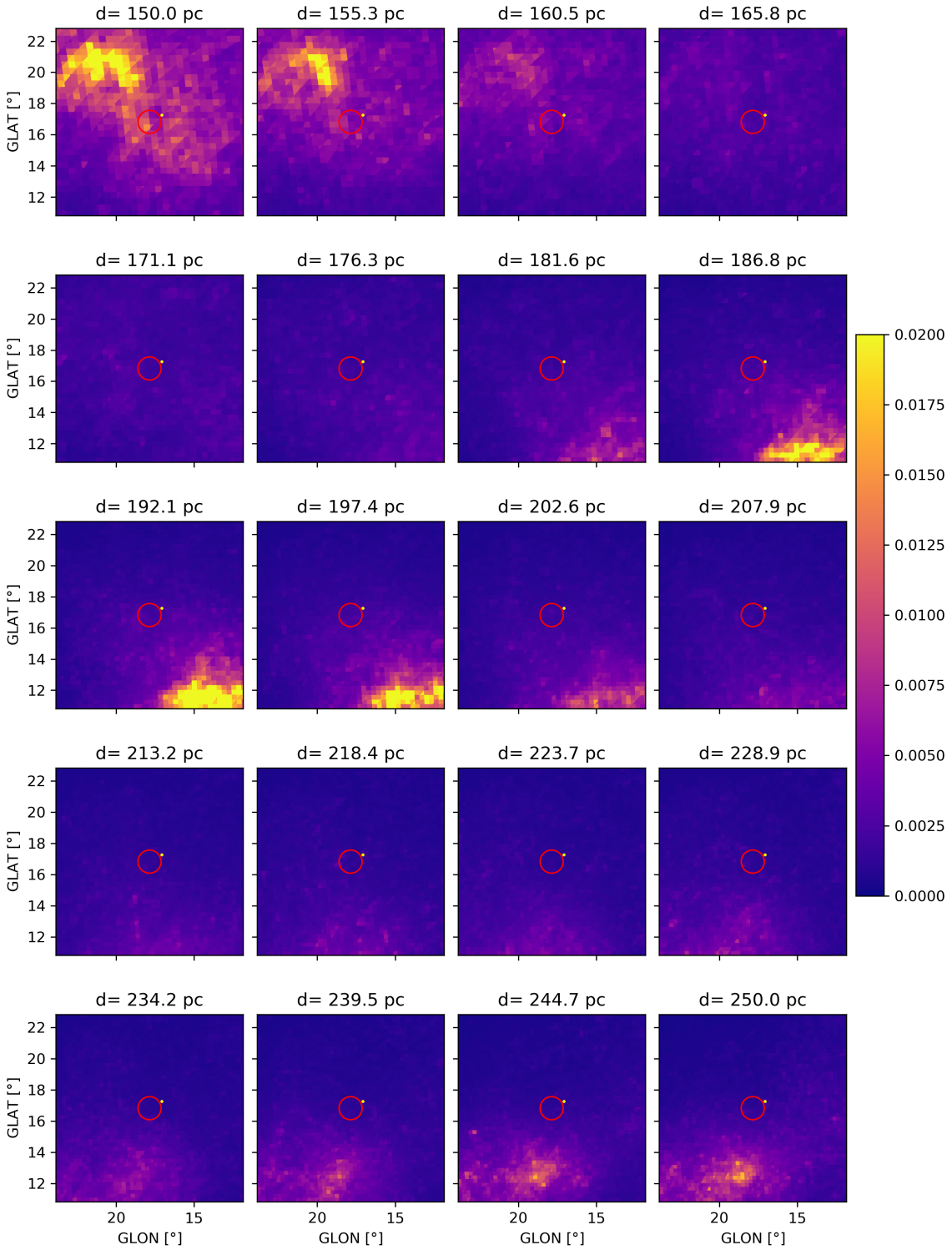

Figure 3.8: Dust maps in different slices along the line of sight around FHES J1723.5-0501. The color scale shows the extinction factor of a G-band photon traveling one parsec in that dust. The values are given in natural logarithmic units. The positions of FHES J1723.5-0501 and PSR J1720-0533 are indicated by the red and yellow circles, respectively. The maps are created using the data products from Leike et al. 2020 [45] in the `dustmaps` Python package.

3.5.2 The Hillas criterion

In the leptonic case, we investigate whether FHES J1723.5-0501 is theoretically large enough to re-accelerate leptonic particles arriving from PSR J1720-0533 to the observed energies by the Fermi-LAT. The Hillas criterion [44], given by

$$\epsilon < ZeBR, \tag{3.7}$$

limits the Larmor radius of a particle to the radius of the accelerator. Here Z is the atomic number of the particle, e is the electron charge, B is the magnetic field strength of the accelerator and R is the radius of the accelerator. For an electron or positron, the Larmor radius is given by $R_L = 1.08\epsilon_{15}B_{\mu\mathrm{G}}^{-1}$ pc, where ϵ_{15} is the energy of the particle in units of 10^{15} eV and $B_{\mu\mathrm{G}}$ is the magnetic field strength of the accelerator in units of microgauss.

Based on the detection of photons with $\epsilon \sim 500\,\mathrm{GeV}$ from the SED of FHES J1723.5-0501 (see Figure 3.5), and assuming a magnetic field strength in the galactic medium on the scale of $B \sim 1\,\mu\mathrm{G}$ (see e.g. [52]), we calculate the Larmor radius, R_L, of the e^+ e^- pairs of with this energy to be on the scale $R_L \sim 1 \times 10^{-3}\,\mathrm{pc}$ which is much less than the estimated radius of the extended source of $D_{\mathrm{ext}}/2 = 2.5\,\mathrm{pc}$ if it was placed at $d \simeq 0.2\,\mathrm{kpc}$. Therefore, with these assumptions, we expect the extended source to be theoretically large enough to re-accelerate e^+ e^- pairs to the observed energies. By using Equation (3.7), we get the maximum energy of an electron or positron in an accelerator with radius $D_{\mathrm{ext}}/2$ and magnetic field strength of $B = 1\,\mu\mathrm{G}$ of $\epsilon_{\mathrm{max}} \sim 3700\,\mathrm{erg} = 2310\,\mathrm{TeV}$, which exceeds the sensitivity range of the Fermi-LAT.

These calculations imply that FHES J1723.5-0501, in fact, could be energized by the pulsar emission if it was placed at a similar distance from Earth, and if there exist internal magnetic fields within the extended source to accelerate leptons arriving from the pulsar.

3.5.3 Dust maps

Motivated by the discussion above, we conduct a search for a potential dust cloud along the line of sight of FHES J1723.5-0501 by using the dust map created by Leike et al. 2020 [45] in the `dustmaps` Python package[8]. The map consists of a data cube representing the extinction of G-band (optical) photons per parsec in a chosen ROI at a given distance away from Earth. Figure 3.8 illustrates different slices of extinction along the line of sight around FHES J1723.5-0501, indicated by the red circle, as well as the position of PSR J1720-0533 indicated by the small yellow circle. We consider distances in the range $150 - 250\,\mathrm{pc}$, as the cosmic ray flux from PSR J1720-0533 would not be large enough to energize the extended source if it was located beyond this range. The color scale indicates the extinction in natural logarithmic units, where a value of 1 would correspond to an extinction of e^{-1} per parsec for the G-band photon. If the extended γ-ray source originates from a high-density region within the interstellar medium, we would expect a noticeable increase in the extinction fraction in the region encompassed by the red circle. However, our analysis of the produced dust maps reveals no evidence for a region of higher extinction in the produced dust maps in the vicinity of FHES J1723.5-0501. Therefore, we conclude that there is no indication of a dust cloud along the $150 - 250\,\mathrm{pc}$ line of sight region surrounding FHES J1723.5-0501.

3.6 Conclusions

We conclude that it is unlikely that FHES J1723.5-0501 is a dust cloud responsible for producing γ-ray photons through interactions with cosmic rays originating from PSR J1720-0533. Despite the Hillas criterion being satisfied for a $D_{\mathrm{ext}} \sim 5\,\mathrm{pc}$ spherical cloud, there is no evidence supporting the existence of such an interstellar magnetized cloud in the region around FHES J1723.5-0501, as seen in Figure 3.8. Fluctuations in the Galactic magnetic fields are often attributed to dust clouds [45], and therefore we see no compelling reason why there should exist a magnetized region in the interstellar medium responsible for accelerating leptons arriving from PSR J1720-0533. Additionally, the hadronic scenario, where the cosmic rays from the black widow potentially produce the extended γ-ray emission, also fails with the lack of evidence of a dust cloud in the vicinity of FHES J1723.5-0501.

[8] See https://dustmaps.readthedocs.io/en/latest/index.html

If the calculated $R_{\rm ext}$ in the $10 - 1000\,{\rm GeV}$ energy band is accurate, it supports the claim from Araya et al. 2021 [43] that FHES J1723.5-0501 is a type 1a SNR, as our morphological analysis suggests a non-decreasing $R_{\rm ext}$ with increasing energies. Additionally, the evidence of a 1.4 GHz radio shell engulfed by the extension reported by A18, contributes to their suggestion that FHES J1723.5-0501 is associated with a type 1a SNR. In their analysis of this radio emission, Araya et al. 2021 [43] calculate a two-point spectral index from the 1.4 and 2.3 GHz radio flux densities of $\alpha = -0.75 \pm 0.15$ for $S \propto \nu^{\alpha}$, and conclude that this is consistent with non-thermal emission from a synchrotron-emitting shell SNR. Ultimately, it seems unlikely that there exists a physical connection between PSR J1720-0533 and FHES J1723.5-0501, and there is no evidence to contradict the statement of a type 1a SNR nature for FHES J1723.5-0501.

Based on our observed γ-ray energy flux in the $0.1 - 100\,{\rm GeV}$ energy band of $G_{\gamma} = 2.1 \times 10^{-11}\,{\rm erg\,cm^{-2}\,s^{-1}}$, and the distance estimate range of $d \simeq 1.4 - 3.5\,{\rm kpc}$ from Araya et al. 2021 [43], we calculate the γ-ray luminosity of FHES J1723.5-0501 to be in the range of $L_{\gamma} = 5 \times 10^{33} - 3 \times 10^{34}\,{\rm erg\,s^{-1}}$ which places it among the brightest SNR γ-ray luminosities observed, as can be seen in Figure 13 in the First Fermi-LAT Supernova Remnant Catalog (1SC) [53]. The calculated spectral index of $\Gamma = 1.93 \pm 0.07$ places this potential γ-ray emitting SNR among the SNRs with the hardest reported spectral indices (see Figure 8 in 1SC).

Chapter 4

Fermi-LAT γ-ray Analysis of PSR J1720-0533

4.1 Flux upper limits on PSR J1720-0533: the faintest γ-ray pulsar

After properly modeling FHES J1723.5-0501 (see Chapter 3), we search for a point-like γ-ray counterpart to the black widow spider PSR J1720-0533 (see Section 1.6). To do so, we introduce a new point source at the radio timing position of the black widow pulsar, measured by Wang et al. 2021 [32]. We model its γ-ray spectrum with a power law with an exponential cutoff (PLEC), given by

$$\frac{dN}{dE} = N_0 \left(\frac{E}{E_c}\right)^{\Gamma} \exp\left(\frac{E}{E_c}\right)^{b}, \tag{4.1}$$

where E_c is the cutoff energy. This spectral shape gives a common way to model the spectral curvature of MSPs [33], which typically display a cutoff at a few GeV. As the spectral parameters of PSR J1720-0533 are unknown, we use the reported best-fit values from Xing and Wang 2016 [54]. The authors perform a maximum likelihood analysis of 39 MSPs in the Second Fermi-LAT Catalog for γ-ray pulsars (2PC) [33], to obtain flux data points in the $0.1 - 300$ GeV energy band. Then, they fit a PLEC to the normalized flux data points of these sources and derive best-fit values of $E_c = 3.7^{+0.95}_{-0.70}$ GeV and $\Gamma = 1.54^{+0.10}_{-0.11}$, which they state can be used to identify candidate MSPs among the unidentified Fermi-LAT sources. We assume these values give a good representation of the γ-ray spectrum of PSR J1720-0533. We also set b to one, as there is no evidence to suggest a sub-exponential cutoff for this pulsar, given by $b < 1$. These parameters are kept fixed in the analysis as the source is too faint for the Fermi-LAT to detect it. After adding the black widow to the model, we refit its normalization together with all spectral parameters of all other model sources in the ROI.

From this final fit, we find TS = 2.8 for PSR J1720-0533, resulting in a detection significance of 1.7σ and thus a non-detection of the pulsar. Figure 4.1 presents the local TS-map around the pulsar using a test source with a PLEC spectral model with $\Gamma = 1.54$ and $E_c = 3.7$ GeV, and the map shows no significant peaks in the vicinity of the pulsar radio timing position. For the TS-peak around 0.3° east of the pulsar position, we find a maximum TS-value of TS = 5.6 ($\sigma \approx 2.4$), which is not a significant detection either.

For the spectral properties assumed above, we find a 95% upper limit on the γ-ray energy flux in the $0.1 - 100$ GeV band of $G_\gamma < 1.3 \times 10^{-12}$ erg cm^{-2} s^{-1}. Assuming isotropy, and the distance estimate of $d = 191$ pc, we find a 95% upper limit on the γ-ray luminosity in the $0.1 - 100$ GeV band of $L_\gamma < 5.8 \times 10^{30}$ erg s^{-1}. At the time of writing, this is the deepest L_γ upper limit for any pulsar. This statement remains true considering a conservative 50% uncertainty on the dispersion measure distance of ± 96 pc. We demonstrate this in Figure 4.2 where we plot the γ-ray luminosities against the spin-down power ($\dot{E}$) of the currently known spiders and other types of pulsars (see captions to Figure 4.2 and Table 4.1 for details). We include three lines of constant γ-ray efficiency $\eta = L_\gamma/\dot{E}$ and the heuristic luminosity defined by $L_\gamma^h = \sqrt{10^{33}\dot{E}}$ erg s^{-1}. This heuristic luminosity arises from the assumption that above some open field-line voltage, $V \propto \sqrt{\dot{E}}$, the γ-ray luminosity is

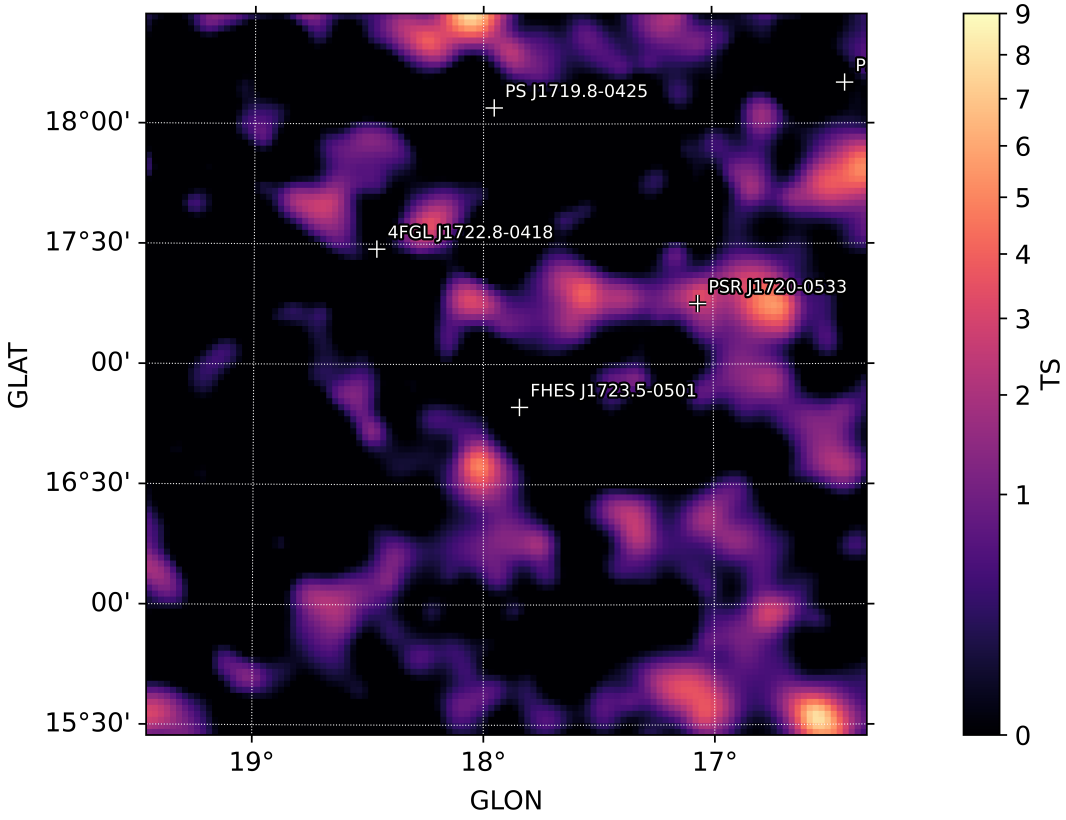

Figure 4.1: TS-map of the region around PSR J1720-0533 using a test source with a typical spectral shape of a pulsar. When producing the map, PSR J1720-0533 is excluded from the model to show any potential emission around its position. The white crosses on the map indicate the positions of the model sources. No significant source is detected at the radio position of the pulsar or in the surrounding displayed $3° \times 3°$ area.

linearly proportional to V [33]. We see from Figure 4.2 that PSR J1720-0533 has an efficiency in converting $\dot{E}$ into L_γ well below 1%, which is unprecedented in the MSP population. In Figure 4.3 we present the same plot, now with only the spider population and including uncertainties in the γ-ray luminosity. In these uncertainties, we have not taken the uncertainty in the distance estimates into consideration, only the uncertainties in the γ-ray fluxes from 4FGL-DR3 [40].

From Figure 3 in Wang et al. 2021 [32], we estimate a 1.4 GHz energy flux density before eclipse of $S_{1400} = 0.7\,\mathrm{mJy}$. This is used in Figure 4.4, where we present a scatter plot of 2PC pulsars' radio flux density in the 1.4 GHz band (S_{1400}), versus the γ-ray energy flux (G_γ) in the $0.1 - 100\,\mathrm{GeV}$ energy band. Because it includes measurements of fluxes and flux densities, this plot is not affected by uncertainties in the distance estimates. For PSR J1720-0533, we plot the 95% upper limit energy flux calculated in this work versus the estimated S_{1400} radio flux density. We find that PSR J1720-0533 has the lowest G_γ value of all the included pulsars, only contested by the uncertainty of PSR J1531-5610, which has the lowest G_γ value in 2PC. We also note that there is nothing peculiar about the radio flux density value for PSR J1720-0533 compared to the other pulsars.

In Table 4.1, we present a catalog of 56 known spider binaries, with their 4FGL γ-ray counterparts (if detected). The set of spiders and their distances is based on Table 1 from Linares and Kachelreiß 2021 [14], with recent updates. For details, we refer to their table and references therein. The γ-ray properties are obtained from the 4FGL counterparts, with some exceptions listed in Table 4.1. For the sources without any γ-ray counterpart, we refer to the referenced literature, and for PSR J1720-0533 we refer to this work.

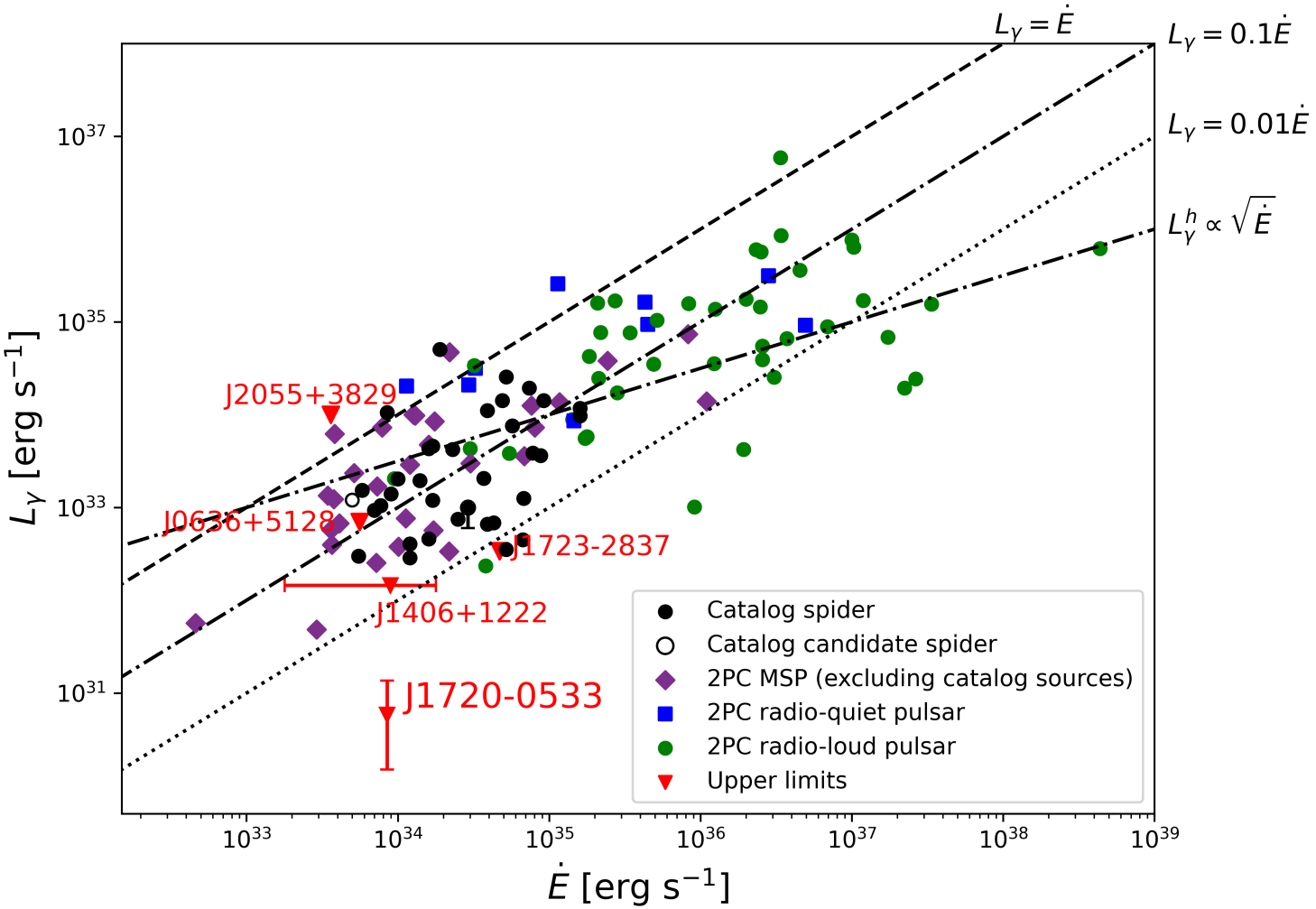

Figure 4.2: The γ-ray luminosities, L_γ, plotted against the spin-down powers, $\dot{E}$, of spider binaries in the catalog in Table 4.1, and the remaining pulsars of the 2PC catalog. The dotted lines indicate constant efficiencies of the γ-ray emission. The heuristic luminosity, $L_\gamma = \sqrt{10^{33}\dot{E}}$ is also shown.

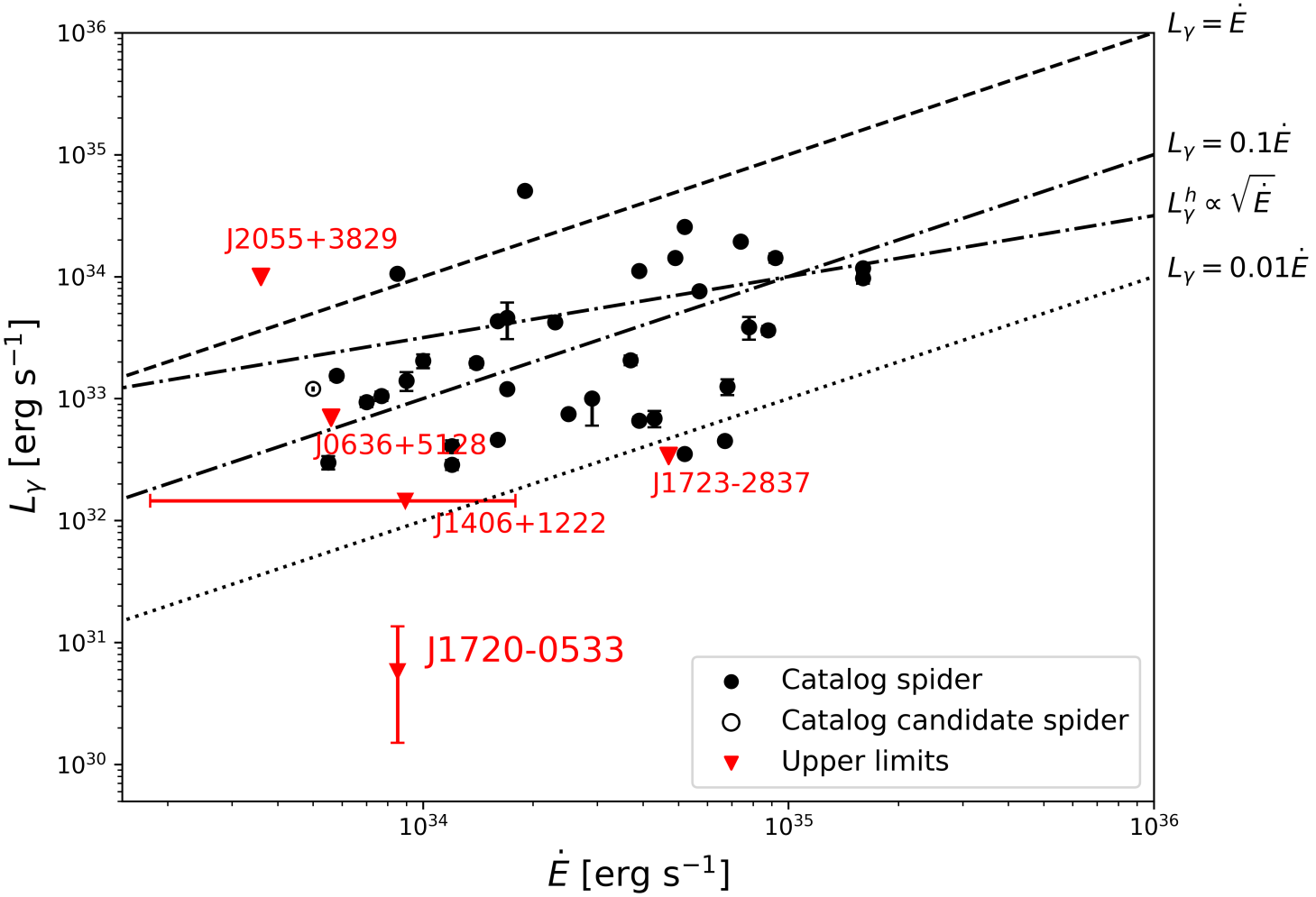

Figure 4.3: Same plot as Figure 4.2, but for the catalog spiders only. Here we include uncertainties in the γ-ray luminosity, extrapolated from the uncertainty in G_γ and ignoring uncertainties in the distance estimates.

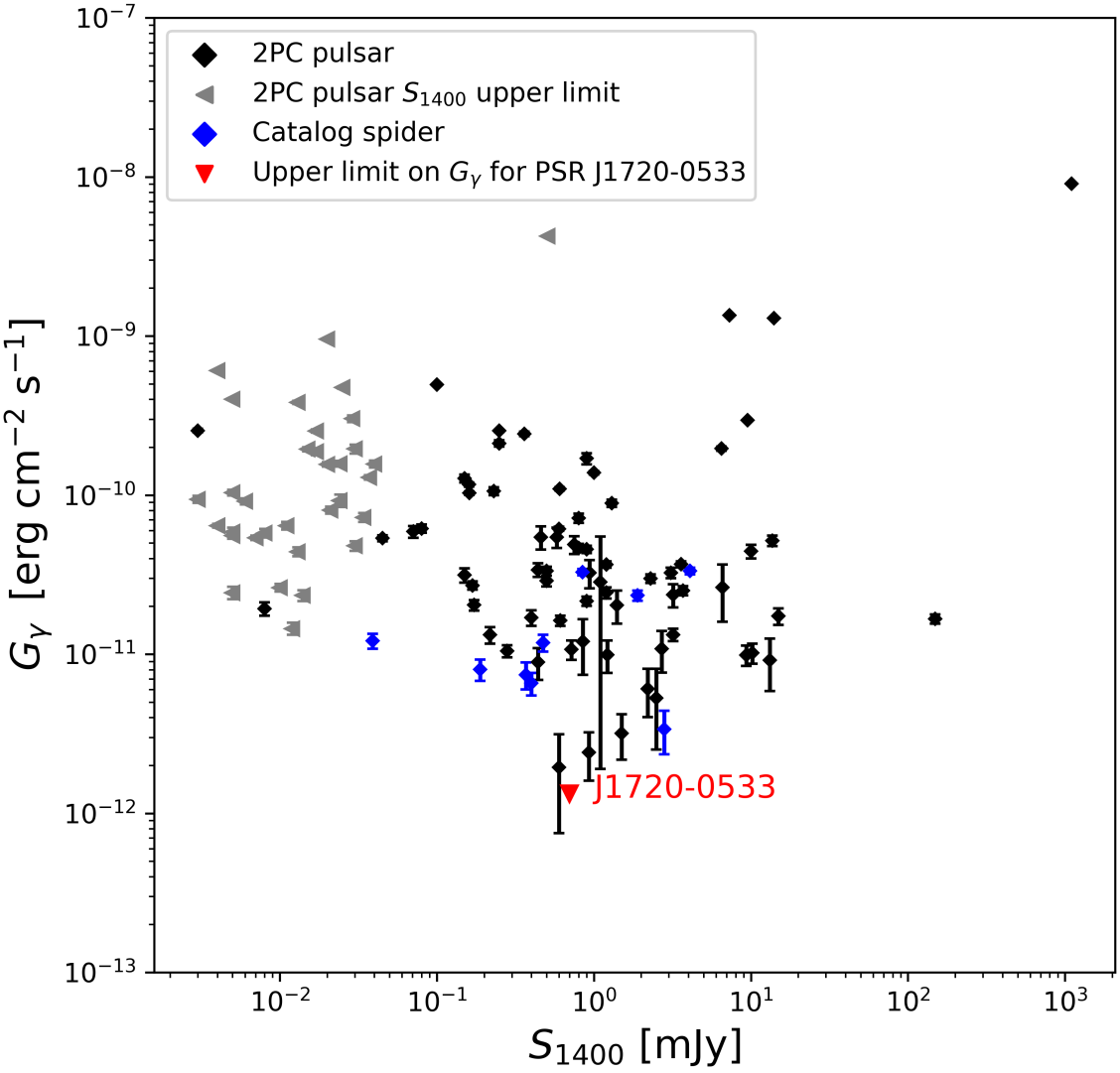

Figure 4.4: Radio flux density in mJy of PSR J1720-0533, catalog spiders, and 2PC pulsars plotted against their γ-ray energy flux, G_γ. The gray triangles indicate upper limits on the 1.4 GHz radio flux density. PSR J1720-0533 has the lowest γ-ray energy flux compared to the pulsars in 2PC, but a common value for the radio flux density.

Table 4.1: Catalog of the γ-ray properties and $\dot{E}$ values of the known spider population, together with their 4FGL counterparts and spectral shapes. In the table, the distances are in units of kpc, G_γ is in units of 10^{-12} erg cm^{-2} s^{-1}, L_γ in units of 10^{33} erg s^{-1}, and $\dot{E}$ in units of 10^{34} erg s^{-1}. The uncertainty in luminosity is calculated considering no uncertainty in the distance estimate. For the spider types, 'RB' and 'BW' indicates redbacks and black widows respectively, and the 'c' represents candidate sources. The sources without a 4FGL counterpart are highlighted by a bold ID, and they are further discussed in Section 4.2.4. References: [14] Linares and Kachelreiß 2021; [55] Crawford et al. 2013; [56] Draghis and Romani 2018; [57] Swiggum et al. 2023; [12] Burdge et al. 2022.

ID	Pulsar name	4FGL counterpart	Spider type	Distance	Spectrum type	G_γ	L_γ	$\dot{E}$	References
1	PSR J1023+0038	4FGL J1023.7+0038	RB	1.4	LP	32.4 ± 0.8	7.6 ± 0.2	5.7	[14, 40]
2	PSR J1048+2339	4FGL J1048.6+2340	RB	0.7	PLSEC	4.9 ± 0.5	0.29 ± 0.03	1.2	[14, 40]
3	PSR J1227-4853	4FGL J1228.0-4853	RB	2.5	PLSEC	19 ± 2	14 ± 1	9.2	[14, 40]
4	PSR J1306-4035	4FGL J1306.8-4035	RB	1.2	LP	9.0 ± 0.7	1.5 ± 0.1	-	[14, 40]
5	PSR J1431-4715	4FGL J1431.4-4711	RB	1.5	PLSEC	4.7 ± 0.7	1.3 ± 0.2	6.8	[14, 40]
6	PSR J1622-0315	4FGL J1623.0-0315	RB	1.1	PLSEC	7.2 ± 0.7	1.01 ± 0.01	0.77	[14, 40]
7	PSR J1628-3205	4FGL J1628.1-3204	RB	1.2	PLSEC	11.3 ± 0.9	1.96 ± 0.2	1.4	[14, 40]
8	PSR J1723-2837	-	RB	0.75	-	< 5	< 0.34	4.7	[55]
9	PSR J1816+4510	4FGL J1816.5+4510	RB	4.5	PLSEC	10.6 ± 0.5	25.6 ± 1.2	5.2	[14, 40]
10	PSR J1908+2105	4FGL J1908.9+2103	RB	2.6	PLSEC	4.9 ± 0.8	3.9 ± 0.6	-	[14, 40]
11	PSR J1957+2516	4FGL J1957.3+2517	RB	3.1	LP	4.0 ± 1.3	4.6 ± 1.5	1.7	[14, 40]
12	PSR J2129-0429	4FGL J2129.8-0428	RB	0.9	PLSEC	6.8 ± 0.4	0.66 ± 0.05	3.9	[14, 40]
13	PSR J2215+5135	4FGL J2215.6+5135	RB	3	PLSEC	18.0 ± 0.8	19.4 ± 0.9	7.4	[14, 40]
14	PSR J2339-0533	4FGL J2339.6-0533	RB	1.1	PLSEC	29.2 ± 0.8	4.2 ± 0.1	2.3	[14, 40]
15	PSR J0212+5320	4FGL J0212.1+5321	RBc	1.1	LP	15.6 ± 0.6	2.26 ± 0.09	-	[14, 40]
16	PSR J0523-2529	4FGL J0523.3-2527	RBc	1.1	LP	12.0 ± 0.5	1.73 ± 0.08	-	[14, 40]
17	PSR J0744-2523	4FGL J0744.0-2525	RBc	1.5	PLSEC	17 ± 1	4.7 ± 0.3	-	[14, 40]
18	PSR J0838.8-2829	4FGL J0838.7-2827	RBc	1	LP	7.3 ± 0.5	0.87 ± 0.06	-	[14, 40]
19	PSR J0954.8-3948	4FGL J0955.3-3949	RBc	1.7	LP	11.6 ± 0.9	4.0 ± 0.3	-	[14, 40]
20	PSR J1302-3258	4FGL J1302.4-3258	RBc	0.96	PLSEC	10.9 ± 0.5	1.20 ± 0.06	0.5	[14, 40]
21	PSR J2039-5618	4FGL J2039.5-5617	RB	0.9	PLSEC	15.4 ± 0.6	1.50 ± 0.06	-	[14, 40]
22	PSR J2333-5526	4FGL J2333.1-5527	RBc	3.1	LP	4.3 ± 0.4	5.0 ± 0.5	-	[14, 40]
23	PSR B1959+20	4FGL J1959.5+2048	BW	2.5	PLSEC	15.7 ± 0.9	11.7 ± 0.6	16	[14, 40]
24	PSR J0610-2100	4FGL J0610.2-2100	BW	3.5	PLSEC	7.2 ± 0.5	10.6 ± 0.7	0.85	[14, 40]
25	PSR J2051-0827	4FGL J2051.0-0826	BW	1	PLSEC	2.5 ± 0.3	0.30 ± 0.04	0.55	[14, 40]
26	PSR J0023+0923	4FGL J0023.4+0920	BW	0.7	PLSEC	7.8 ± 0.6	0.46 ± 0.03	1.6	[14, 40]
27	PSR J0251+2606	4FGL J0251.0+2605	BW	1.2	PLSEC	4.9 ± 0.4	0.84 ± 0.07	-	[14, 40]

Table 4.1 Continued:

ID	Pulsar name	4FGL counterpart	Spider type	Distance	Spectrum type	G_γ	L_γ	$\dot{E}$	References
28	PSR J0636+5128	-	BW	0.5	-	< 5	< 0.7	0.56	[56]
29	PSR J0952-0607	4FGL J0952.1-0607	BW	0.97	PLSEC	2.4 ± 0.03	0.27 ± 0.04	-	[14, 40]
30	PSR J1124-3653	4FGL J1124.0-3653	BW	1.7	PLSEC	12.5 ± 0.06	4.3 ± 0.2	1.6	[14, 40]
31	PSR J1301+0833	4FGL J1301.6+0834	BW	0.7	PLSEC	7.7 ± 0.5	0.45 ± 0.03	6.7	[14, 40]
32	PSR J1311-3430	4FGL J1311.7-3430	BW	1.4	PLSEC	61 ± 1	14.2 ± 0.3	4.9	[14, 40]
33	PSR J1446-4701	4FGL J1446.6-4701	BW	1.5	PLSEC	7.7 ± 0.7	2.1 ± 0.2	3.7	[14, 40]
34	PSR J1513-2550	4FGL J1513.4-2549	BW	2	PLSEC	7.6 ± 0.6	3.6 ± 0.3	8.8	[14, 40]
35	PSR J1544+4937	4FGL J1544.0+4939	BW	1.2	PLSEC	2.4 ± 0.3	0.41 ± 0.05	1.2	[14, 40]
36	PSR J1641+8049	4FGL J1641.2+8049	BW	1.7	PLSEC	2.0 ± 0.3	0.7 ± 0.1	4.3	[14, 40]
37	PSR J1731-1847	4FGL J1731.7-1850	BW	2.5	LP	5 ± 1	3.8 ± 0.8	7.8	[14, 40]
38	PSR J1745+1017	4FGL J1745.5+1017	BW	1.3	PLSEC	7.6 ± 0.6	1.5 ± 0.1	0.58	[14, 40]
39	PSR J1805+06	4FGL J1805.6+0615	BW	2.5	PLSEC	5.3 ± 0.5	3.9 ± 0.4	-	[14, 40]
40	PSR J1810+1744	4FGL J1810.5+1744	BW	2	PLSEC	23.2 ± 0.9	11.1 ± 0.4	3.9	[14, 40]
41	PSR J1928+1245	-	BW	6.1	-	-	-	0.24	[58]
42	PSR J1946-5403	4FGL J1946.5-5402	BW	0.9	PLSEC	9.8 ± 0.5	0.95 ± 0.05	-	[14, 40]
43	PSR J2017-1614	4FGL J2017.7-1612	BW	1.1	PLSEC	6.5 ± 0.6	0.94 ± 0.09	0.7	[14, 40]
44	PSR J2047+1053	4FGL J2047.3+1051	BW	2	PLSEC	4.3 ± 0.6	2.0 ± 0.3	1	[14, 40]
45	PSR J2052+1218	4FGL J2052.7+1218	BW	3.9	PLSEC	4.6 ± 0.6	8 ± 1	-	[14, 40]
46	PSR J2055+3829	-	BW	4.6	-	< 4	< 10	0.36	[59]
47	PSR J2115+5448	4FGL J2115.1+5449	BW	3.4	PLSEC	7.0 ± 0.7	10 ± 1	16	[14, 40]
48	PSR J2214+3000	4FGL J2214.6+3000	BW	3.6	PLSEC	32.6 ± 0.7	50 ± 1	1.9	[14, 40]
49	PSR J2234+0944	4FGL J2234.7+0943	BW	1	PLSEC	10.0 ± 0.6	1.20 ± 0.07	1.7	[14, 40]
50	PSR J2241-5236	4FGL J2241.7-5236	BW	0.5	PLSEC	25 ± 1	0.75 ± 0.03	2.5	[14, 40]
51	PSR J2256-1024	4FGL J2256.8-1024	BW	0.6	PLSEC	8.2 ± 0.5	0.35 ± 0.02	5.2	[14, 40]
52	PSR J1653-0159	4FGL J1653.6-0158	BWc	1	PLSEC	34 ± 1	4.1 ± 0.1	-	[14, 40]
53	PSR J1221-0633	4FGL J1221.4-0634	BW	1	PLSEC	5.8	$0.4 - 1$	2.9	[57]
54	PSR J1317-0157	4FGL J1317.5-0153	BW	2.8	LP	1.49	1.4	0.9	[57]
55	ZTF J1406+1222	-	BWc	1.14	PL	< 0.93	< 0.145	$0.113 - 1.79$	[60]
56	PSR J1720-0533	-	BW	0.191	PLSEC	< 1.33	< 0.00582	0.84	This work

4.2 Discussion on the non-detection of γ-ray emission from PSR J1720-0533

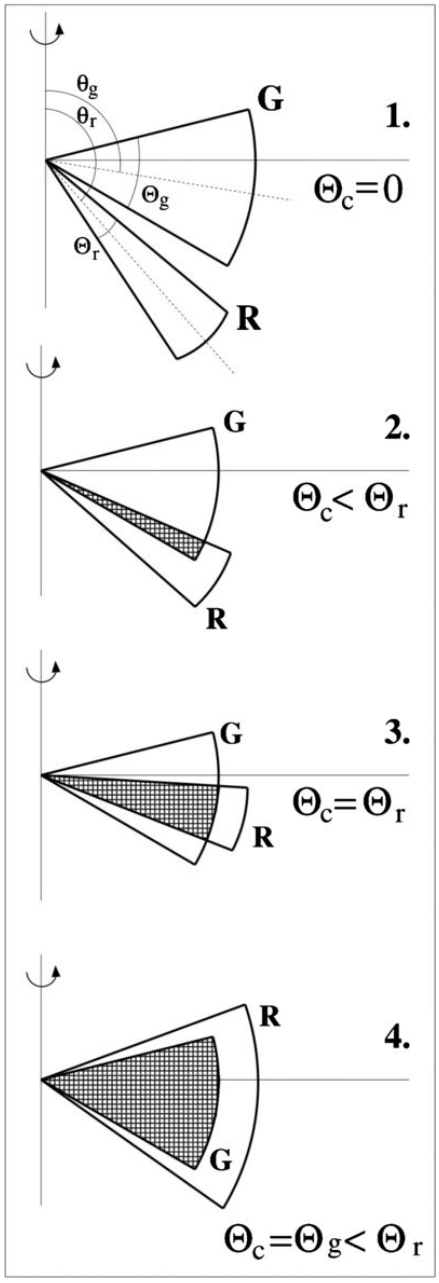

Figure 4.5: Figure 1 from Ravi, Manchester and Hobbs 2010 [61] showing four possible configurations of radio (R) and γ-ray (G) beams from a pulsar emitting in both bands. The centered co-latitudes are indicated by θ_g and θ_r, and the beam widths are indicated by Θ_g and Θ_r. Θ_c denotes the common angular zone for the two beams and is indicated with the hatched area.

One-third of all known MSPs in the Galactic disk show γ-ray emission [62]. Compared to the 56 spiders considered in this study, we find that 50 of them (90%) have a 4FGL counterpart. However, this sample of spiders is biased towards sources with detectable γ-ray emission as many of them have been identified through targeted searches at the positions of unassociated Fermi-LAT sources. As a result, the percentage of γ-ray loud spiders in our sample may not be representative of the population as a whole.

The limit where MSPs are unable to accelerate particles to γ-ray energies in their magnetospheres defines the γ-ray death line for MSPs. This limit is constrained by the lowest spin-down power of the known γ-ray emitting MSP population. In 2PC, this limit was found to be $\dot{E}_{\rm death} \sim 3 \times 10^{33}\,{\rm erg\ s^{-1}}$. However, after discovering γ-ray pulsations in the low-$\dot{E}$ millisecond pulsar PSR J1730-2304, Guillemot et al. 2016 [62] lowered this γ-ray MSP death line to $\dot{E}_{\rm death} \sim 8 \times 10^{32}\,{\rm erg\ s^{-1}}$. In the same paper, the authors suggest that out of all MSPs in the Galactic disk with known spin-down rates and $\dot{E}/d^2 > 5 \times 10^{33}\,{\rm erg\ s^{-1}\ kpc^{-2}}$, 75% are detected by Fermi-LAT. With this in mind, PSR J1720-0533, with $\dot{E} = 0.85 \times 10^{34}\,{\rm erg\ s^{-1}} > \dot{E}_{\rm death}$ and $\dot{E}/d^2 = 2.3 \times 10^{35}\,{\rm erg\ s^{-1}\ kpc^{-2}}$, is a promising candidate to produce γ-ray emission detectable by the Fermi-LAT. However, we have reported a non-detection of γ-ray emission from the pulsar and placed an upper limit on its γ-ray luminosity of $L_\gamma < 5.8 \times 10^{30}\,{\rm erg\ s^{-1}}$. We discuss in this section the possible physical explanations for this extremely low value of L_γ.

4.2.1 Equatorial γ-ray beaming

The non-detection of γ-ray emission from radio pulsars can be attributed to geometrical effects, such as unfavorable viewing angles ξ, which is defined as the angle between the line of sight and the angular momentum vector of the pulsar. In their 2014 paper, Guillemot and Tauris [63] report evidence that MSPs with $\dot{E} > \dot{E}_{\rm death}$ which are not detected in γ-rays, generally have low ξ-values and that these small values are at least partly responsible for the non-detection of γ-ray pulsations. This finding suggests that the γ-ray emission from MSPs is constrained towards its rotational equator so that γ-ray pulsations are preferably seen when ξ is large. As discussed in Section 1.5, recent emission models place the γ-ray production in the current sheet, which is equatorially beamed by nature. Kalapotharakos et al. 2014 [64] report that models with high conductivity in the pulsar magnetosphere, which place the emission close to the equatorial current sheets, are statistically favorable. This provides a physical explanation for the statistical evidence of equatorial γ-ray beaming suggested in Guillemot and Tauris 2014 [63].

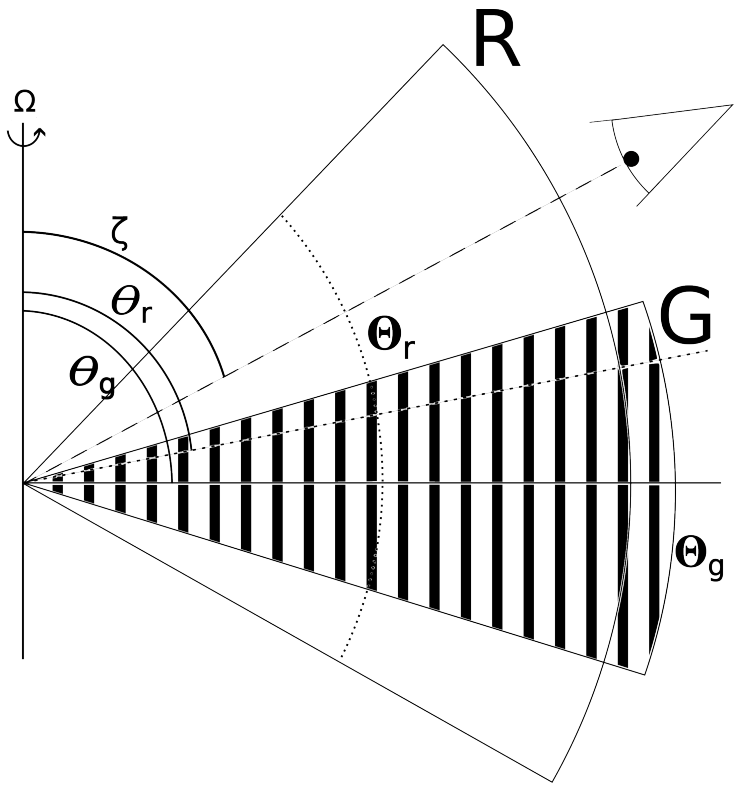

Figure 4.6: A possible configuration of the radio beam, R (empty cone), and the γ-ray beam, G (striped cone), of MSPs. This configuration shows how an unfortunate viewing angle can result in observed radio pulsations but no γ-ray detection, as in PSR J1720-0533. The angles are defined as in Figure 4.5, with the viewing angle ξ also shown.

Considering the absence of γ-ray emission, despite significant radio pulsations observed from PSR J1720-0533, provides insight into the emission-beaming properties of this black widow pulsar. MSPs are known to have wide radio beams as a result of lower surface magnetic fields which places the last open field line further away from the magnetic poles [17]. The lack of significant γ-ray emission excludes the possibility of the radio beam being engulfed by the γ-ray beam, which corresponds to configuration 3 in Figure 4.5. This figure displays Figure 1 from Ravi, Manchester, and Hobbs 2010 [61], where the authors present four possible configurations of radio and γ-ray beams from pulsars. The hatched area shows the range of viewing angles needed to observe both radio and γ-ray emission. We observe that configurations 1, 2, and 4 are possible configurations for PSR J1720-0533 as they maintain the possibility that our line of sight intersects the radio beam, but not the γ-ray beam. We note that the beams in configuration $1-3$ within Figure 4.5 do not represent the wide radio beams for MSPs, nor the possibilities of a narrower γ-ray beam. However, Figure 4.5 provides a good illustration of different beaming configurations, and it shows how equatorially beamed γ-rays can result in a non-detection of γ-ray emission if the viewing angle of the pulsar is too small.

Since i) most known spiders show radio and γ-ray emission, ii) the radio beams of MSPs are believed to be large, and iii) their γ-ray beam is thought to be pointed towards the rotational equatorial plane, we suggest that a version of configuration 4 in Figure 4.5 is the most likely configuration for MSPs. Approximating the beams as two cones of emission and using the solid angle of the two beams given by

$$\Omega_{\text{beam}} = \int_{\text{beam}} \mathrm{d}\Omega = \int_0^{\Theta_i/2} \sin\theta \mathrm{d}\theta \int_0^{2\pi} \mathrm{d}\phi = 2\pi \left(1 - \cos\left(\frac{\Theta_i}{2}\right)\right) \tag{4.2}$$

we find the solid angle ratio between the γ-ray beam and the radio beam:

$$\frac{\Omega_g}{\Omega_r} = \frac{1 - \cos(\Theta_g/2)}{1 - \cos(\Theta_r/2)} = f, \tag{4.3}$$

where f is equal to the fraction of MSPs with detected γ-ray emission. We rearrange and find

$$\Theta_g = 2 \arccos\left(1 - f\left(1 - \cos\frac{\Theta_r}{2}\right)\right). \tag{4.4}$$

For $0 < \Theta_r < 180°$, Equation (4.4) is well approximated by a linear relation. With $f = 0.33$ we get $\Theta_g \simeq 0.53\Theta_r$ in this range. Thus, with the assumptions we have made, we can constrain the width of the γ-ray beam of MSPs to be about half the width of the radio beam on average. We show this suggested configuration for MSPs in Figure 4.6. In the figure, we see how an unfavorable viewing angle can result in the non-detection of γ-rays from PSR J1720-0533, while still detecting radio emission from the wider radio beam. Although the assumption of a cone-like geometry for the γ-ray emission is very simplistic, as we know it has a more complex structure connected to the current sheet, we consider this configuration to be a good approximation to explain the fraction of γ-ray loud MSPs, and the non-detection of γ-ray emission from PSR J1720-0533.

4.2.2 Shklovskii correction

As mentioned in Section 1.6, the observed spin-down rate for PSR J1720-0533 of $\dot{P} = 7.46 \times 10^{-21}$ is not Shklovskii-corrected. Therefore, the intrinsic spin-down power, $\dot{E}_{\rm int} \propto \dot{P}_{\rm int}$, of the pulsar is unknown, where the intrinsic period derivative, $\dot{P}_{\rm int}$, can be expressed as

$$\dot{P}_{\rm int} = \dot{P}_{\rm obs} - \dot{P}_{\rm Gal} - \dot{P}_{\rm Shk}. \tag{4.5}$$

Here, $\dot{P}_{\rm obs}$ is the observed spin-down rate, $\dot{P}_{\rm Gal}$ denotes a correction of Galactic line of sight acceleration, commonly observed for sources in globular clusters [62], and the $\dot{P}_{\rm Shk}$ denotes the Shklovskii correction [65]. $\dot{P}_{\rm Shk}$ is given by

$$\dot{P}_{\rm Shk} \simeq 2.43 \times 10^{-21} \left(\frac{\mu_\perp}{\rm mas\ yr^{-1}}\right)^2 \left(\frac{d}{1\,\rm kpc}\right) \left(\frac{P}{\rm s}\right), \tag{4.6}$$

where $\mu_\perp$ is the transverse proper motion of the system [33]. $\dot{P}_{\rm Shk}$ represents an important correction for MSPs with low $\dot{P}_{\rm int}$-values [33] and is expected to be the primary correction for nearby Galactic sources. Thus, from Equations (4.5) and (1.3), the previously reported spin-down power, $\dot{E}$, of J1720-0533 is expected to be lower than that implied by $\dot{P}_{\rm obs}$ and therefore closer to the γ-ray death line $\dot{E}_{\rm death} \sim 8 \times 10^{32}\,\rm erg\ s^{-1}$ (see Section 4.2). Equation (4.6) shows the significance of precise measurements of $\mu_\perp$ and source distances to obtain accurate results of the intrinsic period derivative of pulsars, especially for the low-$\dot{P}$ (and correspondingly low-$\dot{E}$) sources close to the γ-ray death line. To the best of our knowledge, no $\mu_\perp$ measurement has been reported for PSR J1720-0533 to date.

The small radial distance to PSR J1720-0533 means that the proper transverse motion of the pulsar could be large. Using the largest observed pulsar proper motion of $\mu_\perp = 376\,\rm mas\ yr^{-1}$ from Table 1 in Hobbs et al. 2005 [66] along with the distance, period, and period derivative from Wang et al. 2021 [32] (see Section 1.6) in (4.6), we estimate the Shklovskii correction for PSR J1720-0533, resulting in a value of $\dot{P}_{\rm obs}/\dot{P}_{\rm Shk} \approx 0.03$. Furthermore, we consider the closest known MSP at the time of writing, PSR J0437-4715, with a calculated trigonometric parallax distance of $d = 156.3 \pm 1.3\,\rm pc$ [67]. This MSP is reported to have a proper transverse motion of $\mu_\perp \simeq 141\,\rm mas\ yr^{-1}$ and a spin period of $P \simeq 5.8\,\rm ms$ in Verbiest et al. 2008 [68], resulting in $\dot{P}_{\rm shk} \approx 4.4 \times 10^{-20}$. We see that similar corrections for PSR J1720-0533 would result in a negative $\dot{P}_{\rm int}$ value, which would imply a spin-up scenario. This would be at odds with the detection of radio pulsations and eclipses, which strongly suggest that PSR J1720-0533 is not currently accreting. Although we know there exist transitional MSPs [11], which change states from a rotation-powered MSP to an accretion-powered MSP (e.g. PSR J1023+0038), there is no evidence suggesting that PSR J1720-0533 is a part of this subset of MSPs.

The value of $\dot{P}_{\rm obs}/\dot{P}_{\rm Shk}$ changes to unity for $\mu_\perp \approx 70\,\rm mas\ yr^{-1}$ corresponding to a transverse velocity of $63\,\rm km\ s^{-1}$ for the pulsar at the estimated distance of $d = 0.191\,\rm kpc$. Therefore, using this distance, we predict a maximum transverse proper motion for PSR J1720-0533 of $\mu_\perp < 70\,\rm mas\ yr^{-1}$, to avoid the spin-up scenario.

It is clear from the calculations above that the Shklovskii correction can play a dominant role in determining the intrinsic spin-down rate for PSR J1720-0533. The pulsar's spin-down power

might intrinsically be close to or below the γ-ray death line, which would explain the low γ-ray flux. However, as the pulsar exhibit radio pulsations, we know it is energetic enough to produce radio emission in the region above the magnetic poles. The radio pulsar death line is determined by setting the voltage gap in the polar cap to the limited voltage of the gap, which is given by $\Phi_{\rm max} = BR^3\Omega^2/2c^2$ [69]. The death line is defined by setting $\Phi_{\rm max} = 10^{12}\,{\rm V} \Rightarrow B_{12}/P^2 \simeq 0.2$ [70], where B_{12} is the surface magnetic field strength of the pulsar in units of $10^{12}\,{\rm G}$. Under the assumption of a rotating dipole model, this voltage corresponds to a spin-down power of $\dot{E} \simeq 1.5 \times 10^{30}\,{\rm erg\,s^{-1}}$, which is usually referred to as the radio death line for pulsars. Therefore we know that the $\dot{P}_{\rm Shk}$ term cannot alter the $\dot{P}_{\rm int}$-value of PSR J1720-0533 to the point where the corresponding intrinsic $\dot{E}$-value is below this radio pulsar death line. However, as this would require $\mu_\perp \simeq 70\,{\rm mas\,yr^{-1}}$, this makes no further constraints on the predicted maximum transverse proper motion of PSR J1720-0533.

4.2.3 Distance estimates

In Section 1.6, we discussed that dispersion measure distance estimates are known to be associated with larger uncertainties than other distance estimate techniques. Wang et al. 2021 [32] estimated the distance to PSR J1720-0533 as $d = 191\,{\rm pc}$ using the electron density model YMW16 by Yao et al. 2017 [31]. Even though this model is believed to perform better than its predecessor, NE2001 [71], we use the dispersion measure from Wang et al. 2021 [32] of $36.8\,{\rm cm^{-3}\,pc}$ with the NE2001 electron density model to obtain the distance estimate of $d_{\rm NE2001} = 1.34\,{\rm kpc}$. This distance would result in a 95% upper limit on the γ-ray luminosity of $L_\gamma < 2.9 \times 10^{32}\,{\rm erg\,s^{-1}}$, which is low, but not the lowest value observed for a pulsar. The value of $\dot{E}/d^2_{\rm NE2001} = 4.7 \times 10^{33}\,{\rm erg\,s^{-1}\,kpc^{-2}}$, derived with this distance could explain the non-detection of γ-ray emission due to a large distance to the pulsar as it is below the $\dot{E}/d^2 = 5 \times 10^{33}\,{\rm erg\,s^{-1}\,kpc^{-2}}$ limit, above which Guillemot et al. 2016 [62] reported that 75% of MSPs have detectable γ-ray emission. Independent distance measurements may rule out this scenario, which for now we consider unlikely.

4.2.4 The spiders without a 4FGL γ-ray counterpart

As discussed at the start of Section 4.2, 90% of all known spiders exhibit detectable γ-ray emission, suggesting that the absence of γ-ray emission from spiders is unexpected. However, considering the identification bias towards γ-ray loud spiders, we suggest that spider identifications in other frequency bands should yield a 33% rate of γ-ray loud spiders, consistent with the whole MSP population [62]. This is suggested on the basis that the emission physics of MSPs in spider binaries should not differ from the emission physics of the remaining MSP population. Below we investigate possible reasons for the non-detection of γ-ray emission from the five remaining spiders without a 4FGL γ-ray counterpart: PSR J1723-2837, PSR J0636+5128, PSR J1928+1245 and PSR J2055+3829, which were identified through radio surveys, and ZTF J1406+1222 which was identified through an optical survey with the Zwicky Transient Facility (ZTF).

PSR J1723-2837

PSR J1723-2837 is a 1.84 ms eclipsing redback pulsar in a 15-hour circular orbit [55] with an estimated dispersion measure distance of $d \sim 0.75\,{\rm kpc}$. It was discovered by radio searches performed by Faulkner et al. 2004 [72] in the Parkes multibeam pulsar survey, and is the only redback without any γ-ray association in the Fermi-catalog to date. There is a 4FGL-DR3 source located 0.37° away from the pulsar (4FGL J1723.1-2859) with a 95% semi-major axis of $R_{95} = 0.14°$ [40], but no association is confirmed yet.

Crawford et al. 2013 [55] looked for γ-ray pulsations from PSR J1723-2837 by phase folding the Fermi-LAT photons in the vicinity of the pulsar's position, but find no indication of pulsed emission. They further discuss possible physical reasons behind the non-detection of γ-ray emission, including the pulsar's location at a low galactic latitude, which may place it in a region where the γ-ray flux does not exceed the background emission contamination. They also report an observed spin-down power of $\dot{E} = 4.6 \times 10^{34}\,{\rm erg\,s^{-1}}$ without Shklovskii correction, and place an upper limit on the transverse proper motion of $\mu_\perp < 170\,{\rm mas\,yr^{-1}}$. A $\mu_\perp$-value close to this limit may place the intrinsic spin-down power below the γ-ray death line. Furthermore, the authors report an orbital inclination of 30° to 41°, based on Doppler shifts from optical spectroscopy. This range

of inclination angles suggests a small viewing angle for this system, which could explain the non-detection of γ-rays. Similar to PSR J1720-0533, a measurement of the transverse velocity of this pulsar is needed to confirm whether or not the intrinsic spin-down power is above the γ-ray death line. If it is, then the most probable explanation for the non-detection of γ-ray pulsations is an unfavorable viewing angle.

PSR J0636+5128

PSR J0636+5128 is a black widow pulsar discovered through its radio pulsations as part of the Green Bank Northern Celestial Cap Pulsar Survey [73]. It is in a tight 1.6-hour orbit with a spin period of $P = 2.87\,\mathrm{ms}$, and it has no 4FGL-DR3 source within a 2.9° radius of its position. The Shklovskii-corrected spin-down power of the pulsar is low, with $\dot{E} = 5.6 \times 10^{33}\,\mathrm{erg\,s^{-1}}$, but it is above the γ-ray death line. Draghis and Romani 2018 [56] report good lightcurve fits for inclination angles of $i < 40°$ and discuss that the probable reason for non-detection of γ-rays (and X-rays) in this system is due to an unfavorable viewing angle.

PSR J1928+1245

PSR J1928+1245 is a non-eclipsing black widow pulsar in a tight 3.28-hour orbit with a spin period of $P = 3.02\,\mathrm{ms}$ and a low (Shklovskii-corrected) spin-down power of $P = 2.4 \times 10^{33}\,\mathrm{erg\,s^{-1}}$. Its radio pulsations were discovered with the Arecibo L-Band Feed Array (PALFA), and it was first analyzed by Parent et al. 2019 [58]. They report a large dispersion measure distance of 6.1 kpc, which results in the largest distance to any spider listed in the catalog in Table 4.1. Furthermore, they observe no evidence of radio eclipses and thus they suggest that the orbital inclination of the system is small. There is no published Fermi-LAT analysis of the pulsar, and there are only two sources in 4FGL-DR3 (4FGL J1923.2+1408e and 4FGL J1925.7+1227) which are located within 2° of PSR J1928+1245. However, 4FGL J1923.2+1408e is already associated with a SNR, and 4FGL J1925.7+1227 is a blazar candidate. Thus, the non-detection of γ-ray emission is suspected to result from an unfavorable viewing angle.

ZTF J1406+1222

ZTF J1406+1222 was discovered by Burdge et al. 2022 [12] during a wide optical search for short orbital period binary systems. They classify this source as a hierarchical triple, which hosts a black widow candidate with a 62-minute orbital period and a K-type cool subdwarf in a 12000-year orbit around the black widow. The inner black widow system has the shortest orbital period observed for any spider system to date.

In their paper, they report no γ-ray detection using the Fermi-LAT and no radio emission using the 70 m DSS-14 and 34 m DSS-13 antennae at the Goldstone Observatory[1]. This fact combined with the triple system nature of this black widow makes it an interesting object in the spider subset of MSPs. They also report a 95% upper limit on the γ-ray luminosity of $L_\gamma < 1.45 \times 10^{32}\,\mathrm{erg\,s^{-1}}$. The spin-down power is estimated to be in the range of $\dot{E} = 0.1 \times 10^{34} - 1.8 \times 10^{34}\,\mathrm{erg\,s^{-1}}$ based on the relation between $\dot{E}$ and the heating luminosity L_H, given by $\dot{E} = \eta L_H$, where they assume $0.1 < \eta < 1$. This explains the large uncertainty on the spin-down power of ZTF J1406+1222 in Figure 4.2. The authors report of good model fits to their light curve data with inclination angles as low as 35° and they therefore suggest that the low γ-ray flux can be explained by a low orbital inclination.

PSR J2055+3829

PSR J2055+3829 is an eclipsing black widow first discovered through radio observations with the Nançay Radio Telescope as part of the SPAN512 survey [74]. The pulsar has a spin period of $P = 2.09\,\mathrm{ms}$ and a Shklovskii-corrected spin-down power of $\dot{E} = 3.6 \times 10^{33}\,\mathrm{erg\,s^{-1}}$. There are no 4FGL-DR3 sources within 2.9° of PSR J2055+3829, and Guillemot et al. 2019 [59] report no evidence of γ-ray pulsations after phase folding the Fermi-LAT photons around the pulsar's position. While the authors suggest that the non-detection can be due to unfavorable viewing geometries, they claim that it is most likely due to the large distance to this system. They

[1] See https://www.gdscc.nasa.gov/

estimate a dispersion measure distance of $\sim 4.6\,\mathrm{kpc}$ and using a 100% γ-ray efficiency ($L_\gamma = \dot{E}$) they get a theoretical upper limit on the energy flux of $G_\gamma = 1.4 \times 10^{-12}\,\mathrm{erg\,cm^{-2}\,s^{-1}}$. This value is below their calculated Fermi-LAT energy flux sensitivity of $G_\gamma = 4 \times 10^{-12}\,\mathrm{erg\,cm^{-2}\,s^{-1}}$ in that region, where they applied the same method as the three-year sensitivity map in Figure 16 of the 2PC publication paper [33]. Therefore, the authors concluded that the non-detection of γ-ray pulsations is due to the large distance to PSR J2055+3829, as even with a large efficiency and a favorable viewing angle, the energy flux would not exceed the sensitivity of the Fermi-LAT.

4.3 Conclusions

We have used the full 14-year data set of the Fermi-LAT to conduct a high-energy, binned likelihood analysis of the black widow pulsar PSR J1720-0533. In the process, we model the extended γ-ray source FHES J1723.5-0501 using an extended source optimization algorithm based on Ackermann et al. 2018 [42]. The analysis concluded in a non-detection of γ-ray emission from PSR J1720-0533, with a very stringent upper limit on its γ-ray luminosity of $L_\gamma < 5.8 \times 10^{30}\,\mathrm{erg\,s^{-1}}$. This is the deepest upper limit on the γ-ray luminosity for any pulsar to date. The physical reasons behind the non-detection can be attributed to either an intrinsic spin-down power lower than the γ-ray death line, which we favor if the transverse proper motion of the pulsar $v_\perp \simeq 70\,\mathrm{mas\,yr^{-1}}$, or an unfavorable viewing angle which places Earth's line of sight outside the γ-ray beam of the pulsar. Future measurements of the distance, transverse proper motion, and the orbital inclination angle of this interesting and peculiar MSP can help distinguish between our proposed scenarios.

Bibliography

[1] A. Heger et al. 'How Massive Single Stars End Their Life'. In: *The Astrophysical Journal* 591.1 (2003), pp. 288–300. DOI: 10.1086/375341. URL: https://doi.org/10.1086%2F375341.

[2] S. Chandrasekhar. 'The Maximum Mass of Ideal White Dwarfs'. In: *The Astrophysical Journal* 74 (1931), p. 81. DOI: 10.1086/143324.

[3] S. Miyaji et al. 'Supernova triggered by electron captures'. In: *Publications of the Astronomical Society of Japan* 32 (1980), pp. 303–329.

[4] J. M. Lattimer. 'Neutron Stars and the Nuclear Matter Equation of State'. In: *Annual Review of Nuclear and Particle Science* 71 (2021), pp. 433–464. DOI: 10.1146/annurev-nucl-102419-124827.

[5] A. Watts et al. 'Probing the neutron star interior and the Equation of State of cold dense matter with the SKA'. In: *Advancing Astrophysics with the Square Kilometre Array (AASKA14)*. 2015, p. 43. DOI: 10.22323/1.215.004310.48550/arXiv.1501.00042. arXiv: 1501.00042 [astro-ph.SR].

[6] M. E. Caplan, A. S. Schneider and C. J. Horowitz. 'Elasticity of Nuclear Pasta'. In: *Phys. Rev. Lett.* 121 (2018), p. 132701. DOI: 10.1103/PhysRevLett.121.132701. URL: https://link.aps.org/doi/10.1103/PhysRevLett.121.132701.

[7] J. J. Condon and S. M. Ransom. *Essential Radio Astronomy*. Princeton University Press, 2016. URL: https://www.perlego.com/book/739554/essential-radio-astronomy-pdf.

[8] D. R. Lorimer and M. Kramer. *Handbook of Pulsar Astronomy*. Vol. 4. 2004.

[9] C. Thompson and R. C. Duncan. 'The soft gamma repeaters as very strongly magnetized neutron stars - I. Radiative mechanism for outbursts'. In: *Monthly Notices of the Royal Astronomical Society* 275.2 (1995), pp. 255–300. ISSN: 0035-8711. DOI: 10.1093/mnras/275.2.255. eprint: https://academic.oup.com/mnras/article-pdf/275/2/255/18539652/mnras275-0255.pdf. URL: https://doi.org/10.1093/mnras/275.2.255.

[10] J. W. T. Hessels et al. 'A Radio Pulsar Spinning at 716 Hz'. In: *Science* 311.5769 (2006), pp. 1901–1904. DOI: 10.1126/science.1123430. arXiv: astro-ph/0601337 [astro-ph].

[11] A. Papitto and D. de Martino. 'Transitional Millisecond Pulsars'. In: *Astrophysics and Space Science Library*. Springer International Publishing, 2021, pp. 157–200. DOI: 10.1007/978-3-030-85198-9_6. URL: https://doi.org/10.1007%2F978-3-030-85198-9_6.

[12] K. B. Burdge et al. 'A 62-minute orbital period black widow binary in a wide hierarchical triple'. In: *Nature* 605.7908 (2022), pp. 41–45. DOI: 10.1038/s41586-022-04551-1. URL: https://doi.org/10.1038%2Fs41586-022-04551-1.

[13] B. Bhattacharyya and J. Roy. 'Radio Millisecond Pulsars'. In: *Astrophysics and Space Science Library*. Springer International Publishing, 2021, pp. 1–32. DOI: 10.1007/978-3-030-85198-9_1. URL: https://doi.org/10.1007%2F978-3-030-85198-9_1.

[14] M. Linares and M. Kachelrieß. 'Cosmic ray positrons from compact binary millisecond pulsars'. In: *Journal of Cosmology and Astroparticle Physics* 2021.2 (2021), p. 30. DOI: 10.1088/1475-7516/2021/02/030. arXiv: 2010.02844 [astro-ph.HE].

[15] S. R. Kulkarni and J. J. Hester. 'Discovery of a nebula around PSR1957 + 20'. In: *Nature* 335.6193 (1988), pp. 801–803. DOI: 10.1038/335801a0.

[16] B. W. Stappers et al. 'An X-ray nebula associated with the millisecond pulsar B1957+20'. In: *Science* 299 (2003), pp. 1372–1374. DOI: 10.1126/science.1079841. arXiv: astro-ph/0302588 [astro-ph].

[17] A. K. Harding. 'The Emission Physics of Millisecond Pulsars'. In: *Millisecond Pulsars*. Ed. by S. Bhattacharyya, A. Papitto and D. Bhattacharya. Cham: Springer International Publishing, 2022, pp. 57–85. ISBN: 978-3-030-85198-9. DOI: 10.1007/978-3-030-85198-9_3. URL: https://doi.org/10.1007/978-3-030-85198-9_3.

[18] T. Erber. 'High-Energy Electromagnetic Conversion Processes in Intense Magnetic Fields'. In: *Rev. Mod. Phys.* 38 (1966), pp. 626–659. DOI: 10.1103/RevModPhys.38.626. URL: https://link.aps.org/doi/10.1103/RevModPhys.38.626.

[19] J. Arons. 'Pair creation above pulsar polar caps - Steady flow in the surface acceleration zone and polar CAP X-ray emission'. In: *The Astrophysical Journal* 248 (1981), pp. 1099–1116. DOI: 10.1086/159239.

[20] G. Younes et al. 'Pulse Peak Migration during the Outburst Decay of the Magnetar SGR 1830-0645: Crustal Motion and Magnetospheric Untwisting'. In: *The Astrophysical Journal Letters* 924.2 (2022), p. L27. DOI: 10.3847/2041-8213/ac4700. URL: https://doi.org/10.3847%2F2041-8213%2Fac4700.

[21] S. Bogdanov et al. 'Constraining the Neutron Star Mass-Radius Relation and Dense Matter Equation of State with NICER. III. Model Description and Verification of Parameter Estimation Codes'. In: *The Astrophysical Journal Letters* 914.1 (2021), p. L15. DOI: 10.3847/2041-8213/abfb79. arXiv: 2104.06928 [astro-ph.HE].

[22] K. S. Cheng, C. Ho and M. Ruderman. 'Energetic Radiation from Rapidly Spinning Pulsars. I. Outer Magnetosphere Gaps'. In: *The Astrophysical Journal* 300 (1986), p. 500. DOI: 10.1086/163829.

[23] J. Dyks and B. Rudak. 'Two-Pole Caustic Model for High-Energy Light Curves of Pulsars'. In: *The Astrophysical Journal* 598.2 (2003), pp. 1201–1206. DOI: 10.1086/379052. arXiv: astro-ph/0303006 [astro-ph].

[24] G.-J. Qiao et al. 'The Inner Annular Gap for Pulsar Radiation: γ-Ray and Radio Emission'. In: *The Astrophysical Journal* 606.1 (2004), pp. L49–L52. DOI: 10.1086/421048. arXiv: astro-ph/0403398 [astro-ph].

[25] G.-J. Qiao et al. 'An Annular Gap Acceleration Model for γ-ray Emission of Pulsars'. In: *Chinese Journal of Astronomy & Astrophysics* 7 (2007), pp. 496–502. DOI: 10.1088/1009-9271/7/4/04. arXiv: 0704.3801 [astro-ph].

[26] M. C. Miller et al. 'PSR J0030+0451 Mass and Radius from NICER Data and Implications for the Properties of Neutron Star Matter'. In: *The Astrophysical Journal Letters* 887.1 (2019), p. L24. DOI: 10.3847/2041-8213/ab50c5. URL: https://dx.doi.org/10.3847/2041-8213/ab50c5.

[27] T. E. Riley et al. 'A *NICER* View of PSR J0030+0451: Millisecond Pulsar Parameter Estimation'. In: *The Astrophysical Journal* 887.1 (2019), p. L21. DOI: 10.3847/2041-8213/ab481c. URL: https://doi.org/10.3847%5C%2F2041-8213%2Fab481c.

[28] J.-P. Macquart et al. 'The Commensal Real-Time ASKAP Fast-Transients (CRAFT) Survey'. In: *Publications of the Astronomical Society of Australia* 27.3 (2010), pp. 272–282. DOI: 10.1071/as09082. URL: https://doi.org/10.1071%2Fas09082.

[29] The FAST collaboration. *Five-hundred-meter Aperture Spherical radio Telescope*. Accessed: 2023 - 02 - 06. URL: https://fast.bao.ac.cn/.

[30] P. Jiang et al. 'Commissioning progress of the FAST'. In: *Science China Physics, Mechanics, and Astronomy* 62.5 (2019), p. 959502. DOI: 10.1007/s11433-018-9376-1. arXiv: 1903.06324 [astro-ph.IM].

[31] J. M. Yao, R. N. Manchester and N. Wang. 'A New Electron-density Model for Estimation of Pulsar and FRB Distances'. In: *The Astrophysical Journal* 835.1 (2017), p. 29. DOI: 10.3847/1538-4357/835/1/29. arXiv: 1610.09448 [astro-ph.GA].

[32] S. Q. Wang et al. 'Unusual Emission Variations Near the Eclipse of Black Widow Pulsar PSR J1720-0533'. In: *The Astrophysical Journal Letters* 922.1 (2021), p. L13. DOI: 10.3847/2041-8213/ac365c10.48550/arXiv.2111.02690. arXiv: 2111.02690 [astro-ph.HE].

[33] A. A. Abdo et al. 'The Second Fermi Large Area Telescope Catalog of Gamma-Ray Pulsars'. In: *The Astrophysical Journal Supplement* 208.2 (2013), p. 17. DOI: 10.1088/0067-0049/208/2/17. arXiv: 1305.4385 [astro-ph.HE].

[34] C. Y. Hui and K. L. Li. 'High Energy Radiation from Spider Pulsars'. In: *Galaxies* 7.4 (2019), p. 93. DOI: 10.3390/galaxies7040093. arXiv: 1912.06988 [astro-ph.HE].

[35] The Fermi-LAT collaboration. *The Third Fermi-LAT Pulsar Catalog*. Accessed: 2023 - 02 - 06. URL: https://indico.cern.ch/event/1010947/contributions/4278087/attachments/2227472/3773529/20210412_Symposium_3PC.pdf.

[36] W. B. Atwood et al. 'The Large Area Telescope on the Fermi Gamma-Ray Space Telescope Mission'. In: *The Astrophysical Journal* 697.2 (2009), pp. 1071–1102. DOI: 10.1088/0004-637X/697/2/1071. arXiv: 0902.1089 [astro-ph.IM].

[37] The Fermi-LAT collaboration. *Overview of the LAT*. Accessed: 2023 - 02 - 20. URL: https://fermi.gsfc.nasa.gov/ssc/data/analysis/documentation/Cicerone/Cicerone_Introduction/LAT_overview.html.

[38] F. James. *MINUIT Function Minimization and Error Analysis: Reference Manual Version 94.1*. Accessed: January 2023. 1994. URL: https://cds.cern.ch/record/2296388/files/minuit.pdf.

[39] B. Anderson et al. 'Using Likelihood for Combined Data Set Analysis'. In: *arXiv e-prints* (2015), arXiv:1502.03081. DOI: 10.48550/arXiv.1502.03081. arXiv: 1502.03081 [astro-ph.HE].

[40] S. Abdollahi et al. 'Incremental Fermi Large Area Telescope Fourth Source Catalog'. In: *The Astrophysical Journal Supplement Series* 260.2 (2022), p. 53. DOI: 10.3847/1538-4365/ac6751. URL: https://doi.org/10.3847%2F1538-4365%2Fac6751.

[41] S. Abdollahi et al. '*Fermi* Large Area Telescope Fourth Source Catalog'. In: *The Astrophysical Journal Supplement Series* 247.1 (2020), p. 33. DOI: 10.3847/1538-4365/ab6bcb. URL: https://doi.org/10.3847%2F1538-4365%2Fab6bcb.

[42] M. Ackermann et al. 'The Search for Spatial Extension in High-latitude Sources Detected by the Fermi Large Area Telescope'. In: *The Astrophysical Journal Supplement Series* 237.2 (2018), p. 32. DOI: 10.3847/1538-4365/aacdf7. arXiv: 1804.08035 [astro-ph.HE].

[43] M. Araya, N. Hurley-Walker and S. Quiró s-Araya. 'G17.8 16.7: A new supernova remnant'. In: *Monthly Notices of the Royal Astronomical Society* 510.2 (2021), pp. 2920–2927. DOI: 10.1093/mnras/stab3550. URL: https://doi.org/10.1093%2Fmnras%2Fstab3550.

[44] A. M. Hillas. 'The Origin of Ultra-High-Energy Cosmic Rays'. In: *Annual review of astronomy and astrophysics* 22 (1984), pp. 425–444. DOI: 10.1146/annurev.aa.22.090184.002233.

[45] R. H. Leike, M. Glatzle and T. A. Enßlin. 'Resolving nearby dust clouds'. In: *Astronomy Astrophysics* 639 (2020), A138. DOI: 10.1051/0004-6361/202038169. arXiv: 2004.06732 [astro-ph.GA].

[46] F. Acero et al. 'Fermi Large Area Telescope Third Source Catalog'. In: *The Astrophysical Journal Supplement Series* 218.2 (2015), p. 23. DOI: 10.1088/0067-0049/218/2/23. arXiv: 1501.02003 [astro-ph.HE].

[47] M. Ajello et al. '3FHL: The Third Catalog of Hard Fermi-LAT Sources'. In: *The Astrophysical Journal Supplement Series* 232.2 (2017), p. 18. DOI: 10.3847/1538-4365/aa8221. arXiv: 1702.00664 [astro-ph.HE].

[48] H. Akaike. 'A new look at the statistical model identification'. In: *IEEE Transactions on Automatic Control* 19.6 (1974), pp. 716–723. DOI: 10.1109/TAC.1974.1100705.

[49] M. Wood et al. 'Fermipy: An open-source Python package for analysis of Fermi-LAT Data'. In: *35th International Cosmic Ray Conference (ICRC2017)*. Vol. 301. International Cosmic Ray Conference. 2017, p. 824. DOI: 10.22323/1.301.0824. arXiv: 1707.09551 [astro-ph.IM].

[50] The Fermi-LAT collaboration. *Installing the Fermitools*. Accessed: September 2022. URL: https://fermi.gsfc.nasa.gov/ssc/data/analysis/software/.

[51] F. Aharonian et al. 'Energy dependent γ-ray morphology in the pulsar wind nebula HESS J1825-137'. In: *Astronomy and Astrophysics* 460.2 (2006), pp. 365–374. DOI: 10.1051/0004-6361:20065546. arXiv: astro-ph/0607548 [astro-ph].

[52] R. Beck. 'Magnetic Fields in Galaxies'. In: *Large-Scale Magnetic Fields in the Universe*. Ed. by R. Beck et al. Vol. 39. 2013, pp. 215–230. DOI: 10.1007/978-1-4614-5728-2_8.

[53] F. Acero et al. 'The First Fermi LAT Supernova Remnant Catalog'. In: *The Astrophysical Journal Supplement Series* 224.1 (2016), p. 8. DOI: 10.3847/0067-0049/224/1/8. arXiv: 1511.06778 [astro-ph.HE].

[54] Y. Xing and Z. Wang. 'Fermi Study of Gamma-ray Millisecond Pulsars: the Spectral Shape and Pulsed Emission from J0614-3329 up to 60 GeV'. In: *The Astrophysical Journal* 831.2 (2016), p. 143. DOI: 10.3847/0004-637X/831/2/143. arXiv: 1604.08710 [astro-ph.HE].

[55] F. Crawford et al. 'PSR J1723-2837: An Eclipsing Binary Radio Millisecond Pulsar'. In: *The Astrophysical Journal* 776.1 (2013), p. 20. DOI: 10.1088/0004-637X/776/1/20. arXiv: 1308.4956 [astro-ph.SR].

[56] P. Draghis and R. W. Romani. 'PSR J0636+5128: A Heated Companion in a Tight Orbit'. In: *The Astrophysical Journal Letters* 862.1 (2018), p. L6. DOI: 10.3847/2041-8213/aad2db. arXiv: 1807.04249 [astro-ph.HE].

[57] J. K. Swiggum et al. 'The Green Bank North Celestial Cap Survey. VII. 12 New Pulsar Timing Solutions'. In: *The Astrophysical Journal* 944.2 (2023), p. 154. DOI: 10.3847/1538-4357/acb43f. arXiv: 2212.03926 [astro-ph.HE].

[58] E. Parent et al. 'Eight Millisecond Pulsars Discovered in the Arecibo PALFA Survey'. In: *The Astrophysical Journal* 886.2 (2019), p. 148. DOI: 10.3847/1538-4357/ab4f85. arXiv: 1908.09926 [astro-ph.HE].

[59] L. Guillemot et al. 'Timing of PSR J2055+3829, an eclipsing black widow pulsar discovered with the Nançay Radio Telescope'. In: *Astronomy & Astrophysics* 629 (2019), A92. DOI: 10.1051/0004-6361/201936015. arXiv: 1907.09778 [astro-ph.HE].

[60] K. B. Burdge et al. 'A 62-minute orbital period black widow binary in a wide hierarchical triple'. In: *Nature* 605.7908 (2022), pp. 41–45. DOI: 10.1038/s41586-022-04551-1. arXiv: 2205.02278 [astro-ph.HE].

[61] V. Ravi, R. N. Manchester and G. Hobbs. 'Wide Radio Beams from γ-ray Pulsars'. In: *The Astrophysical Journal Letters* 716.1 (2010), pp. L85–L89. DOI: 10.1088/2041-8205/716/1/L85. arXiv: 1005.1966 [astro-ph.HE].

[62] L. Guillemot et al. 'The gamma-ray millisecond pulsar deathline, revisited. New velocity and distance measurements'. In: *Astronomy & Astrophysics* 587 (2016), A109. DOI: 10.1051/0004-6361/201527847. arXiv: 1601.05987 [astro-ph.HE].

[63] L. Guillemot and T. M. Tauris. 'On the non-detection of γ-rays from energetic millisecond pulsars - dependence on viewing geometry'. In: *Monthly Notices of the Royal Astronomical Society* 439.2 (2014), pp. 2033–2042. DOI: 10.1093/mnras/stu082. arXiv: 1401.2773 [astro-ph.HE].

[64] C. Kalapotharakos, A. K. Harding and D. Kazanas. 'Gamma-Ray Emission in Dissipative Pulsar Magnetospheres: From Theory to Fermi Observations'. In: *The Astrophysical Journal* 793.2 (2014), p. 97. DOI: 10.1088/0004-637X/793/2/97. arXiv: 1310.3545 [astro-ph.HE].

[65] I. S. Shklovskii. 'Possible Causes of the Secular Increase in Pulsar Periods'. In: *Soviet Astronomy* 13 (1970), p. 562.

[66] G. Hobbs et al. 'A statistical study of 233 pulsar proper motions'. In: *Monthly Notices of the Royal Astronomical Society* 360.3 (2005), pp. 974–992. DOI: 10.1111/j.1365-2966.2005.09087.x. arXiv: astro-ph/0504584 [astro-ph].

[67] A. T. Deller et al. 'Extremely High Precision VLBI Astrometry of PSR J0437-4715 and Implications for Theories of Gravity'. In: *The Astrophysical Journal Letters* 685.1 (2008), p. L67. DOI: 10.1086/592401. arXiv: 0808.1594 [astro-ph].

[68] J. P. W. Verbiest et al. 'Precision Timing of PSR J0437-4715: An Accurate Pulsar Distance, a High Pulsar Mass, and a Limit on the Variation of Newton's Gravitational Constant'. In: *The Astrophysical Journal* 679.1 (2008), pp. 675–680. DOI: 10.1086/529576. arXiv: 0801.2589 [astro-ph].

[69] Q.-D. Wu et al. 'Luminosity of a radio pulsar and its new emission death line'. In: *Research in Astronomy and Astrophysics* 20.11 (2020), p. 188. DOI: 10.1088/1674-4527/20/11/188. arXiv: 2007.01015 [astro-ph.HE].

[70] D. Bhattacharya and E. P. J. van den Heuvel. 'Formation and evolution of binary and millisecond radio pulsars'. In: *Physics Reports* 203.1-2 (1991), pp. 1–124. DOI: 10.1016/0370-1573(91)90064-S.

[71] J. M. Cordes and T. J. W. Lazio. 'NE2001.I. A New Model for the Galactic Distribution of Free Electrons and its Fluctuations'. In: *arXiv e-prints* (2002), astro–ph/0207156. DOI: 10.48550/arXiv.astro-ph/0207156. arXiv: astro-ph/0207156 [astro-ph].

[72] A. J. Faulkner et al. 'The Parkes Multibeam Pulsar Survey - V. Finding binary and millisecond pulsars'. In: *Monthly Notices of the Royal Astronomical Society* 355.1 (2004), pp. 147–158. DOI: 10.1111/j.1365-2966.2004.08310.x. arXiv: astro-ph/0408228 [astro-ph].

[73] K. Stovall et al. 'The Green Bank Northern Celestial Cap Pulsar Survey. I. Survey Description, Data Analysis, and Initial Results'. In: *The Astrophysical Journal* 791.1 (2014), p. 67. DOI: 10.1088/0004-637X/791/1/67. arXiv: 1406.5214 [astro-ph.HE].

[74] G. Desvignes et al. 'The SPAN512 mid-latitude pulsar survey at the Nançay Radio Telescope'. In: *Astronomy & Astrophysics* 667 (2022), A79. DOI: 10.1051/0004-6361/202244171. arXiv: 2209.01806 [astro-ph.HE].

Appendix A

Details and Parameters of the Fermi-LAT Data Analysis

A.1 Analysis script for the 2008 – 2022 data set

```
import operator
import matplotlib.pyplot as plt
import matplotlib
import numpy as np
from fermipy.gtanalysis import GTAnalysis
from fermipy.plotting import ROIPlotter
import matplotlib.patheffects as PathEffects
from astropy.coordinates import SkyCoord
from fermipy.jobs.target_analysis import *

gta = GTAnalysis('config.yaml',logging={'verbosity': 3})
matplotlib.interactive(True)

#Perform data preparation
gta.setup()

#Delete sources connected to extended emission
gta.delete_source('4FGL_J1723.5-0501e')

#Free all sources
gta.free_sources()
#Fix sources with npred<1
gta.free_sources(minmax_npred=[0,1],free=False)
gta.fit()

#Localize sources in ROI and >0.1 degree from boundary
for s in gta.roi.sources:
     if s.name!='isodiff':
          if s.name!='galdiff':
               if s['offset_roi_edge'] > -0.1: continue
               gta.localize(s.name,fix_shape=True,free_background=False,
               update=True, dtheta_max= 0.1, make_plots = True)

#Fit spectral params of all sources in ROI
gta.free_sources()
for s in gta.roi.sources:
     if s.name!='isodiff':
          if s.name!='galdiff':
```

```
            if s['offset_roi_edge'] < 0: continue
            gta.free_source(s.name, free = False)
gta.fit()

#Defining function to perform optimization of outer ROI
def B():
    model = {'Index' : 2.0, 'SpatialModel' : 'PointSource',
    'SpectralModel': 'Powerlaw'}
    for i in range(4): #Max iterations
        gta.print_roi()
        gta.free_sources(free=False)
        srcs = gta.find_sources(model=model, sqrt_ts_threshold=3.0,
        min_separation=0.5,multithread=True, sources_per_iter=50,
        max_iter=1)
        gta.print_roi()

        #Checking if all added sources are in R_inner
        out = False
        for s in range(len(srcs['sources'])):
            if srcs['sources'][s]['offset']>1:
                out = True

        #Deleting newly added sources in inner ROI
        exc_lst = ['isodiff', 'galdiff']
        for s in gta.roi.sources:
            if '4FGL' in s.name:
                exc_lst.append(s.name)
        gta.delete_sources(distance = 1,  exclude = exc_lst)

        #Sources with TS>100 modeled with LogParabola:
        for s in gta.roi.sources:
            if 'PS' in s.name:
                if s.name!='isodiff':
                    if s.name!='galdiff':
                        if s['ts']>100:
                            gta.set_source_spectrum(s.name,
                            spectrum_type = 'LogParabola')

        if srcs['sources'] == []:
            print('No more sources with TS>9')
            print('No of iterations: ',i+1)
            gta.free_sources()
            for s in gta.roi.sources:
                 if s.name!='isodiff':
                     if s.name!='galdiff':
                         if s['offset_roi_edge'] < 0: continue
                         gta.free_source(s.name, free = False)
            gta.fit()

            #Save
            gta.write_roi('B4')
            break

        if out == False:
            print('All sources outside R_inner added to model')
            print('No of iterations: ',i+1)
            gta.free_sources()
            for s in gta.roi.sources:
```

```
                if s.name!='isodiff':
                    if s.name!='galdiff':
                        if s['offset_roi_edge'] < 0: continue
                        gta.free_source(s.name, free = False)
            gta.fit()

            #Save
            gta.write_roi('B4')
            break

        if i == 5:
            print('Maximum number of iterations reached:',i+1)
            break
    return

#Run optimization of outer ROI
B()

#Defining function to perform optimization of inner ROI and test
#central source for extension
def C():


    #Add source of interest as point source
    gta.add_source('FHES J1723.5-0501',{ 'glon' : 17.9, 'glat' : 16.96,
    'SpectrumType' : 'PowerLaw', 'Index' : 2.0, 'Scale' : 1000,
    'Prefactor' : 1e-11,'SpatialModel' : 'PointSource' })

    C_sources={}
    for i in range(5):
        #Testing for extention hypotisis:
        gta.free_sources(free=False)
        gta.free_sources(distance=1)
        gta.free_sources(distance=1.5,pars='norm')
        gta.free_source('FHES J1723.5-0501')
        gta.free_source('galdiff', free=False)
        gta.free_source('isodiff', free=False)
        ext_1 = gta.extension('FHES J1723.5-0501',fit_position =
        True, free_background = True,spatial_model='RadialGaussian')

        L_n_1 = ext_1['loglike_ptsrc']
        L_n_m = ext_1['loglike_ext']
        delta_mu = 1
        Delta_m = 2*(L_n_1-L_n_m+delta_mu)

        gta.write_roi('C_last')

        #Adding one additional source to the model. Will be in
        #R_inner after executing the B step of the analysis
        model = {'Index' : 2.0, 'SpatialModel' : 'PointSource',
        'SpectralModel': 'Powerlaw'}
        srcs = gta.find_sources(model=model, sqrt_ts_threshold=3.0,
        min_separation=0.5,multithread=True, sources_per_iter=5,
        max_iter=1)

        s_in = []
        for s in srcs['sources']:
            if s['offset'] >1:
```

```
                gta.delete_source(s['name'])
            else:
                s_in.append(s['name'])
        for s in range(len(s_in)):
            if s>0:
                gta.delete_source(s_in[s])
        if s_in==[]:
            print('Found no sources with TS>9 in iteration ',i+1)
            return

        #Fitting all components in ROI
        gta.free_sources()
        for s in gta.roi.sources:
                if s.name!='isodiff':
                    if s.name!='galdiff':
                        if s['offset_roi_edge'] < 0: continue
                        gta.free_source(s.name, free = False)
        gta.fit()

        #Refit locations of central source and new sources in R_inner
        C_sources[srcs['sources'][0]['name']] = srcs['sources']
        [0]['ts']
        C_sorted = sorted(C_sources.items(), key=lambda x: x[1],
        reverse=True)
        gta.localize('FHES J1723.5-0501',fix_shape=True,
        free_background=False, update=True)
        for s in C_sorted:
            gta.localize(s[0],fix_shape=True,free_background=False,
            update=True, dtheta_max = 0.1)

        #Test for extended emission
        gta.free_sources(free=False)
        gta.free_sources(distance=1)
        gta.free_sources(distance=1.5,pars='norm')
        gta.free_source('FHES J1723.5-0501')
        gta.free_source('galdiff', free=False)
        gta.free_source('isodiff', free=False)
        ext_2= gta.extension('FHES J1723.5-0501',free_background =
        True,spatial_model='RadialGaussian')

        L_n_m_1 = ext_2['loglike_ext']
        TS_m_1 = 2*(L_n_m_1-L_n_m)

        if Delta_m<0 and TS_m_1<16:
            print('Delta_m>0 & TSm+1>16')
            print('TS_m =', ext_1['ts_ext'])
            return
    print('Number of maximum iterations reached')
    return

#Run optimization of inner ROI
C()

#Free normalizations and spectral index for sources within 1 degree,
#and normalizations of sources within 1.5 degrees
gta.free_sources(free=False)
gta.free_sources(distance=1)
gta.free_sources(distance=1.5,pars='norm')
```

```
gta.free_source('galdiff', free=False)
gta.free_source('isodiff', free=False)
ext = gta.extension('FHES_J1723.5-0501',fit_position = True,
free_background = True, spatial_model='RadialGaussian',update = True)

#Fit all sources inside 6x6 ROI
gta.free_sources()
for s in gta.roi.sources:
     if s.name!='isodiff':
          if s.name!='galdiff':
               if s['offset_roi_edge'] < 0: continue
               gta.free_source(s.name, free = False)
gta.fit()

#Free normalizations and spectral index for sources within 1 degree,
#and normalizations of sources within 1.5 degree
gta.free_sources(free=False)
gta.free_sources(distance=1)
gta.free_sources(distance=1.5,pars='norm')
gta.free_source('galdiff', free=False)
gta.free_source('isodiff', free=False)
ext = gta.extension('FHES_J1723.5-0501',fit_position = True,
free_background = True, spatial_model='RadialGaussian',update = True)

#Fit all sources inside 6x6 ROI
gta.free_sources()
for s in gta.roi.sources:
     if s.name!='isodiff':
          if s.name!='galdiff':
               if s['offset_roi_edge'] < 0: continue
               gta.free_source(s.name, free = False)
gta.fit()

#Add PSR J1720
gta.add_source('PSR_J1720-0533',{ 'glon' : 17.06662724, 'glat' :
17.25233543, 'SpectrumType' : 'PLSuperExpCutoff', 'Index1' : 1.54,
'Scale' : 1000, 'Prefactor' : 1e-13,'Cutoff': 3700, 'SpatialModel':
'PointSource' })

#Free parameters of sources in ROI
gta.free_sources(free=False)
for s in gta.roi.sources:
     if s.name!='isodiff':
          if s.name!='galdiff':
               if s.name != 'PSR_J1720-0533':
                    if s['offset_roi_edge'] > 0: continue
                    gta.free_source(s.name)
gta.free_source('PSR_J1720-0533', pars = 'norm')

#Perform the last fit to produce the final model including
#PSR J1720-0533
gta.fit()
```

A.2 Configuration file for the 2008 – 2016 data set

```
binning:
  binsperdec: 8
  binsz: 0.025
  coordsys: GAL
  roiwidth: 6
components:
- { selection: {evtype: 32} }
- { selection: {evtype: 28} }
selection:
  emax: 877938
  emin: 1000
  evclass: 128
  filter: DATA_QUAL==1 && LAT_CONFIG==1
  target: 3FGL J1725.0-0513
  tmax: 476239414
  tmin: 239557417
  roicut: 'no'
  zmax: 100
  radius: 8
data:
  evfile: events.lst
  scfile: spacecraft.fits
gtlike:
  edisp: true
  edisp_disable:
  - isodiff
  - galdiff
  irfs: P8R2_SOURCE_V6
model:
  catalogs:
  - 3FGL
  galdiff: gll_iem_v06.fits
  isodiff: iso_P8R2_SOURCE_V6_v06.txt
  src_roiwidth: 10
optimizer:
  min_fit_quality: 3
  optimizer: NEWMINUIT
extension:
  fix_shape: True
  free_background: True
  spatial_model: RadialGaussian
```

A.3 Configuration file for the 2008 – 2022 data set

```
binning:
  binsperdec: 8
  binsz: 0.025
  coordsys: GAL
  roiwidth: 6
components:
- { selection: {evtype: 32} }
- { selection: {evtype: 28} }
selection:
  emax: 1000000
  emin: 1000
  evclass: 128
  filter: DATA_QUAL==1 && LAT_CONFIG==1
  glat: 16.96
  glon: 17.9
  tmax: 685859961
  tmin: 239557417
  roicut: 'no'
  zmax: 100
  radius: 8
data:
  evfile: events.lst
  scfile: spacecraft.fits
gtlike:
  edisp: true
  edisp_disable:
  - isodiff
  - galdiff
  irfs: P8R3_SOURCE_V3
model:
  catalogs:
  - 4FGL
  galdiff: gll_iem_v07.fits
  isodiff: iso_P8R3_SOURCE_V3_v1.txt
  src_roiwidth: 10
optimizer:
  min_fit_quality: 3
  optimizer: NEWMINUIT
extension:
  fix_shape: True
  free_background: True
  spatial_model: RadialGaussian
```

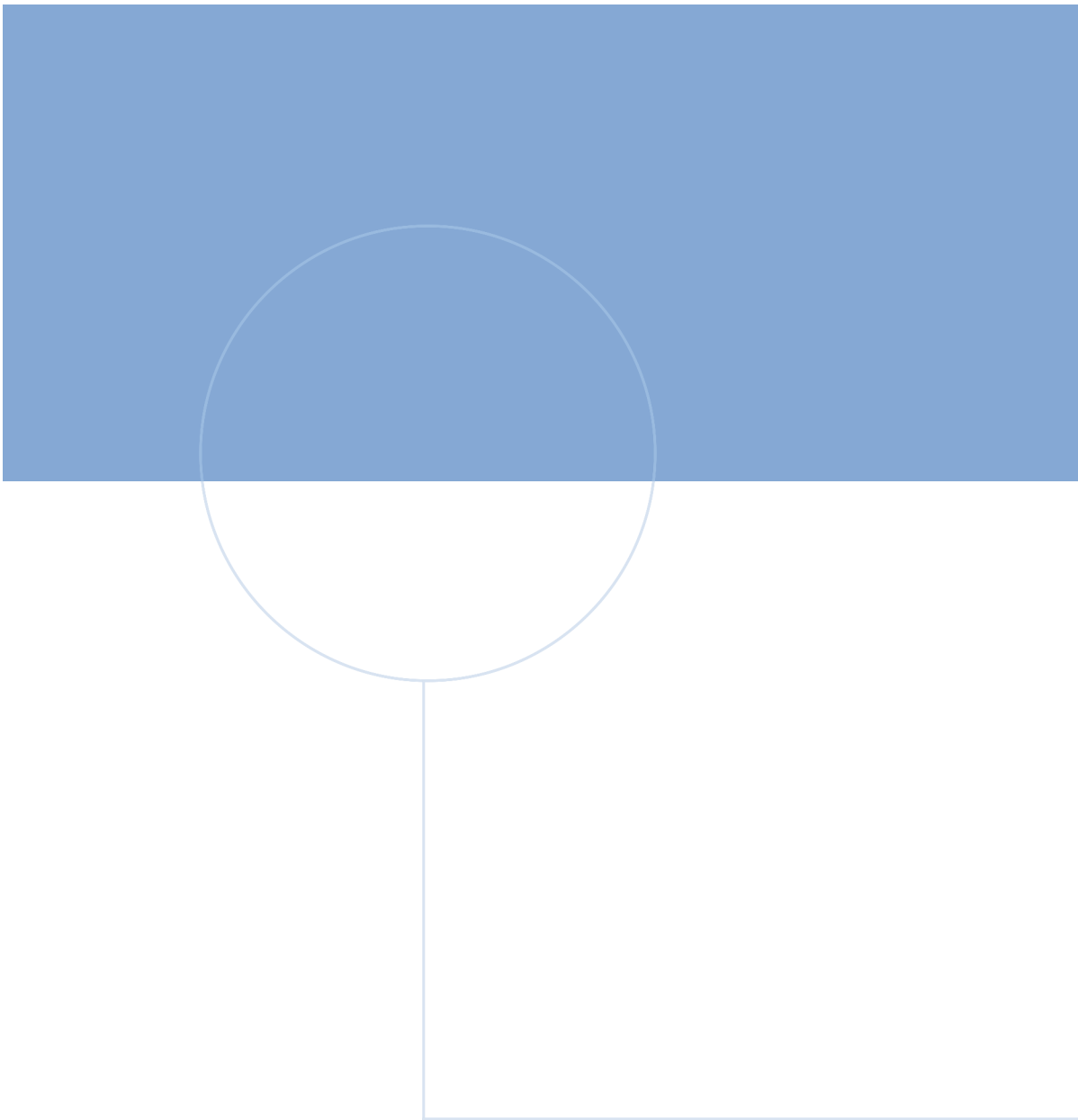

NTNU

Norwegian University of
Science and Technology